Neutrino Oscillation Analysis of Upward Through-going and Stopping Muons in Super-Kamiokande

Kazunori Nitta

February 2003

Doctor Thesis, Osaka University

Abstract

A total of 463 upward stopping muons and 1846 upward through-going muons of minimum energy of 1.6 GeV are observed in 1645 live days of the Super-Kamiokande experiment. The observed upward through-going muon flux and the upward stopping muon flux are 1.71$\pm$ 0.04(stat.)$\pm$ 0.02(syst.)$\times 10^{-13}$ cm^{-2}s^{-1}sr^{-1} and 0.42$\pm$ 0.02(stat.)$\pm$ 0.02(syst.)$\times 10^{-13}$ cm^{-2}s^{-1}sr^{-1} ,respectively. The ratio of upward stopping/through-going muons is 0.245 $\pm$ 0.014(stat.) $\pm$ 0.013(syst.). The double ratio of the observed ratio to the expected ratio is 0.659 and the difference comes to 2.6σ. The ν_μ-ν_τ oscillation hypothesis with the parameters of $\sin^2 2\theta > 0.7$ and $1.3\times 10^{-3} < \Delta m^2 < 4.5\times 10^{-3}$ eV^2 at 90 % confidence level is consistent with the zenith angle distribution for the combination of upward stopping muons and through-going muons. The null oscillation is strongly disfavored.

Acknowledgments

I would like to express my great appreciation to my adviser, Prof. Yoshitaka Kuno. He invited me to his group and gave me a chance to continue my study.

I would like to express my graduate to Prof. Y.Nagashima. He introduced me to the Super-Kamiokande experiment. I am deeply indebted to members of upward-going muon analysis group. Especially I would like to thank Prof. Yoshitaka Ito. This thesis would never be completed without his advice. I would like to thank Dr. A.Okada, Dr. M.Yoshida and Dr. C.Saji, and also wish to thank the members in USA, Prof. R.J.Wilkes, Prof. J.G.Learned, Dr. A.Habig, Dr. S.Matsuno, Dr. A.L.Stachyra and Mr. D.Shantanu.

I am thankful to Mr. S.Yamada, Mr. S.Nakayama, Mr. M.Yamashita and Mr. A.Takeda, for their friendship and encourage in Kamioka. I have learnt so many things from their discussion. My thanks also go to Mr. Y.Gando, Mr. M.Ishitsuka, Mr. C.Mitsuda, Mr. K.Kawasaki, Mr. Y.Ashie, Mr. A.Minamino, Ms. Y.Nakajima and Mr. R.Nanbu. I am happy to enjoy the life in Kamioka with them.

I would like to thank all the Super-Kamiokande and K2K collaborators and the staff in the Kamioka Observatory for their help and kindness. I grate fully acknowledge the cooperation of Kamioka Mining and Smelting Company.

I wish to express my gratitude to Prof. T.Yamanaka, Prof. M.Aoki, Prof. M.Hazumi and Dr. T.Hara for helpful advice.

I express my gratitude to the members at Osaka University for the good companionship and encouragement, Mr. T.Hojo, Mr. K.Kotera, Mr. K.Hara, Mr. H.Miyake, Mr.K.Sakashita, Ms. Y.Ikemoto, Mr. N.Nosaka, Mr. Y.Takubo, Ms. J.Ishii, Mr. F.Maeda, Mr. K.Nakahara, Mr. Y.Arakawa, Mr. Y.kuriyama, Mr. S.Takano, Mr. A.Ishihara, Mr. H.Sakamoto, Mr. K.Terai. I am deeply indebted to Ms. S.Tsuzuki, Ms. N.Sugimoto and Ms. M.Torikoshi for their encouragement and help.

At the last, I would like to thank Prof. Masato Takita. He teached me experimental physics of the atmospheric neutrino and I learned many things under his excellent guidance. I can't thank him enough for his eagerness and useful instruction.

I am very proud of participation in Super-Kamiokande experiment.

Contents

List of Figures

List of Tables

Chapter 1

Introduction

The existence of neutrino was suggested by Pauli[1] in 1930 since the energy and momentum were not conserved in nuclear beta decays. In 1934, Fermi took the neutrino hypothesis and built his theory of beta decay(weak interaction). Bethe and Peierls showed that the cross section between neutrinos and matter should be extremely small: billions of time smaller than the one of an electron. This particle interacts so weakly with matter that it can go through the whole earth without the interaction.

In 1952, Reines and Cowan observed the neutrino[2]. The target was made of about 200 litters of water mixed with cadmium chloride. An anti-neutrino coming from the nuclear reactor interacts with a proton of the target matter and give a positron and a neutron. The positron annihilates with an electron of the surrounding material, and two simultaneous photons are produced. The neutron is captured by a cadmium nucleus. To identify the neutrino interaction, several gamma rays are also detected in the scintillator as a delayed coincidence after the detection of the gamma ray by positron annihilation. The group of Lederman, Schwarz and Steinberger[3] discovered the muon neutrino in 1962 by observing the interaction ν_μ+N$\rightarrow$ μ+N' using a neutrino beam by the decay of pions. Neutrinos produced in association with muons do not behave the same as those produced in association with electrons. In 2000, the DONUT collaboration[4] announced the first direct observation of the tau neutrino by the observation of tau particles produced by tau neutrinos. Now there are known to be three kinds of neutrinos.

In the Standard Model[5, 6, 7] for elementary particles, the neutrino is described as exactly massless. However there is no fundamental reason that the neutrino must be exactly massless. Whether the neutrino has a mass has been a long standing problem. Table 1.1 shows the best upper limits at present on the mass of each neutrino species. The best limit of ν_e mass is obtained to measure the endpoint region of the electron energy spectrum of the tritium beta-decay[8]. The decay results in a 3-helium, electron and an electron anti-neutrino. If the neutrino has non-zero rest mass, the shape of the spectrum differs from the case of the zero rest mass at the high energy part. However the differences are exiguous and the demands on the sensitivity and accuracy of the experiment are

Flavor	Mass Limit	Experiment
ν_e	3 eV	tritium beta decays[8]
ν_e	170 KeV (90%C.L)	PSI[9]
ν_e	18.2 MeV (95%C.L)	ALEPH[10]

Table 1.1: the best upper limits at present

therefore enormous. The ν_μ mass is constrained by measuring the muon momentum in $\pi\rightarrow \mu+\nu_\mu$ decays. The PSI group gives an upper limit on the ν_μ mass of 170 keV[9]. The best limit on the ν_τ mass is obtained from the kinematics of hadronic tau decays. The best result using this method has been obtained by the ALEPH collaboration in the decay channel of Z boson into $\tau\rightarrow 5\pi(\pi^0)\nu_\tau$ and $\tau\rightarrow 3\pi\nu_\tau$ [10]. There is a possibility of an astronomical detection of neutrino mass using neutrinos from a supernova explosion. If neutrinos are massive, heavier mass neutrinos arrive earlier. Thus neutrino detectors would first see higher energy events and then see less energetic events. This effect was not observed from the spread of arrival time of neutrinos in SN1987A, and the mass limit of $\nu_\mathrm{e} < 16$ eV was obtained[11].

Results from these direct neutrino mass measurements are consistent with massless neutrinos but does not dismiss the possibility of mass. For example, the smallness of the neutrino mass is naturally explained by the seesaw mechanism[12, 13]. The Super-Kamiokande experiment which is a 50 kton water Cherenkov detector indicated evidently that at least some flavors of neutrinos are massive by the observation of atmospheric neutrinos[21, 22]. This result shows that the standard model must be extended to accommodate for neutrino masses. This smallness of the neutrino mass quite possibly has a key to open the door of new elementary particle physics.

1.1 Neutrino Oscillation

If the neutrino has a mass, the mass and flavour eigenstates are not necessarily identical. Thus, the flavour eigenstates $|\nu_\alpha\rangle$ (α = e,μ,τ) can be expressed as a superposition of the mass eigenstates, $|\nu_i\rangle$ (i = 1,2,3),

$$|\nu_\alpha\rangle = \sum_i U_{\alpha i}|\nu_i\rangle \tag{1.1}$$

where U is a unitary mixing matrix between the the two eigenstates ($U^\dagger U$=$UU^\dagger$=1 and $\sum_i U_{\alpha i}U^\dagger_{i\beta} = \delta_{\alpha\beta}$). The mixing matrix for three neutrinos, Maki-Nakagawa-Sakata(MNS) matrix[14, 15], is usually expressed as follows,

$$U = \begin{pmatrix} c_{12}c_{13} & s_{12}c_{13} & s_{13}e^{-i\delta} \\ -s_{12}c_{23} - c_{12}s_{23}s_{13}e^{i\delta} & c_{12}c_{23} - s_{12}s_{23}s_{13}e^{i\delta} & s_{23}c_{13} \\ s_{12}s_{23} - c_{12}c_{23}s_{13}e^{i\delta} & -c_{12}s_{23} - s_{12}c_{23}s_{13}e^{i\delta} & c_{23}c_{13} \end{pmatrix}, \tag{1.2}$$

where c_{ij}, s_{ij} and δ correspond to $\cos\theta_{ij}$, $\sin\theta_{ij}$ and CP violation phase respectively (i, j = 1,2,3), $\theta_{i,j}$ is the mixing angle of the mass eigenstates ν_i and ν_j.

The mass eigenstate $|\nu_i\rangle$ with a finite mass m_i, momentum p and energy $E_i = \sqrt{p^2 + m_i^2}$ satisfies the following energy eigenvalue equation:

$$H_0|\nu_i\rangle = E_i|\nu_i\rangle. \tag{1.3}$$

where H_0 is the free neutrino Hamiltonian. The time dependent Schrödinger equation is then expressed as:

$$\begin{aligned} i\frac{d}{dt}|\nu_\beta(t)\rangle &= H_0|\nu_\beta(t)\rangle \\ &= \sum_j U_{\beta j}E_j|\nu_j(t)\rangle \\ &= \sum_{j,\alpha} U_{\beta j}E_j U^\dagger_{\alpha j}|\nu_\alpha(t)\rangle \end{aligned} \tag{1.4}$$

The mass eigenstates evolve with the phase factor $\exp(-iEt)$. Using the relativistic approximation $E_j = \sqrt{p^2 + m_j^2} \approx p + m_j^2/2p$, the $|\nu_\beta(t)\rangle$ can be obtained by solving this equation analytically:

$$\begin{aligned} |\nu_\beta(t)\rangle &= \sum_{j,\alpha} U_{\beta j}\exp(-iE_j t)U^*_{\alpha j}|\nu_\alpha(0)\rangle \\ &= \exp(-ipt)\sum_{j,\alpha} U_{\beta j}\exp\left(-i\frac{m_j^2}{2p}t\right)U^*_{\alpha j}|\nu_\alpha(0)\rangle \\ &\equiv \sum_\alpha A_{\alpha\beta}|\nu_\alpha(0)\rangle \end{aligned} \tag{1.5}$$

$$A^*_{\alpha\beta} = \exp(ipt)\sum_k U^*_{\alpha k}\exp\left(i\frac{m_k}{2p}t\right)U_{\beta k} \tag{1.6}$$

where $A_{\alpha\beta}$ shows the transition amplitude from ν_α to ν_β. Then, the oscillation probability is calculated as:

$$\begin{aligned} P_{\alpha\to\beta} &= |A_{\alpha\beta}|^2 = A_{\alpha\beta}A^*_{\alpha\beta} \\ &= \mathrm{Re}\sum_{j,k} U_{\alpha j}U^*_{\beta j}U^*_{\alpha k}U_{\beta k}\exp\left(-i\frac{m_j^2 - m_k^2}{2p}t\right) \end{aligned} \tag{1.7}$$

Using the unitarity condition $\sum_i U_{\alpha i}U^*_{\beta i} = \delta_{\alpha\beta}$, and employing the neutrino propagation length $t \cong L$ and energy $p \cong E$ in natural unit,

$$P_{\alpha\to\beta} = \delta_{\alpha\beta} - \mathrm{Re}\sum_{j,k} U_{\alpha j}U^*_{\beta j}U^*_{\alpha k}U_{\beta k}\left\{1 - \exp\left(-i\frac{\Delta m^2_{jk}L}{2E}\right)\right\}$$

$$
\begin{aligned}
&= \delta_{\alpha\beta} - 2\sum_{j<k} U_{\alpha j} U^*_{\beta j} U^*_{\alpha k} U_{\beta k} \cos\left(\frac{\Delta m^2_{jk} L}{2E}\right) \\
&= \delta_{\alpha\beta} - 4\sum_{j<k} U_{\alpha j} U^*_{\beta j} U^*_{\alpha k} U_{\beta k} \sin^2\left(\frac{\Delta m^2_{jk} L}{4E}\right),
\end{aligned}
\tag{1.8}
$$

where $\Delta m^2 \equiv m_j^2 - m_k^2$ is the difference of mass squared.

In the case of two flavor oscillation, the unitary matrix is simply given by the following 2 by 2 matrix with one mixing angle, θ,

$$
U = \begin{pmatrix} \cos\theta & \sin\theta \\ -\sin\theta & \cos\theta \end{pmatrix}, \tag{1.9}
$$

Considering the $\nu_\mu \to \nu_\tau$ oscillation, the probability of a neutrino oscillation is given in a much simpler form:

$$
P_{\nu_\mu \to \nu_\tau} = |\langle \nu_\tau(t) | \nu_\mu(0) \rangle|^2 \;=\; \sin^2 2\theta \sin^2\left(\frac{\Delta m^2}{4E} L\right) \tag{1.10}
$$

Finally, the neutrino oscillation probability is given by:

$$
P_{\nu_\mu \to \nu_\tau} = \sin^2 2\theta \sin^2\left(\frac{1.27 \Delta m^2 (\mathrm{eV}^2) L(\mathrm{km})}{E_\nu(\mathrm{GeV})}\right) \tag{1.11}
$$

where E_ν is the neutrino energy, θ is the mixing angle between the flavor eigenstates and the mass eigenstates, and Δm^2 is the mass-squared difference of the neutrino mass eigenstates.

1.2 Atmospheric neutrino

The primary cosmic ray particles, mainly protons and alpha particles, are coming into the atmosphere of the earth continuously. They interact with air nuclei and create secondary mesons, mostly pions and kaons. Atmospheric neutrinos are produced via the decay of secondaries, especially charged pions and muons:

$$
\begin{aligned}
\pi^\pm &\rightarrow \mu^\pm + \nu_\mu(\bar{\nu_\mu}) \\
& \quad\; \mu^\pm \rightarrow e^\pm + \nu_e(\bar{\nu_e}) + \bar{\nu_\mu}(\nu_\mu) \\
K^\pm &\rightarrow \mu^\pm + \nu_\mu(\bar{\nu_\mu}) \\
& \quad\; \mu^\pm \rightarrow e^\pm + \nu_e(\bar{\nu_e}) + \bar{\nu_\mu}(\nu_\mu)
\end{aligned}
$$

Through those decay chains, the expected ratio of numbers of $(\nu_\mu + \bar{\nu_\mu})/(\nu_e + \bar{\nu_e})$, or simply ν_μ/ν_e, should be about two at the low energy region($\sim$ 1GeV). At higher neutrino energy, this ratio becomes greater than two because flight distances of pions and muons become longer and there is less chance for the muons to decay into electron neutrinos. Further, neutrinos easily traverse the entire earth with little or no attenuation, because of their very small cross-section.

Since downward going neutrinos are produced directly above the detector and upward going neutrinos are produced on the opposite side of the Earth, neutrino flight distances vary from 15 km to to 13,000 km. The measurement of atmospheric neutrinos can be sensitive to the neutrino oscillation parameter Δm^2 down to 10^{-4} eV^2.

1.3 Neutrino oscillation experiment

1.3.1 Atmospheric neutrino experiment

The energy spectrum of the atmospheric neutrinos peaks at $\sim$1 GeV and extends to 100's of GeV. Almost all the detectors are located in the deep underground to reduce cosmic ray backgrounds. Atmospheric neutrinos have been observed from the 1980's the following experiments: Kamiokande, Super-Kamiokande, IMB, Soudan2, Fréjus and Nusex, which are classified into two types.

IMB[17, 18], Kamiokande[19, 20] and Super-Kamiokande[21, 22] are imaging water Cherenkov detectors consist of a large volume of clear water surrounded by walls of photo-multiplier tubes (PMTs) to detect the Cherenkov radiation. These detectors were originally built to search for proton decay. Since protons have extremely long life-times. The search for proton decay requires a large detector over a long term operation. For this purpose, units of kilo-ton years are used to compare the exposures of various experiments. The water Cherenkov detector is suited for such massive experiment because it is easy to enlarge the mass of the detector.

The other experiments, Soudan2[23], Fréjus[24] and Nusex[25] were the tracking detectors which detect the tracks of charged particles. This type of detector directly tracks the path of high energy charged particles by the interactions of neutrinos. Plates of iron are sandwiched between electronic counters such as proportional tubes or streamer tubes that record the successive positions of the particle's tracks from plate to plate.

Since the predicted total flux of atmospheric neutrinos has $\sim$20% uncertainty, the comparison of absolute flux is difficult. Then these experiments usually report a double ratio $R \equiv (N_\mu/N_e)_{DATA}/(N_\mu/N_e)_{MC}$ where N_μ is the number of muon-like events and N_e is the number of electron-like events. The $(\nu_\mu+\nu_{\bar{\mu}})/(\nu_e+\nu_{\bar{e}})$ ratio is predicted with only $\sim$5% uncertainty because most of these uncertainty are canceled. Table 1.2 shows R values measured by these experiments.

In the year of 1988, Kamiokande group reported the anomaly in atmospheric neutrino flavor ratio R which was found to be only $\sim$60% of the expected value. The R value significantly lower than one, known as the atmospheric neutrino anomaly, is confirmed by IMB and Soudan 2 experiments. Fréjus and Nusex experiments agreed with the R value $\sim$1. This result were different from the other experiments, but the statistical errors

Experiment	Interaction	Exposure(kt-yr)	R (stat.+ syst.)
IMB	Water	7.7	$0.54 \pm 0.05 \pm 0.012$
Kamiokande(Sub-GeV)	Water	8.2	$0.60\ ^{+0.06}_{-0.05} \pm 0.05$
(multi-GeV)	Water	8.2(FC) 6.0(PC)	$0.63 \pm 0.03 \pm 0.05$
Super-Kamiokande(Sub-GeV)	Water	33	$0.65 \pm 0.05 \pm 0.08$
(multi-GeV)	Water	33	$0.57\ ^{+0.08}_{-0.07} \pm 0.07$
Nusex	Iron	0.74	$0.99\ ^{+0.35}_{-0.25}$
Fréjus	Iron	2.0	$1.00 \pm 0.15 \pm 0.08$
Soudan 2	Rock	3.9	$0.64 \pm 0.11\ ^{+0.06}_{-0.05}$

Table 1.2: Summary of atmospheric neutrino experiments. The first error in R values shows statistical error and the second shows systematic error.

of their measurement were large compared with Kamiokande and IMB. Kamiokande also reported that the deficit of muon events had the zenith angle dependence.

Also, as an experiment result of upward muon events, BAKSAN[26], KAMIOKANDE[27, 28] and IMB[29] reported that the observed number of upward-going neutrinos is consistent with the expected number. However MACRO[30] reported the observed neutrinos smaller than expected significantly. Results of the angular distribution from Kamiokande, MACRO, and Super-Kamiokande[31, 32] are consistent with the neutrino oscillation $\nu_\mu \rightarrow \nu_\tau$.

In 1998, Super-Kamiokande reported the strong distortion of muon-like event zenith angle distribution using contained events, and presented the evidence that the atmospheric neutrino data are consistent with two flavor $\nu_\mu \rightarrow \nu_\tau$ oscillations. by which the atmospheric neutrino anomaly was solved.

1.3.2 Solar neutrino

The sun generates energy by thermonuclear fusion in its core. The neutrino energy range is from hundreds of keV to 15 MeV. The search for ν_e disappearance by the solar neutrino detection is sensitive to oscillations with Δm^2 down to $\sim 10^{-11}\text{eV}^2$.

The solar neutrinos were observed by the following experiments: Homestake[33], Kamiokande[34], SAGE[35] and GALLEX[36]. Homestake is the first solar neutrino experiments started in 1965. From the reaction $\nu_e + {}^{37}\text{Cl} \rightarrow e^- + {}^{37}\text{Ar}$ with the threshold energy of 814 keV, the number of the produced Ar atoms was measured in the detector filled with C_2Cl_4. In the Kamiokande experiment, solar neutrinos were detected thorough the measurement of recoil electrons $\nu_i + e^- \rightarrow \nu_i + e^-$ in elastic scattering. The threshold was 7.0 MeV. Both of Galium radiochemical experiments, SAGE and GALLEX, were started in 1990's. They used a neutrino absorption reaction $\nu_e + {}^{71}\text{Ga} \rightarrow e + {}^{71}\text{Ge}$. The

Experiment	Themal power[GW]	Distance [m]
Gösgen	2.8	37.9, 45.9, 64.7
Bugey	2.8	13.6, 18.3
CHOOZ	8.5	1000
Palo Verde	11.63	750, 890
KamLAND	25	$\sim$180$\times$10^3

Table 1.3: Summary of reactor neutrino experiments.

reaction threshold energy is 233 KeV. All these experiments reported that the observed number of neutrinos was significantly smaller than expected. Super-Kamiokande started in 1996 has observed the solar neutrinos by the same interaction as in Kamiokande and reported no statistically significant energy spectrum distortion and day-night flux distance. The SNO[38] experiment started in 1999 is heavy water(D_2O) Cherenkov detector and measured the pure charge current interaction $\nu_e + n \rightarrow e^- + p$. In 2001, SNO experiment reported that the solar neutrino problem was explained by $\nu_e \rightarrow \nu_x (x = \mu, \tau)$ oscillations by computing ν_e charged current rate of SNO and $\nu_x e^- (x = e, \mu, \tau)$ interaction rate of Super-Kamiokande.

1.3.3 Reactor experiment

Nuclear reactors produce electron anti-neutrinos in nuclear fissions of ^{235}U, ^{238}U, ^{29}Pu and ^{241}Pu with a mean energy of $\sim$ 3 MeV. The anti-neutrinos are detected by the reaction $\bar{\nu_e}$+p$\rightarrow e^+$+n. The disappearance channel $\bar{\nu_e} \rightarrow \bar{\nu_x}$ can be studied because of the low neutrino neutrino energy.

Table 1.3 shows the overview of the reactor experiment: Gösgen[39], Bugey[40], CHOOZ[41] and Palo Verde[42]. All these experiments obtained no evidence for neutrino oscillation $\bar{\nu_e} \rightarrow \bar{\nu_x}$.

But in 2002, KamLAND announced the detection of the deficit of electron anti-neutrinos from reactors at a mean distance of 175 km in Japan. The results combined with all the earlier solar neutrino results establish the correct parameters for the solar neutrino deficit.

1.3.4 Accelerator experiment

At high-energy accelerators, intensive ν_μ and $\bar{\nu_\mu}$ beams are mainly generated from decays of pions produced by collisions of protons with a target.

Accelerator experiments are categorized into the ν_μ disappearance, and ν_e or ν_τ appearance. The ν_τ appearance can be studied only if the neutrino energy is above the

Experiment	source	channel	average energy	Distance(far)[m]
FNAL-E776	$\bar{\nu}_\mu(\nu_\mu) \to \bar{\nu}_e(\nu_e)$	appearance	1.4 GeV	1km
LSND	$\bar{\nu}_\mu(\nu_\mu) \to \bar{\nu}_e(\nu_e)$	appearance	50 MeV	30 m
CHARM	$\nu_\mu \to \nu_e$	appearance	1.5 GeV	903 m
KARMEN	$\bar{\nu}_\mu \to \bar{\nu}_e$	appearance	29.8 MeV	17.7 m
CDHSW	$\nu_\mu \to \nu_e$	disappearance	1 GeV	885 m
FNAL-E531	$\nu_\mu \to \nu_\tau$	appearance	25-30 GeV	950 m
CHORUS	$\nu_\mu \to \nu_\tau$	appearance	27 GeV	15 m
NOMAD	$\nu_\mu \to \nu_\tau$	appearance	23.5 GeV	600 m
K2K	$\nu_\mu \to \nu_\tau$	disappearance	1.4 GeV	250 km

Table 1.4: Summary of accelerator neutrino experiments.

threshold for τ production(~3.6GeV).

FNAL-E776[43] and LSND[44] searched for ν_e and $\bar{\nu}_e$ appearances, and CHARM[45] and KARMEN[46] searched for ν_e and $\bar{\nu}_e$ appearances, respectively. LSND reported the evidence for $\nu_e(\bar{\nu}_e)$ appearance from pure beams of $\nu_\mu(\bar{\nu}_\mu)$ with $\Delta m^2 \sim 1\text{eV}^2$ and $\sin^2 2\theta \sim 10^{-2}$ by using liquid scintillator. But this result has not been confirmed by the other experiments.

FNAL-E531[47], CHORUS[48], NOMAD[49] searched for the ν_τ appearances. No evidence was found.

CDHSW[50] seached for the ν_μ disappearances. No evidence was found. Recently KEK-E362(K2K) experiment reported $\nu_\mu \to \nu_\tau$ oscillation which is consistent to atmospheric neutrino oscillations in Super-Kamiokande.

1.3.5 Summary of neutrino oscillation experiments

Figure 1.1 shows the contour plot of $\nu_\mu \to \nu_e$ oscillation and Figure 1.2 shows the contour plot of $\nu_\mu \to \nu_\tau$ oscillation.

1.4 Atmospheric neutrinos in Super-Kamiokande

Super-Kamiokande is a cylindrical 50-kiloton ring imaging water Cherenkov detector and detects Cherenkov light photons generated by charged particles which propagate in water. The atmospheric neutrino measured in Super-Kamiokande groups into following types by the neutrino interaction point, contained e$\cdot\mu$ events and upward-going muon events. Figure 1.3 shows the schematic view of atmospheric neutrino events.

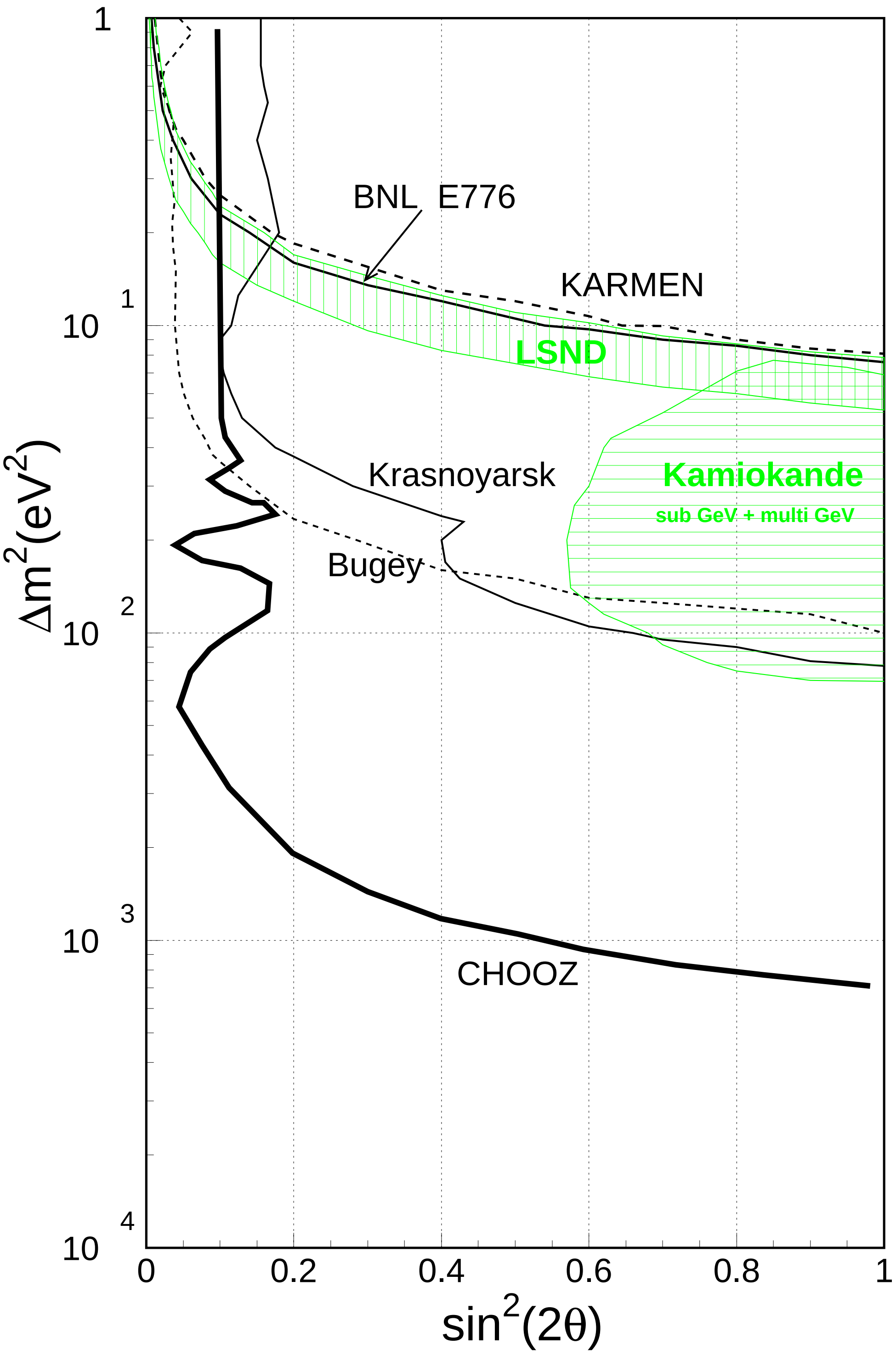

Figure 1.1: Allowed(shaded areas) and excluded(lines) regions of parameter space for $\nu_\mu \to \nu_e$ or $\bar{\nu}_\mu \to \bar{\nu}_e$ oscillations. The excluded regions lie on the right side of curves.

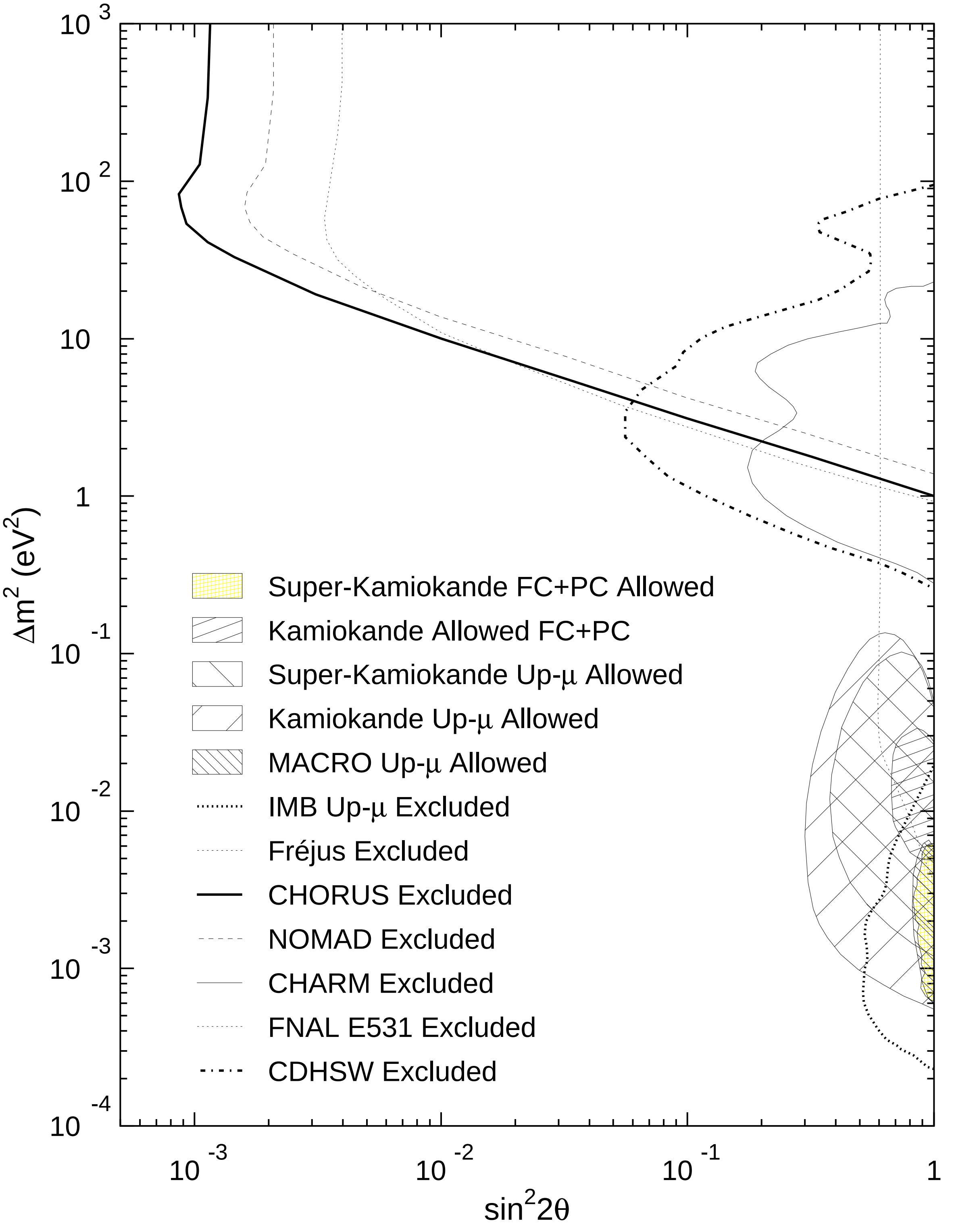

Figure 1.2: Allowed and excluded regions of parameter space for $\nu_\mu \rightarrow \nu_\tau$ or $\nu_\mu \rightarrow \nu_x$ oscillations. The excluded regions lie on the right side of curves.

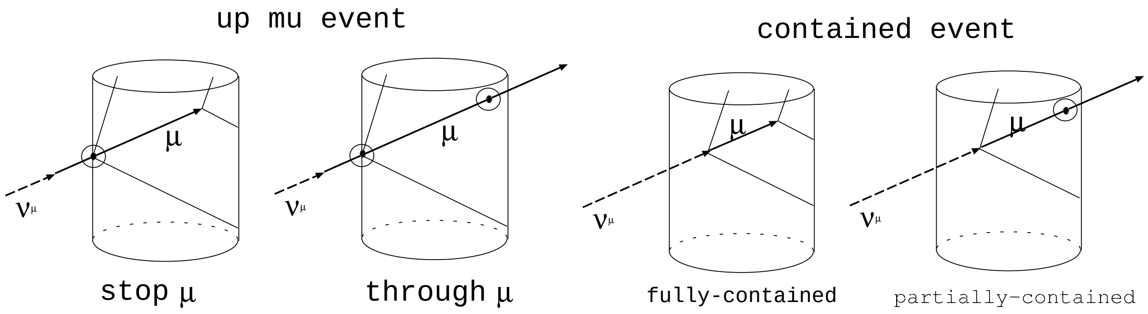

Figure 1.3: The schematic view of atmospheric neutrino events, upward stopping muon event, upward through-going muon event, fully-contained event and partially-contained event, respectively. Circle means the OD hit.

1.4.1 Contained e·μ events

The electron or muon event in which atmospheric neutrinos interact water(O_2) is called as the contained event. An event such that the whole track of charge particle are contained is classified as a fully-contained(FC) event. The particle identification is applied for a Cherenkov ring of FC events and tagged as μ-like or e-like, corresponding to ν_μ and ν_e induced events. In contrast to the FC event, an event such that the vertex of event is within the inner detector and the track of charged particle reached the outer detector is classified as a partially-contained(PC) event. The typical parent neutrino energy of FC and PC are ∼1GeV and ∼10GeV, respectively.

1.4.2 Upward-going muon events

Upward-going muon events also provide the alternative method to observe atmospheric neutrinos. Some atmospheric muon neutrinos interact with the rock surrounding the detector, then muons are produced by charged current interaction. These neutrino-induced muons propagate to the detector in the rock. Since electrons are hardly penetrating particle, only muons can reach the detector.

Downward muons induced by atmospheric neutrinos cannot be distinguished from cosmic-ray muons. But there is no contamination with cosmic-ray muons in the upward muons because muon in the rock cannot travels more than 10 km correspond to the thickness for the horizontal direction. Neutrino-induced muons can be observed as the upward-going directional event, so that they are called as upward-going muons.

Upward-going muons are classified into two types, though-going muons and stopping muons. An event penetrating the detector is called as a through-going muon, and an event stopping inside the detector is called as a stopping muon . Figure 1.4 shows the

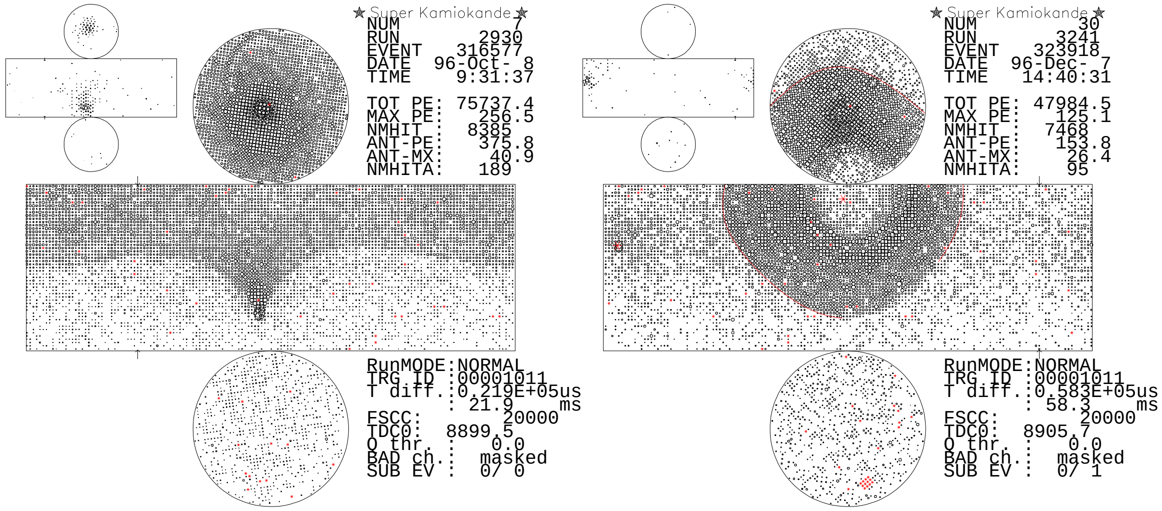

Figure 1.4: The typical event display of upward muons. The left figure shows the upward through-going muon. The right shows the upward stopping muon. The lager display is inner-detector and the smaller display is outer-detector.

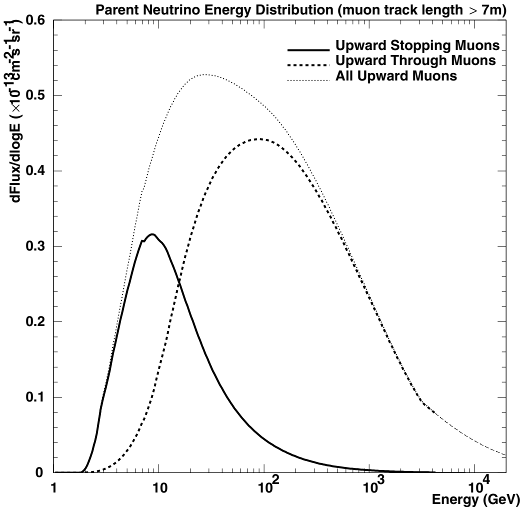

Figure 1.5: Energy distribution of parent neutrino ($\geq$1.6GeV) for upward muons.

event display of upward muons in Super-Kamiokande. As shown in Figure 1.5, the typical neutrino energy of upward through-going and stopping muons are ~10 and ~100 GeV, respectively.

In upward-going muon samples the neutrinos are ideally background free. Upward-going muons keep their direction of parent neutrinos with good accuracy at higher energy (~2^o at 100 GeV).

1.5 Motivation of this thesis

This thesis aims at the analysis of the neutrino oscillation parameter and verifies the oscillation in the energy region of the multi-GeV contained event or in the higher energy region by investigating the angular distribution independently using the upward-going events.

Using upward through-going muon events, neutrino oscillation can be verified in the energy region of 100 GeV or much higher. And the typical neutrino energy of upward stopping muon events is about 10GeV, which is the same energy region of multi-GeV contained event in Super-Kamiokande. Thus upward stopping muon events can verify the neutrino oscillation independently.

Since upward-going muon neutrinos interact rock near the detector in contrast to contained events in which neutrinos interact water(O_2), the atmospheric neutrino oscillation can be verified when the target of neutrino interaction is the rock.

In the previous analyses[31, 32], the direction was decided by manual reconstruction. In this analysis, the direction is reconstructed automatically. This automatic reconstruction can remove the human bios. Moreover, the automatic reconstruction is useful for many events because it is necessary to generate so many Monte calro events to reduce the statistical error.

This study reports the oscillation analysis of upward through-going muons and stopping muons induced by the atmospheric neutrino, which has been obtained during the all Super-Kamiokande data(SK-I) of more than 1600 days observation.

Chapter 2

Super-Kamiokande detector

The Super-Kamiokande detector is a cylindrical 50-kiloton ring imaging water Cherenkov detector, and provided this analysis with data for over five years period between Apr,1996 and July,2001. The main target of this experiment is search for proton decays [1] and study of the neutrinos [2] from atmosphere, solar and astrophysical sources such as supernovae and gamma ray burster. Moreover, Super-Kamiokande is the detector of long baseline ν_μ beam experiment called K2K.

2.1 Detection Method

Super-Kamiokande detects Cherenkov photons, by Photo Multiplier Tubes(PMTs) as shown in Figure 2.1. Cherenkov photons are emitted when a charged particle travels faster than at the light velocity in a medium c/n, where c is the light speed in vacuum and n is the refractive index of the medium. Cherenkov photons are emitted in a cone with a half opening angle θ towards the direction of the particle track. θ is determined

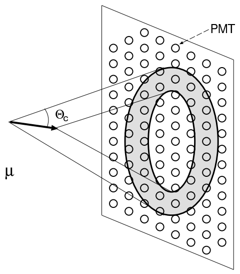

Figure 2.1: Detection of Cherenkov ring by PMTs

---

[1] KAMIOKA Nucleon Decay Experiment
[2] KAMIOKA Neutrino Detection Experiment

as follows,

$$\cos\theta = \frac{1}{n\beta} \tag{2.1}$$

where β is equal to v/c. For β=1 ,θ is about 42 degrees in water(n=1.33). The number of Cherenkov photons, N, as a function of the wavelength,λ, is given by

$$\frac{d^2N}{dxd\lambda} = \frac{2\pi\alpha}{\lambda^2}\left(1 - \frac{1}{n^2\beta^2}\right) \tag{2.2}$$

where α=1/137 is the fine structure constant and x is the path length of the charged particle. The number of Cherenkov photons emitted by a charged particle with β =1 in the wavelength range of 300~600 nm, which is the sensitive region of our PMT, is about 340 per cm.

Since the energy of a charged particle is estimated based on the above relation, the energy of the charged particle is determined from the total number of Cherenkov photons. Moreover the number of charged particles is measured from the number of the Cherenkov rings on the detector wall. In addition, it is possible to identify the particle type by using the photon distribution in the Cherenkov ring. Thus, the vertex position, number of Cherenkov rings, direction, momentum and particle type of the charged particle which produced each Cherenkov ring can be reconstructed by computers based on the information of the photon arrival-time and pulse height from each PMT.

2.2 Detector features

Super-Kamiokande is located 1000 m underground in the Kamioka Observatory in the Kamioka mine in Gifu Prefecture, Japan. The average rock overburden above this detector is 2,700 meters-water-equivalent(m.w.e.). The latitude and longitude are 36°25′N and 137°18′E, respectively. At this depth, the cosmic ray muon flux is reduced by a order of 4~5 of that of the surface. The trigger rate due to cosmic-ray muons is about 2.2 Hz.

Figure 2.2 shows a schematic view of Super-Kamiokande. The detector is filled with pure water of 50,000 tons in a stainless steel tank of 39.3 m in diameter and 41.4 m in height. The two type of photo-multipliers (PMTs) are attached in the opposite direction on the stainless framework 2.5m inside the outer wall. The detector is separated into two parts; the inner detector(ID) and the outer detector(OD) which are optically separated by a pair of opaque sheets which enclose a insensitive region of ~55cm in thickness as shown in Figure 2.3. This division contributes to identify entering cosmic-ray muons, to shield gamma ray and neutrons from the rock, and to identify exiting particles.

The ID is 36.2 m in height and 33.8 m in diameter and 32,000 ton in volume. The 11146 20-inch PMTs are uniformly arranged in the inner detector towards an inner side. The ID PMTs are placed at intervals of 70 cm grid, and the photocathode coverage is

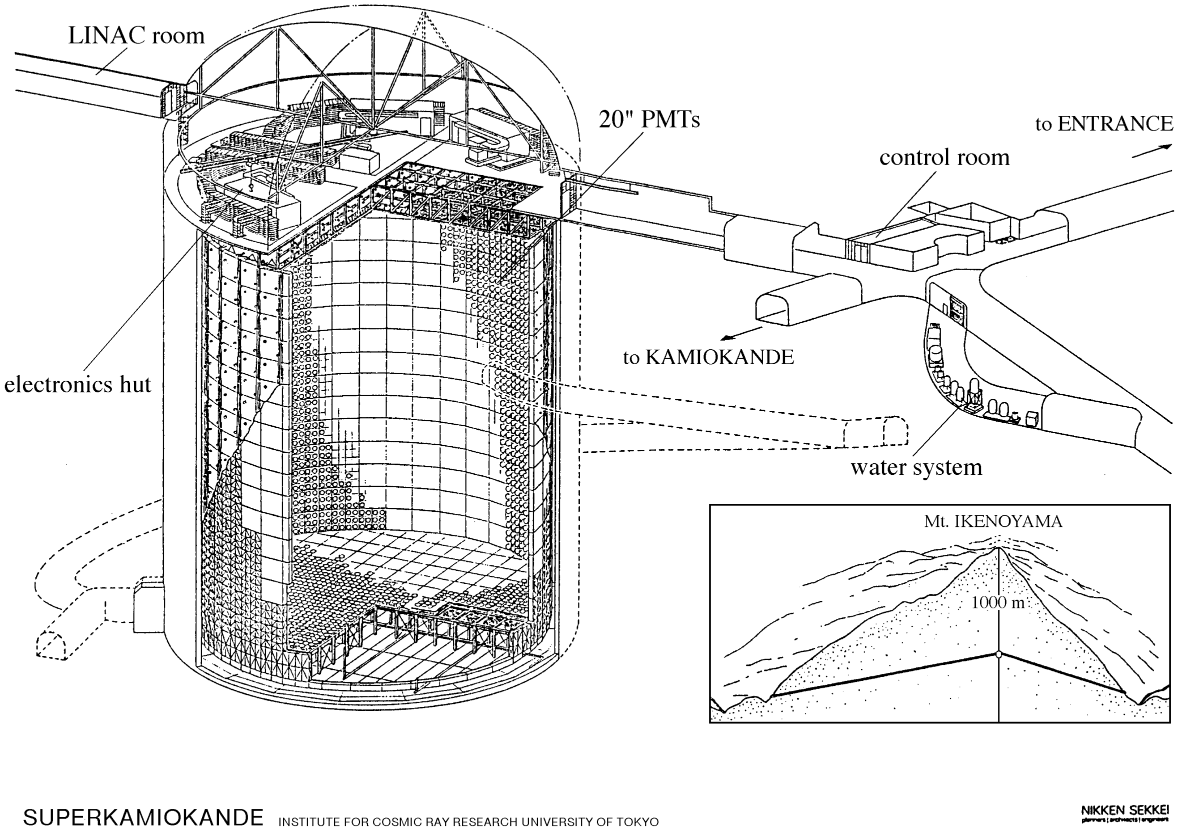

Figure 2.2: The Super-Kamiokande detector. Inset at bottom right shows the location.

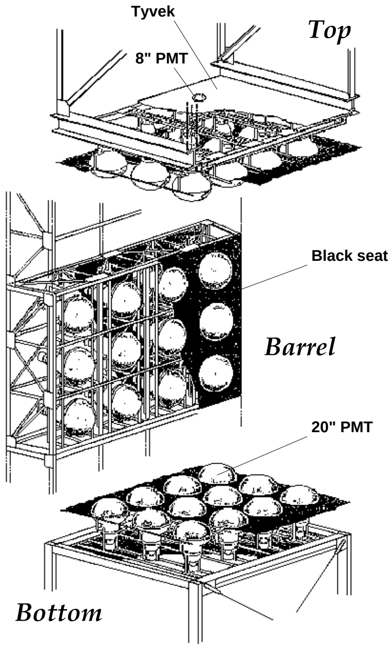

Figure 2.3: The schematic view of the frame which supports PMTs.

Tank	Dimensions	39.3m(diameter), 41.4m(height)
	Volume	50,000 ton
ID	Dimensions	33.8m(diameter), 36.2m(height)
	Volume	32,000 ton
	Size of PMT	20 inch
	Num.of PMTs	1748 (top,bottom), 7650 (side)
	Coverage	40 %
OD	Thickness	2.6m(top,bottom), 2.75m(side)
	Volume	18,000 ton
	Size of PMTs	8 inch
	Num.of PMT	302(top), 308(bottom) and 1275(side)
Photo insensitive	Dimensions	2.6∼2.75 m from OD wall
	Thickness	55 cm

Table 2.1: Performance of the Super-Kamiokande detector.

about 40 %. The surface of the ID is covered with black polyethylene terephtalate sheets called "black sheet" lined with the gaps of the inner PMT's photo cathode as shown in Figure 2.2. The 1885 8-inch outward facing OD PMTs are mounted with wavelength shifter plates which increase photo coverage. To maximize the light detection efficiency, all surfaces of the OD are covered with white Tyvek sheets with a reflectivity of above 80 %. The thickness of the OD water including the dead region is 2.6∼2.75 m.

The several parameters of Super Kamiokande are summarized in Table 2.1

2.2.1 Inner PMT

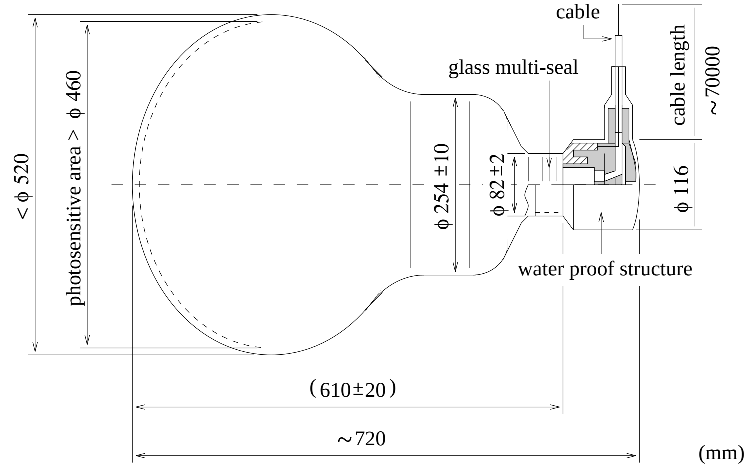

Figure 2.4: The schematic view of the PMT used in Super-Kamiokande.

Figure 2.4 shows a schematic view of the 20-inch PMT(HAMAMATSU R3600). The original PMT was made by Hamamatsu Photonics Company for Kamiokande. It was improved in the dynode shape: the bleeder chain to attain better timing and energy resolutions for Super-Kamiokande.

The photo-cathode is made of bialkali(Sb-K-Cs) that is suited for the collection of Cherenkov light. The quantum efficiency of the 20-inch PMT shown in Figure 2.5 is 21 % at the wave length σ=400 nm which is the typical wave length of Cherenkov light. The collection efficiency for photoelectrons at the first dynode is over 70 %. The single

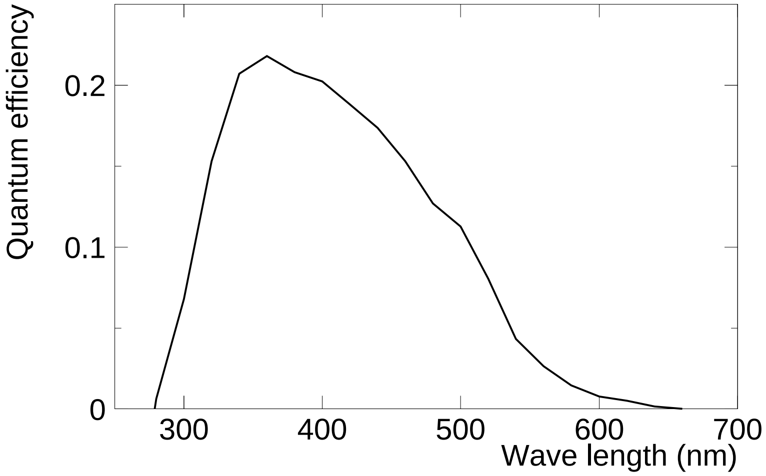

Figure 2.5: The quantum efficiency as a function of the wavelength of the light.

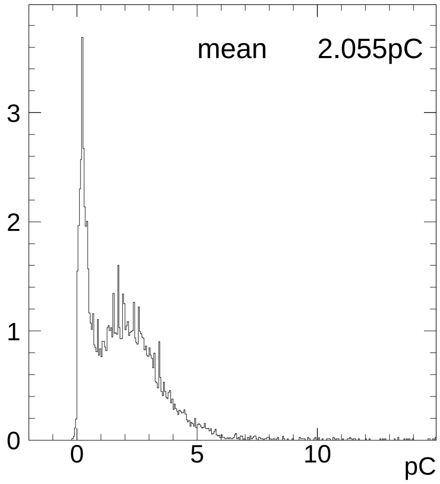

Figure 2.6: Single photo-electron distribution of the PMT used in Super Kamiokande.

Photo-cathode area	50cm in diameter
Shape	Hemispherical
Window material	Pyrex glass (4∼5mm)
Photo-cathode material	Bialkali
Dynodes	11 stage, Venetian blind
Pressure tolerance	6kg/cm^2 water proof
Quantum efficiency	22% at λ =390nm
Gain	10^7 at ∼2000 Volt
Dark current	200nA at gain=10^7
Dark pulse rate	3kHz
Cathode non-uniformity	less than 10 %
Anode non-uniformity	less than 40 %
Transit time spread	σ ∼2.2 nsec

Table 2.2: The properties of the 20-inch ϕ PMT

photo electron peak can be seen clearly as shown in Figure 2.6. The transit time spread for a 1 p.e. signal is 2.2 nsec. The average dark noise at the 0.25 p.e. threshold is about 3 kHz. The ID PMT are operated with gain of about 10^7 at a supply high voltage rating 1,700-2,000 V.

The large PMT is sensitive to external magnetic fields. To compensate for the geomagnetic field which is about 450mG at the Super-Kamiokande site. the 26 sets of Helmholtz coils located at the surface of the tank to reduce the magnetic field inside the tank to less than 100 mG.

Properties of the PMT are summarized in Table 2.2. The details of the 20-inch PMT are presented in [51, 52].

2.2.2 Outer PMT

The outer detector is viewed by 1885 8-inch PMTs(Hamamatsu R1480), which were used at the IMB experiment[17]. A 6cm×6cm×1.3cm wavelength shifter plate is optically coupled to each 8-inch PMT in order to enhance light collection efficiency. These plates absorb Cherenkov light and re-emit photons isotropically at a slightly longer wavelength.

The wave length shifter plate makes the light collection increase by 60%. The timing resolution of the PMT itself is ∼5.5nsec, but goes down to ∼7.5nsec with the wavelength shifter[53]. Figure 2.7 shows the anti-counter PMT and wave length shifter.

To further enhance light collection, the OD volume is lined with a reflective material, Tyvek.

These PMTs typically operate at gains near 10^8 with ∼2kV supply voltage.

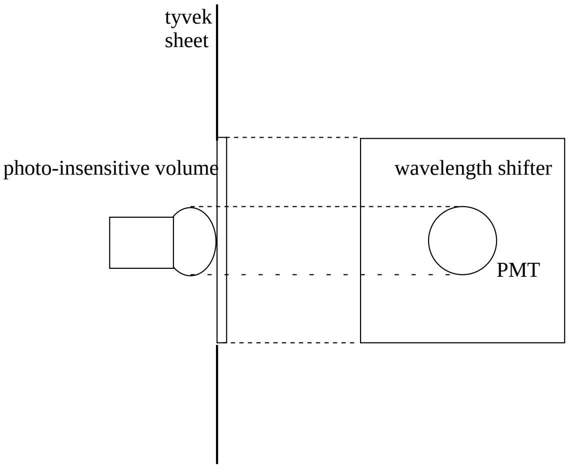

Figure 2.7: The schematic view of the anti-counter PMT and wave length shifter

2.3 Electronics and data acquisition

2.3.1 Inner detector electronics and data acquisition

Figure 2.8 shows a block diagram of the electronics system for the ID. The system has two types of modules, TKO modules[55] and VME modules. 48 TKO and 8 VME modules are housed in 4 electronics huts on top of the detector. Additionally one VME module is located in the central hut for the global trigger(TRG module). Each PMT signal of ID is connected to a front-end electronics module called ATM (Analog Timing Module)[54], which records the integrated charge and arrival time. Each ATM accepts 12 input channels. And 20 ATMs, one GONG module and SCH module are included in each TKO box. A GONG module distributes control signals as a master module to its slave module. A SCH module is a bus-interface module between TKO and VME. A total of 934 ATMs are used for inner detector. Figure 2.9 shows a schematic view of the analog input block of the ATM. ATM has a pair of switching channel There are two pairs of Time-Analog Converters(TAC) and Charge-to-Analog Converters(QAC) to measure the time and charge of an input pulse. TAC provides 1.2 μsec full range in time, 0.3 nsec resolution, and QAC provides 550 pC full range with 0.2 pC resolution. If one channel is not available, the other one can be used instead. This structure enables us to detect a decay electron signal from a muon, which is very important for several analyses on the atmospheric neutrino or proton decay.

Another function of ATM is to make trigger signals. Figure 2.10 shows a schematic view of trigger generation. When the PMT signal exceeds the threshold value($\sim$1/4 p.e.), the discriminator generates a HIT pulse with 200 nsec width and 11 mV/channel height. A HITSUM signal which are summed up of HIT pulses with all channels in the ATM is sent to the central hut to generate a global trigger.

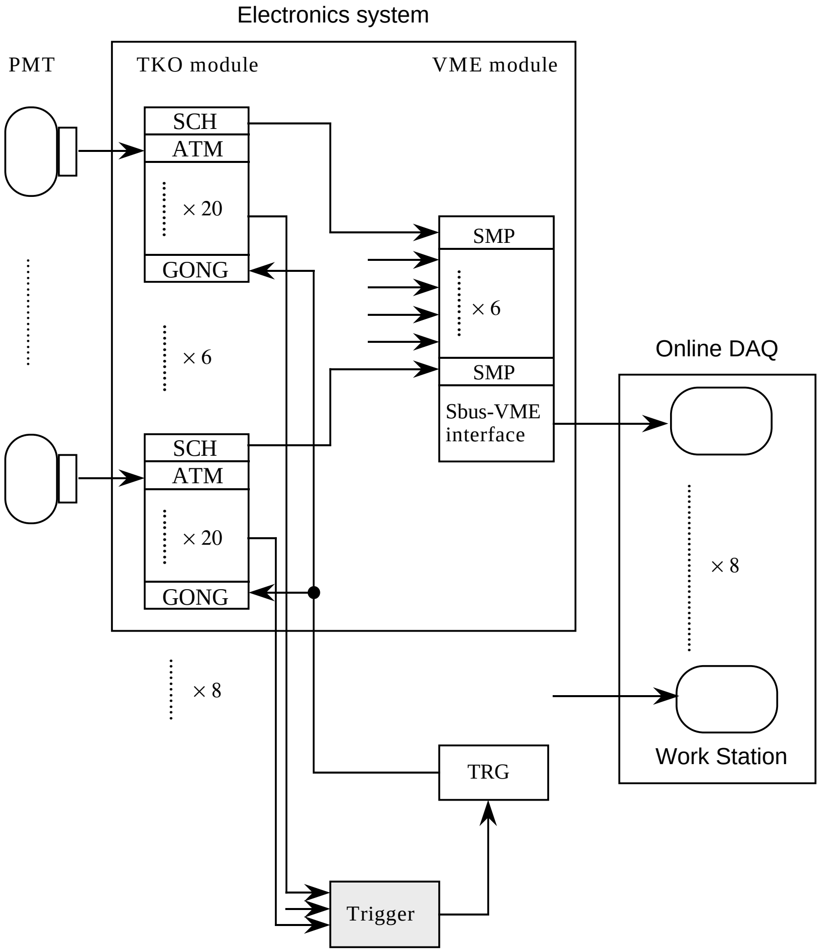

Figure 2.8: The block diagram of the data acqusasition system for the ID.

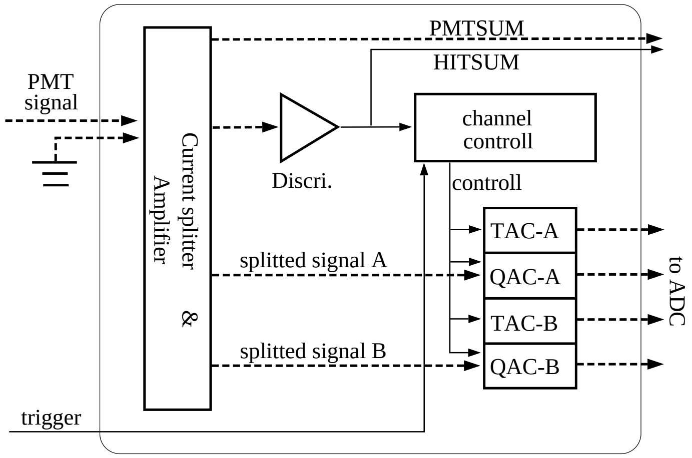

Figure 2.9: The block diagram of the analog input block diagram of the ATM. This figure shows only one channel.

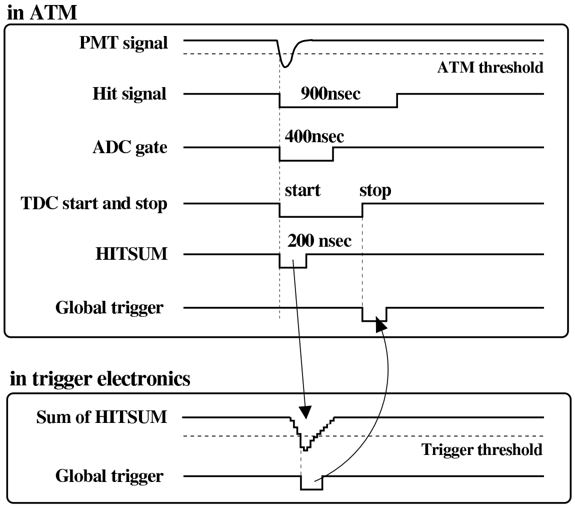

Figure 2.10: The trigger generation and timing in a ATM.

At the same time, one of the splitted signals is sent to a QAC and TAC. The TAC starts to measure the time, and the QAC accumulates the charge in the 400 nsec time window and stores it until the global trigger arrives . If the global trigger arrives within 1.3 μsec after the HIT pulse, the charge(timing) information in QAC(TAC) is digitized by ADC(TDC) and is sent to SMP in the VME module through the SCH module. Finally data are set to 8 online computers.

At every 30 minutes, pedestals of ATMs are measured. For every 1/8 section of detector, ATMs are measured in turn to prevent whole detector from being insensitive.

2.3.2 Outer detector electronics

Figure 2.11 shows the front-end modules for a quarter of OD electronics system. It consists of 40 paddle cards, 10 charge-to-timing converters(QTCs) modules, 5 time-to-digital converters(TDCs) and one FASTBUS smart crate controller(FSCC) in each electronics hut. Each TDC has 96 input channels, corresponding to the total of 1,920 TDC channels.

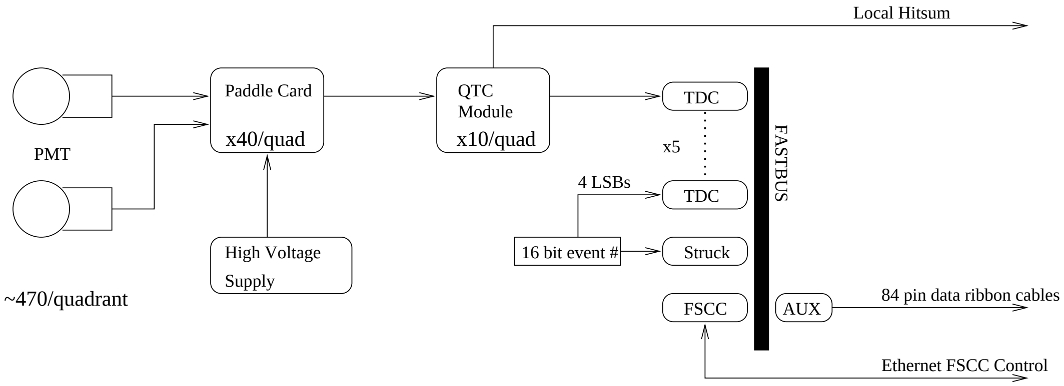

Figure 2.11: The block diagram of the data accusation system for the OD.

The paddle card accepts 12 PMT channels. The signal and high voltage lines are AC coupled, so that this card plays a role in picking off the PMT signals through a high voltage capacitor.

Signals from a OD PMT are sent to a QTC module which generates a logic pulse(ECL level), whose leading edge marks the hit arrival time and whose width represents the integrated charge of the PMT pulse proportionally. The QTC module also provides a HITSUM signal with 200 nsec width and 20 mV pulse like as inner detector.

The ECL pulses from the QTC are digitized in the LeCroy model 1887 multi-hit TDC, which records the start and stop time. Each TDC channel works as a circular buffer that can store latest 8 QTC pulses with a resolution of 0.5 nsec over a window of up to 32 μsec width. The timing of the signal window was set to the full 32 μsec centered around the trigger time for the early period of the operation, but after September 1996, this width is set to 10 μsec before and to 6 μsec after a global trigger in order to reduce the data size.

The TDC signals are read by FSCC and the stored data are sent to an online computer through the VME bus.

2.4 Trigger

The Super-Kamiokande detector has 3 triggers from the inner detector, which are named as High energy(HE) trigger, Low energy(LE) trigger and Super Low energy(SLE) trigger, and 1 trigger from the outer detector, OD trigger. Each of them is triggered by its own level of HITSUM signal independently.

The HE trigger is used mainly to identify cosmic-ray muons, atmospheric neutrinos, K2K-beam neutrinos, and proton decay candidates. It requires a coincidence of 31 HITSUM signals within 200nsec time window. The trigger rate is about 5$\sim$6 Hz.

The LE trigger of which threshold is 29 HITSUM is used for solar neutrino analysis above 5$\sim$6 MeV in the energy.

The SLE trigger started from May-1997 in order to push the analysis threshold of solar neutrino energy spectrum down to 4.6 MeV.

The OD trigger is used for the rejection of the cosmic-ray muons. It is formed by the coincidence of 19 HITSUM signals from the QTC modules in the outer detector.

All trigger signals are sent to the TRG modules. A TRG module records trigger information which includes an event number, the trigger type and the timing of the trigger. The global trigger is generated independently when any of these four trigger is generated, and the data stored in memory modules is read through online workstations.

2.5 Online and offline systems

Each front-end workstation reads out the data from electronics independently, and transfers to an online host computer via FDDI. They are then sent to the offline computer located outside of the mine via an optical fiber cable. The offline host computer saves all the data in a tape library. And it converts the data to offline format, called ZEBRA[56]. This reformatted data is transferred from the detector site to the offline computer facility out of the mine, and stored to the magnetic tape library. At the same time, the data are transfered to the process called "TQREAL" and the primary reduction process. In the TQREAL process, the timing and charge information of PMTs are converted from ADC and TDC counts to units of photoelectron and nanosecond, respectively. After the primary reduction process, the reduced data are also stored to the tape library and the subsequent proper reduction is processed by each analysis group.

2.6 Water and air purification system

2.6.1 Water purification system

The 50 kton of pure water is circulated through the water purification system. The purpose of this system is to remove the radioactive material mainly like as Rn, Ra and Th, and to keep the water transparency as clear as possible by removing small dust, metal ions like as Fe^{2+}, Ni^{2+}, Co^{2+}, and bacteria.

Figure 2.12 shows the schematic diagram of the water system. In this closed cycle system, the water of 30 tons per hour are being processed at all times.

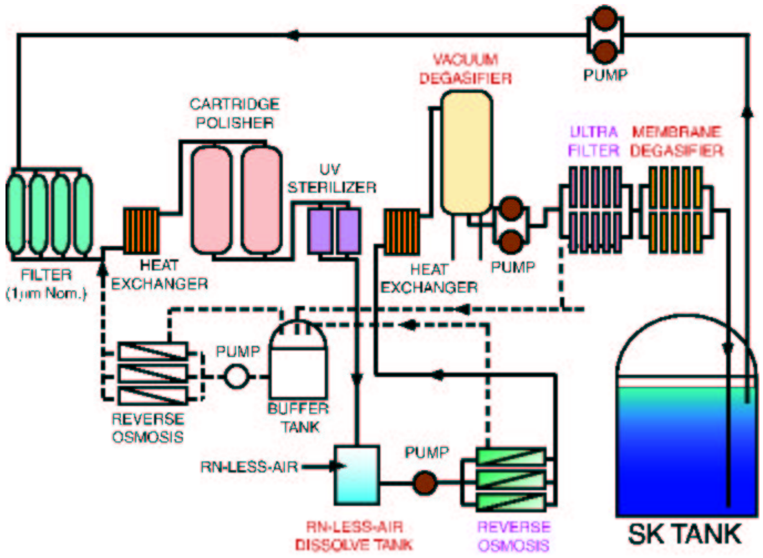

Figure 2.12: A flow diagram of the water purification system.

The 1μm filter removes large dust and particles. The heat-exchanger cools the water and keeps the temperature at around 13 °C to reduce the PMT dark noise and suppress bacteria growth. The cartridge polisher(CP) eliminates radioactive materials and heavy ions which cause to decrease the water transparency. In October 2000 ion-exchange(IEX), which was used for the same purpose as CP, was disconnected from the water flow because it was found that IEX resin was a significant radon source. The UV sterizer reduces the bacteria.

The reverse osmosis(RO) removes additional particles and the tank is used to increase the radon removal efficiency in the vacuum degasifier(VD). The VD remove gas resolved in the water.It is able to remove about 96% of the radon gas. The new RO and Rn-less-air dissolve tank was additionally installed in March 1999. The ultra filter(UF) which consists of hollow fiber membrane filters removes small dust of the order of 10 nm. The membrane degasifier(MD) removes radon dissolved in water.

Radon concentrations are monitored by several real-time radon detectors. In June 2001, the typical radon concentrations in the water are less than 2 mBq/m^3, This system keeps the water transparency above 70 m.

2.6.2 Radon free air system

Air purification system shown as Figure 2.13 consists of three compressors: a buffer tank, driers, filters, and activated charcoal filters.

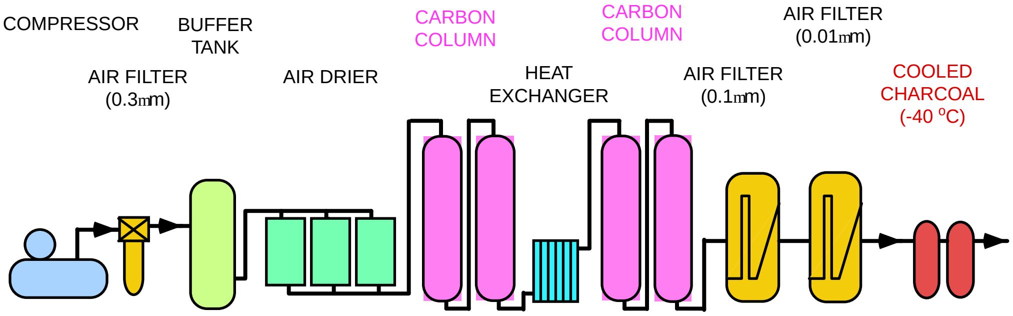

Figure 2.13: A flow diagram of the water purification system.

The radon concentration in the mine air is of order of 10∼1000 Bq/m . There is ∼60cm space between the surface of the water and the top of the water tank. Radon gas contaminated in the air in the gap could dissolve in the water. Therefore radon free air must be sent to this region.

The compressor takes in air from outside the mine and compressed to 7.0∼8.5 atm. The 0.3 μm, 0.1 μm and 0.01 μm air filters remove dusts in air. The air drier removes moisture in the gas to improve the efficiency of removing radon. This system can remove CO_2 in the gas too. The carbon column removes radon gas. The activated charcoal cooled to ∼40 °C traps the radon. The concentration of radon in the air through this system is reduced to the order of a few $\times 10^{-3}$ Bq/m^3 in all seasons.

Chapter 3

Calibration

3.1 Relative gain calibration

In order to make energy uniform measurement capability in the SK detector, it is necessary to calibrate the relative gains of all PMTs. A Xe calibration system is used to check the relative gain and the stability of gain uniformity. Figure 3.1 shows the setup of the Xe light system.

The Xe light of a lamp is irradiated to the scintillation ball in the tank via an optical fiber through an UV(Ultra-Violet) pass filter and ND(Neutral Density) filters. The UV pass filter passes only the UV light and the ND filter is used to adjust the light intensity. A scintillation ball is made of acrylic resin mixed with BBOT wavelength shifter and MgO. The BBOT absorbs the UV lights and emit the light similar to Cherenkov light wavelength. The MgO diffuses the light uniformly. The intensity of the UV light is monitored by two silicon photo-diodes and 5 cm PMT. One of the monitor outputs is used for a trigger. The charge at each PMT is corrected with PMT acceptance, light attenuation in water and non-uniformity of the scintillator ball. The value is measured at various heights of the scintillator ball and different high voltage settings. The distributions of corrected electric charge for all PMTs is shown in Figure 3.2. The relative gain of all PMTs is consistent within 7 %. The stability of the relative gain is also studied by performing 5 measurements in a year. The time variation is stable within 2 %.

3.2 Absolute PMT gain calibration

The absolute gain of PMT is calibrated by measuring a charge distribution of single photo-electron(p.e.). In order to take the single p.e. distribution, low energy gamma-rays emitted from thermal neutron capture in nickel, Ni(n,γ)Ni*, are used. The setup of Ni-Cf calibration is shown in Figure 3.3.

The cylindrical polyethylene container contains a nickel wire and pure water. A

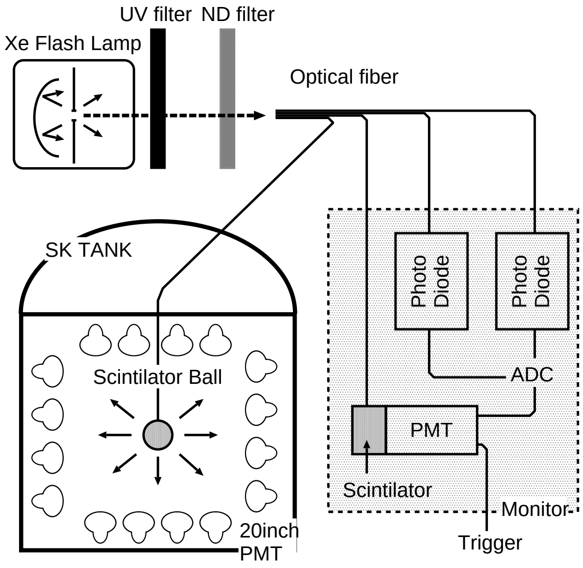

Figure 3.1: The setup of the Xe calibration system which use the Xe lamp and the scintillation ball for the relative gain calibration.

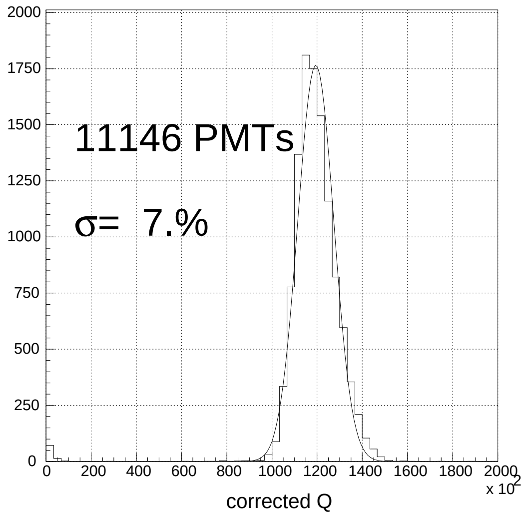

Figure 3.2: The gain spread of the ID PMTs

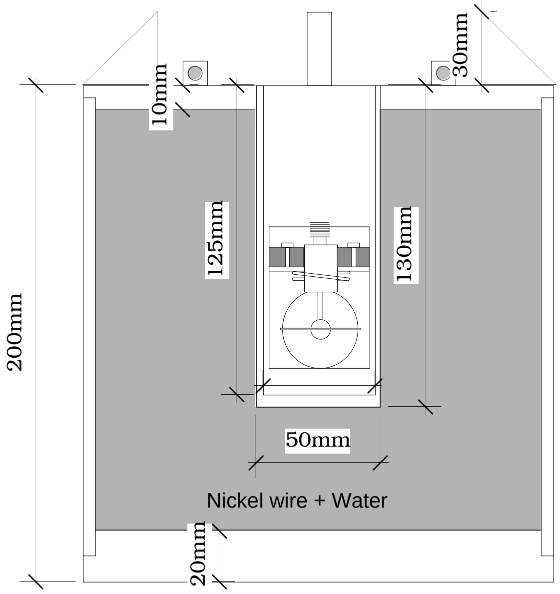

Figure 3.3: The Schematic view of the Ni-Cf calibration system.

reaction	natural abundance (%)	capture cross section (barn)	gamma energy (MeV)	intensity (%)
^{58}Ni(n,γ)^{59}Ni*	67.88	4.4	9.000	65
^{60}Ni(n,γ)^{61}Ni*	26.23	2.6	7.820	15
^{62}Ni(n,γ)^{63}Ni*	3.66	15	6.838	12
^{64}Ni(n,γ)^{65}Ni*	1.08	1.52	6.098	0.4

Table 3.1: The energy table of gamma rays for various isotopes of nickel.

proportional chamber in which ^{252}Cf source is painted on an electrode is located in the hollow space at the center of the container. ^{252}Cf decays through α decay (96.9%) and spontaneous fission (3.1%). Neutrons with averaged kinematic energy $\sim$2 MeV are produced with gamma rays of total energy $\sim$9 MeV by spontaneous fission of ^{252}Cf. The average number of the neutrons and gamma rays by a fission are 3.76 and 10.8, respectively. The emitted neutrons are thermalized by elastic collisions with protons in the pure water with the container. The thermal neutrons captured by nickel wire emit the gamma ray of a maximum energy of 9 MeV shown in Table 3.1. Since this energy is equivalent to about 80 p.e., the number of photons are almost one per PMT.

Figure 3.4 shows the typical single p.e. distribution. The mean value of this distribution is 2.055pC, which is equal to the 1 p.e. The absolute gain of the PMTs is $\sim 6\times10^6$.

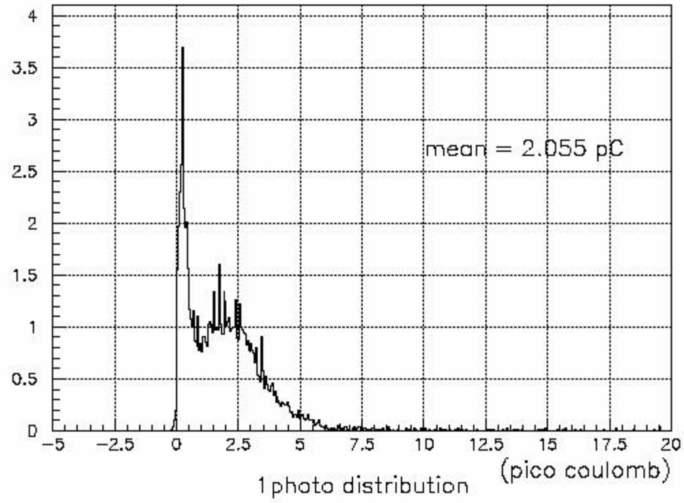

Figure 3.4: Single photo-electron distribution

3.3 Timing calibration

It is necessary for timing calibration to determine a relative time of each PMT and to correct the photo-electron dependability of time(Time-walk).

Figure 3.5 shows the setup of relative timing calibration system. A N_2 laser light of 337 nm is converted to 384 nm by a DYE laser module. The light intensity is controlled using the optical filter. The laser light is divided into two after passing an optical filter. One makes the diffused light by the diffusion ball in the water tank, and the other is injected to monitoring PMT for making a trigger signal. The same system is used for the outer detector(OD) timing calibration[57].

The timing calibration data is taken by changing the intensity of the light from the laser ball placed at the center of the tank. Figure 3.6 shows the typical 2-dimensional plot of timing and charge(TQ map). Since each PMT provides a various profile, it has own TQ map, respectively. As shown in Figure 3.7, the timing resolution is about 3 ns at single p.e. level after the correction of Time-walk as shown in Figure 3.6. The higher p.e. become earlier timing and better resolution.

3.4 Water transparency measurement

Since the bad water transparency becomes the cause of attenuating photons , it is important to measure the attenuation length. As measuring methods, two independent systems are used: direct measurement using a laser and a CCD camera and indirect measurement using cosmic-ray muon events.

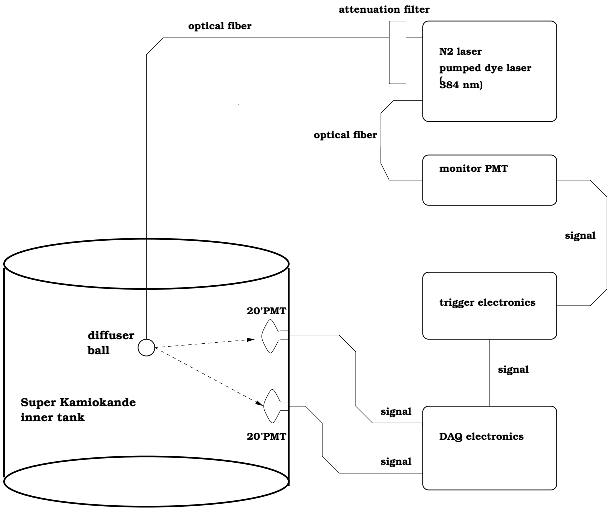

Figure 3.5: The setup of timing calibration.

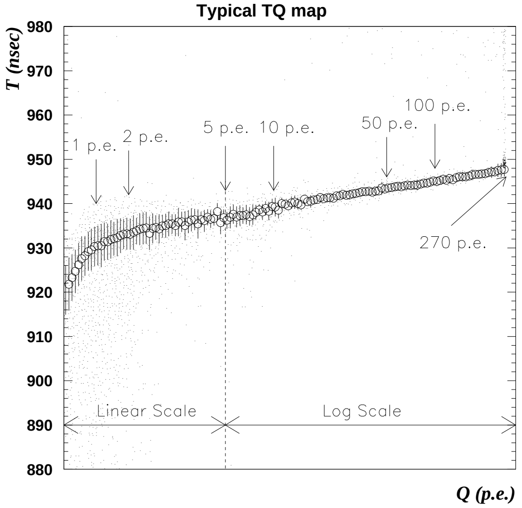

Figure 3.6: Figure of the relation between Q(p.e.) and T(nsec) for a typical PMT. Circles and error bars show peak values and resolution (1 σ level). Higher p.e. means earlier timing.

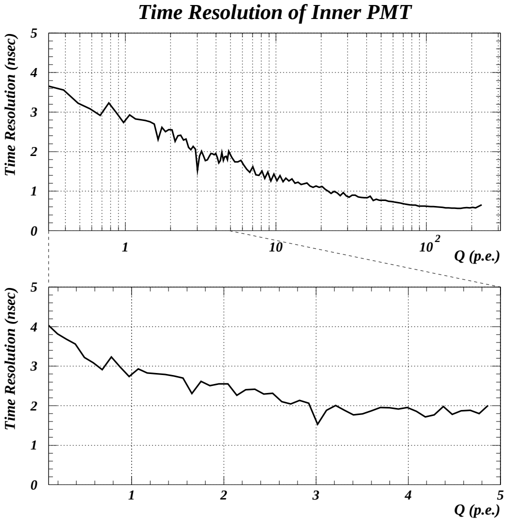

Figure 3.7: The typical timing resolution of the ID.

3.4.1 Direct measurement by a laser and a CCD camera

Figure 3.8 shows the setup of the dye laser ball viewed by a CCD camera system. This system is used for the direct measurement of wavelength dependence of the attenuation length. The light emitted from the N_2 pumped dye laser is split into two optical fibers. One is fed into a 2-inch PMT to monitor the intensity of the light(I_{laser}). The other is fed into a diffusion ball and is emitted isotropically. The intensity of the image of the diffusion ball is taken by the CCD camera(I_{CCD}). The relation of I_{CCD} and I_{laser} is expressed as follows:

$$\frac{I_{CCD}}{I_{laser}} = const. \times \exp(\frac{l_d}{L(\lambda)}) \times \frac{1}{l_d^2} \tag{3.1}$$

where λ is a wavelength, $L(\lambda)$ is an attenuation length, and l_d is the distance between the diffusion ball and the CCD.

Figure 3.9 shows the observation of the $\frac{L_{CCD}}{I_{laser}} \times l_d^2$ as a function of I_d for wavelength of 420 nm on Dec 14, 1996. The horizontal axis is the height of the diffusion ball. By fitting the data with a least square method, the attenuation length at 420 ns was estimated to be 92.2 ± 5.2 m.

3.4.2 Indirect measurement by Cosmic ray muon

The attenuation length in water is also measured by the through-going cosmic-ray muons. The energy deposited by the cosmic-ray muon in the detector is almost independent of the muon energy(~2 MeV/cm). Therefore the cosmic-ray muon can be used for a calibration

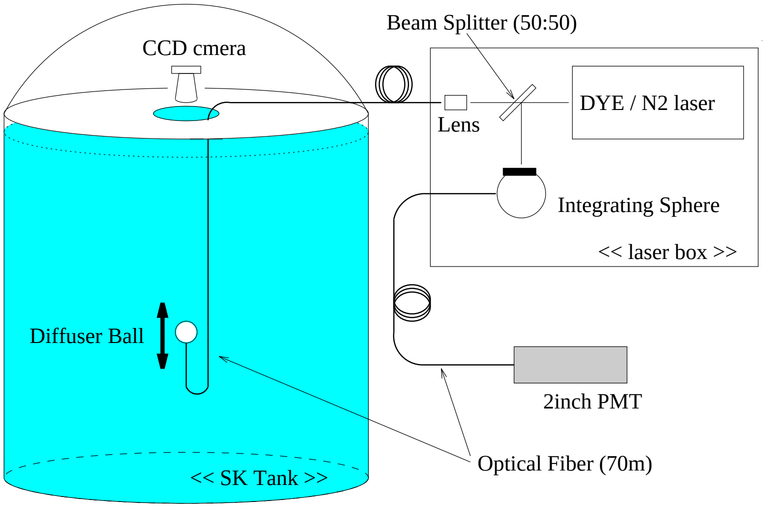

Figure 3.8: The setup of the dye laser + CCD camera system for the measurement of the waver transparency.

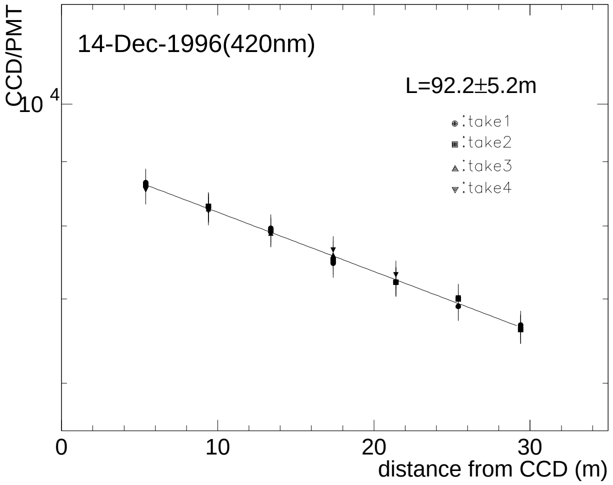

Figure 3.9: The result of a direct measurement of the water attenuation length.

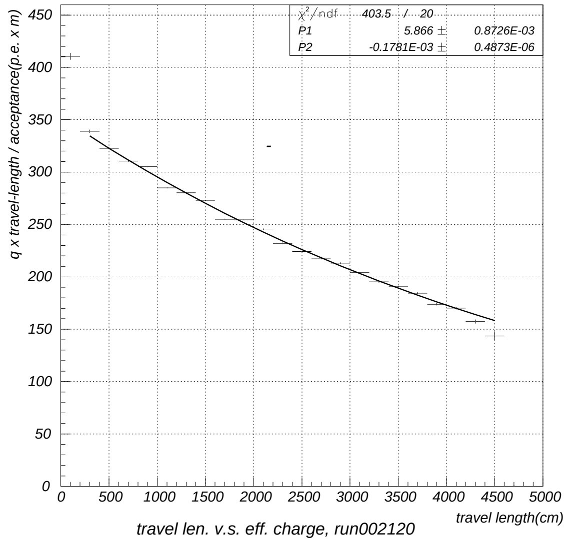

Figure 3.10: $\frac{Q \times l}{f(\theta)}$ distribution from a typical data sample. The solid line shows the fitting result.

source. Comparing with the direct measurement method, cosmic-ray muon method is useful to check a time variation of the attenuation length due to the continuous data taking during a normal run.

The vertical through-going muon events, entering from the top of the detector and exiting to the bottom, are used for the calibration. The muon track is reconstructed by the connecting the entering and exiting points. The observed number of photo-electrons by the i-th PMT, Q$_i$, is expressed as follows:

$$Q_i = const. \times \frac{f(\theta)}{l_i} \exp(-\frac{l_i}{L}) \tag{3.2}$$

where l_i is the light path length and L is the attenuation length of the Cherenkov light. Figure 3.10 shows $\frac{Q_i \times l}{f(\theta)}$ plot as a function of l in a typical run. Since the attenuation length in water varied with the condition of water purification system, it is calculated for each run to correct for the time variation. Figure 3.11 shows the time variation of the attenuation length obtained by the cosmic-ray muon method.

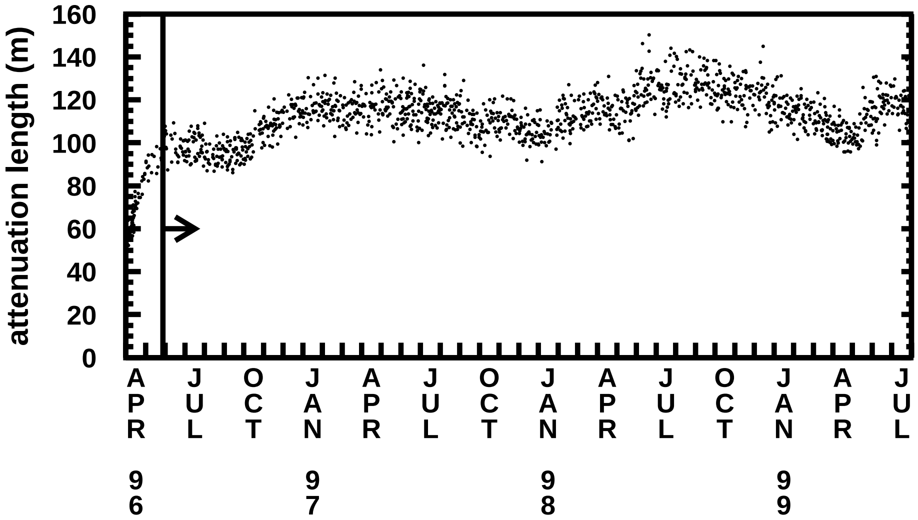

Figure 3.11: The time variation of light attenuation length in water measure by cosmic-ray muons.

Chapter 4

Event Selection

The HE trigger rate for all of Super-Kamiokande data is about 10Hz. About 10^6 events are recorded each day. Typical upward-going muon rate is only a few events per day. Thus the reduction processes are necessary to remove background such as cosmic-ray muons, low energy electrons or noise events.

4.1 Data set

The Super-Kamiokande detector started in April 1996 and finished data taking in July 2001(SK-I). The event selection for upward-going muons needs outer-detector information. Since the outer detector was not stable in the period earlier than May 1996, the data before the period cannot be used for the analysis of upward-going muons. Thus, the data set covers the period from May 1996 to July 2001. The live time for stopping muons and through-going muons are 1646 days described in Section 5.2.

4.2 Reduction process

The reduction flow chart is shown in Figure 4.1. Each process are described as follows. Figure 4.2 shows the trigger rate and event rates. Event rate after the 2nd reduction are stable.

4.2.1 1st reduction

Total Q cut

In the raw data, about 80% are low energy γ-ray from radioactive sources in the water or in the rock outside the detector. In the first reduction step, Events with total photo electron less than 8,000 p.e.s correspond to the track length $\sim$4m are rejected. This

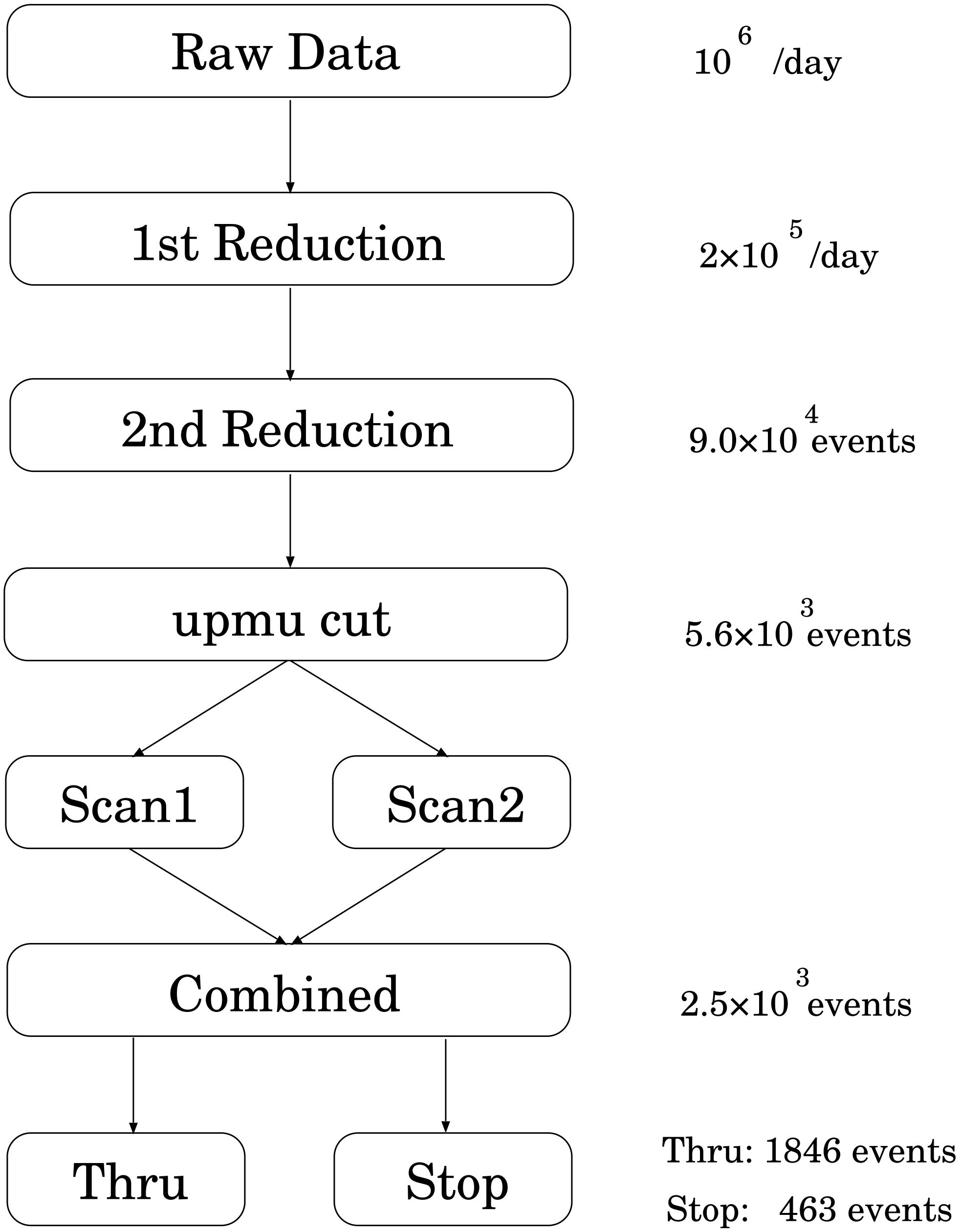

Figure 4.1: The flow chart of event selection.

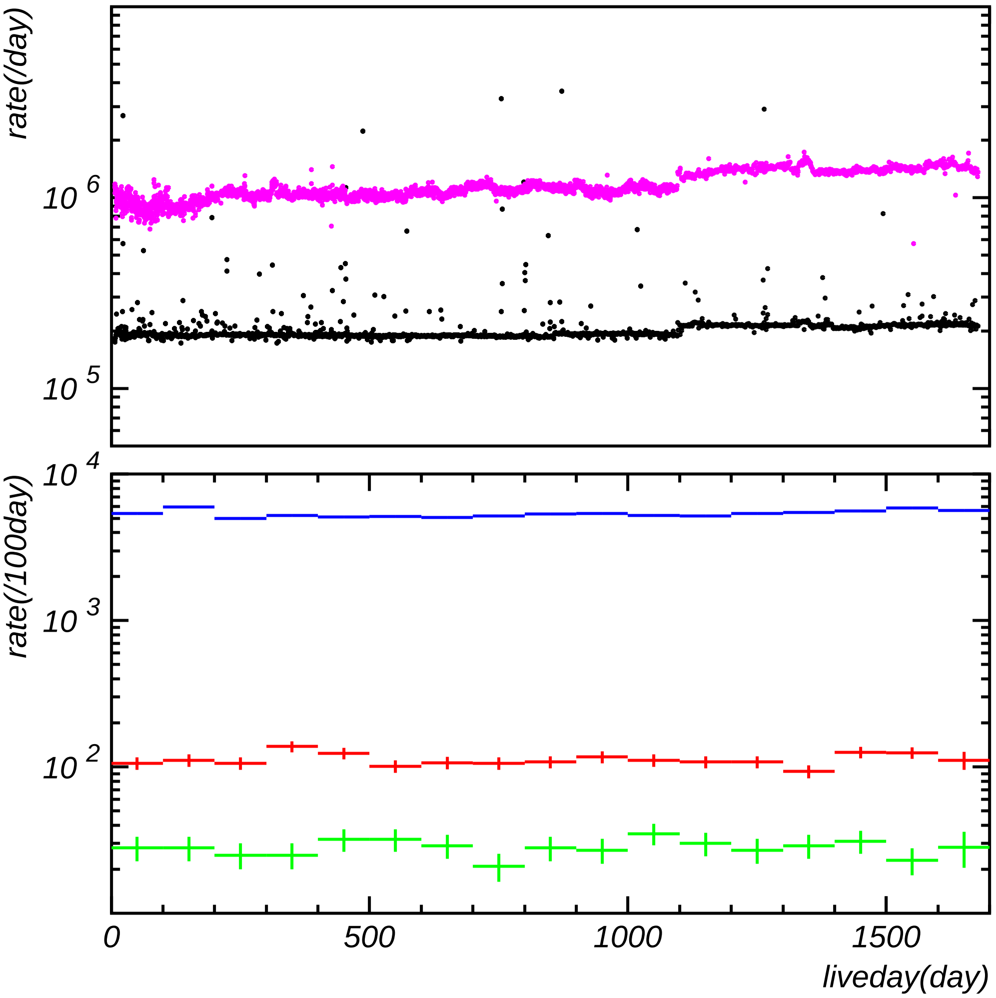

Figure 4.2: The trigger rate and event rates. Upper figure shows the HE trigger rate(pink) and 8000 pe cut rate(black) per day. Lower figure shows the 2nd reduction rate(blue), the upward through-going muon rate(red) and the upward stopping muon rate(green) per 100day.

criterion have an efficient margin. Figure 4.3 shows the total Q distribution for the data and the Monte Carlo.

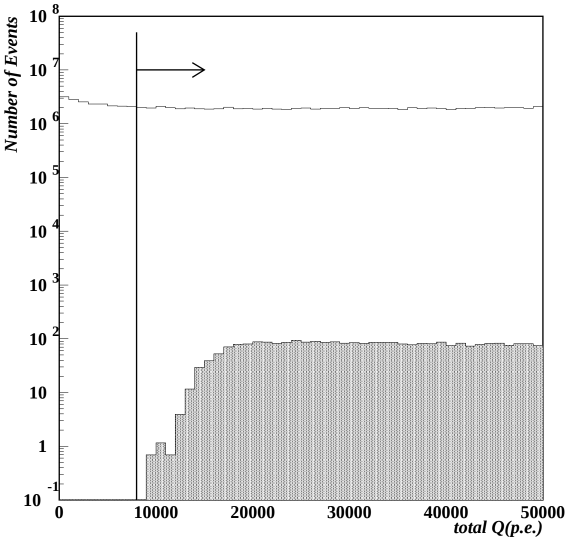

Figure 4.3: The total Q distribution. The histgram shows the data and hatched shows Monte Carlo normalized by the livetime.

Pedestal and OD-off cut

Pedestal events are rejected. If there is no OD hit in an event, this event is rejected.

4.2.2 2nd reduction

Zenith angle cut

To find an entry point initially, the earliest hit timing PMT which has at least three nearest neighbors is searched. If no PMT meets this criterion, the number of neighbors is reduced one until an entry point candidate is found. The fastest entry time(T_0) is just the time of entry point PMT. The exit point is determined to search for the center of the 3×3 PMT clusters which have the highest charge and with its eight surrounding neighbor PMTs. The initial direction is found by drawing a line from the entry point to the exit point.

To determine the direction more precisely, the 'goodness of fit'(GOF) is defined as,

$$GOF = F(f_{cone}) \sum_i g(dt_i), \tag{4.1}$$

where F is a function of the fraction of hits in the Cherenkov cone (f_{cone}), g is a function of the time residual $dt_i = T_{expected} - t_i$, $T_{expected}$ is the calculated time of the expected hit PMT. The function $g(dt_i)$ is determined by timing distributions from the data as,

$$g(dt_i) = \begin{cases} \exp\left(-\frac{(dt_i - t_{mean}(q_i))^2}{2\sigma_1(q_i)^2}\right) & (dt_i < 0 \quad or \quad q_i > 30p.e.s) \\ \exp\left(-\frac{dt_i}{2\sigma_2(q_i)}\right) & (dt_i > 0) \end{cases} \tag{4.2}$$

where σ_1 and σ_2 are timing resolution of the i-th PMT charge.

The direction is searched for to maximize the GOF parameter, by keeping T_0 and the entry point constant. If the event is reconstructed as downward($\cos\Theta$>0.12), the event is rejected.

Edge muon cut

In the downward direction($\cos\Theta$>0.1) events, if the track length which between the entry point and exit point is less than 400 cm, this event is rejected.

Multiple muon cut

Some high energy primary cosmic-ray particles which interact with the atmosphere produce some muons and have almost same direction. Figure 4.4 shows the typical event display of multiple muon. It is assumed that multiple muons have parallel track directions. If the number of the OD clusters are more than three, there is a possibility of multiple muons.

After fitting the first track, a cut which saves only the hits near the track is applied to PMT hits,

$$\vec{n}_{PMT} \cdot \vec{d}_{track} > 0 \tag{4.3}$$

where $\vec{n}_{PMT}$ is the direction of PMT and $\vec{d}_{track}$ is the track direction.

PMTs are further selected to collect the PMTs near the muon tracks. If the light is a plane wave traveling at speed c, 'A plane wave time'(t_{plane}) of the hit PMT is expressed as

$$t_{plane} = T_{entry} + \frac{|(\vec{R}_{PMT} - \vec{R}_{entry}) \cdot \vec{d}_{track}|}{C} \tag{4.4}$$

where $\vec{R}_{PMT}$ is the PMT position vector and $\vec{R}_{entry}$ is the vector to the entry point. If the value t_{plane}-t_i is between -33.3 ns and 16.6 ns the PMT is stored. An event where less than four PMTs left is decided as 1 track event.

Next, other track is searched for. To remove hits closely associated with the first track, PMTs which have 0 ns $<t_{plane}$-$t_i<$ 10 ns and within 12 m of the track are also rejected. It iterates over remaining PMTs as follows,

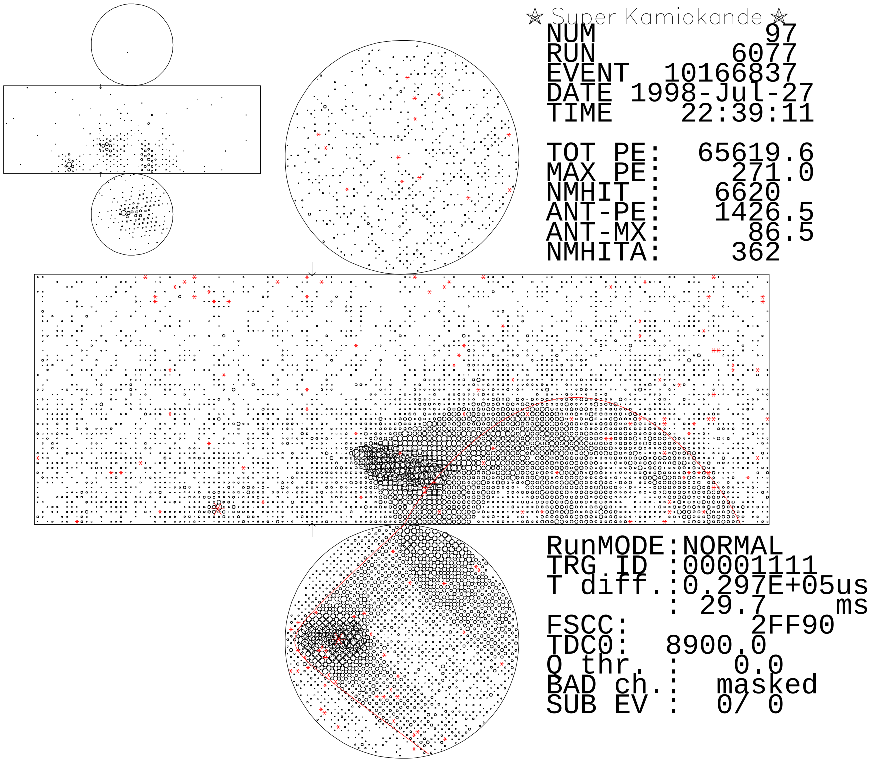

Figure 4.4: The typical event display of multiple muon.

(1) Find the earliest hit. This will be used as T_0 and the entry point.

(2) Cut the PMTs closer than 12m to the track length with $0 < T_{expected}$-$T_i < 10$ ns.

(3) Consider that it is a valid track if the number of PMTs after the cut is more than 5.

(3) If the number of remaining PMTs is more than 6, go back to (1)

After finishing the above steps, this cut is finished as the multiple muon event. If the first track is upward, this event is stored.

Ultra high energy cut

It is difficult to decide the direction of an event when the almost all PMTs of ID has hit signal as shown in Figure 4.5. In this analysis, an event with total photo-electrons grater than 1750kp.e.s is not used.

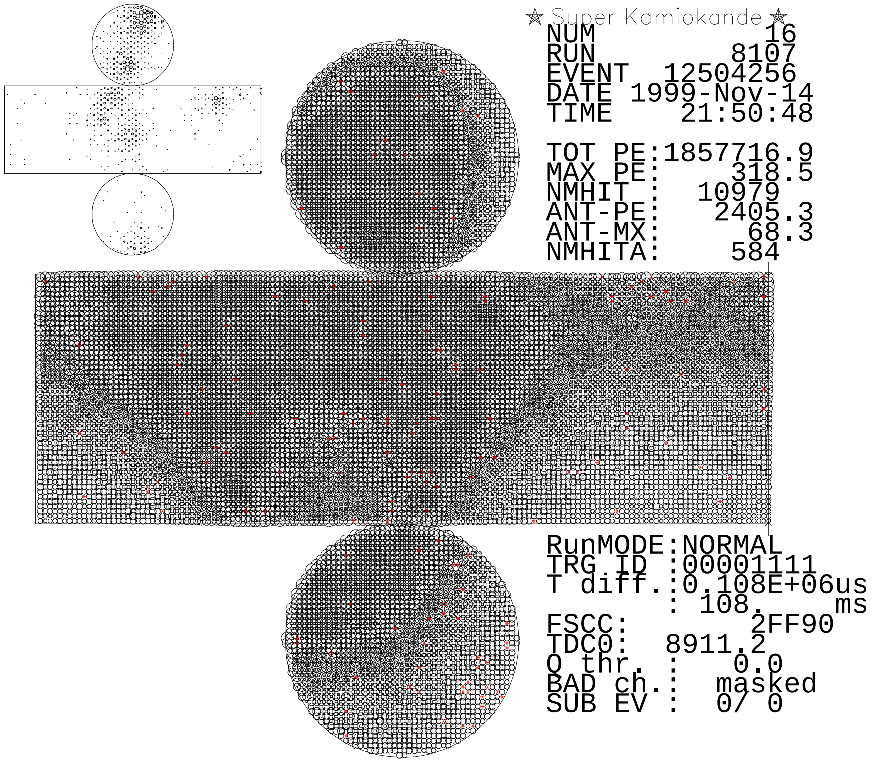

Figure 4.5: The typical event display of ultra high energy.

4.3 Detection efficiency

The detection efficiency for through-going muons and stopping muons are estimated using Monte Carlo events described in Appendix A. The zenith angle distribution of detection efficiency is shown in Figure 4.6.

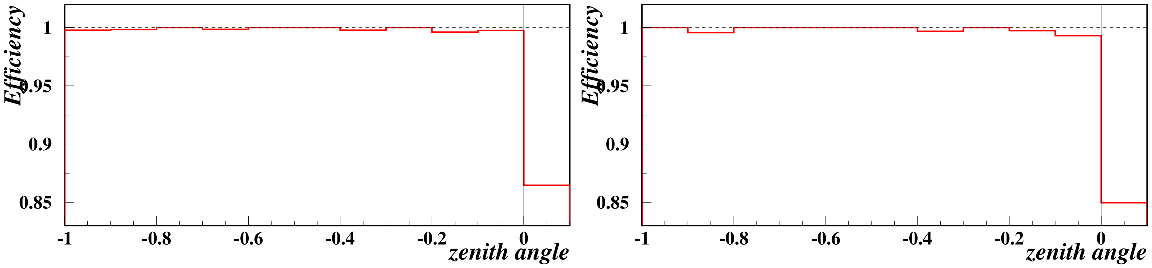

Figure 4.6: Zenith angle distribution of the efficiency for detecting through-going muons(left) and stopping muons(right) by the Monte Carlo simulation.

4.4 Event reconstruction

After the event reduction process, there are about 5 events/day which still include various background events such as cosmic-ray muon events, flashing PMT events and contained events. To decide the direction precisely, events are reconstructed by three fitters: OD-fit, TDC-fit and upmu-fit.

4.4.1 OD-fit

OD-fit by using the information of OD PMTs have the advantage of less miss fitting than the other fitters using the information of ID PMTs, especially for the bremsstrahlung event which hit the almost all ID PMTs or cannot make the Cherenkov cone.

The OD-fit are applied when the number of OD cluster which have more than two. Through-going muon events always have two OD clusters.

The entrance point is decided to find the earliest time on the average among clusters. The exit point is determined by the largest cluster of PMTs in a cluster. The resolution of OD-fit is about 3.8 degrees.

4.4.2 TDC-fit

To search for the position, the goodness G_p is defined as

$$G_P = \frac{1}{N_{hit}} \sum_i exp\left(-\frac{(t_i - \langle t \rangle)^2}{2(1.5\sigma)^2}\right) \tag{4.5}$$

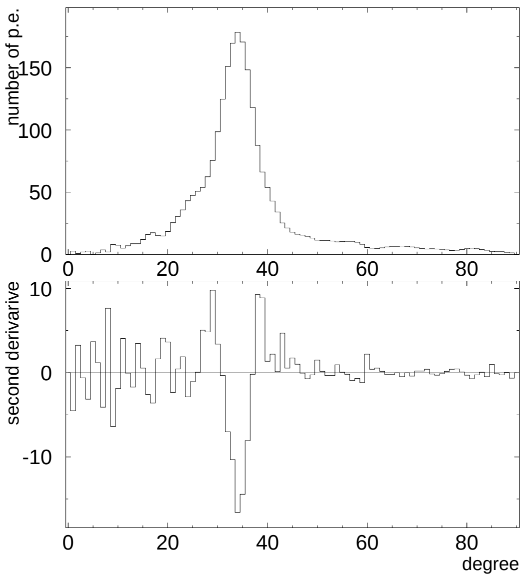

Figure 4.7: The $PE(\theta)$ distributions. Upper figure shows the typical $PE(\theta)$ distribution and lower figure shows the second derivative of $PE(\theta)$. θ_{edge} is larger than the angle at peak position of $PE(\theta)(\theta_{peak})$, and is the angle nearest to θ_{peak} among the angles, which satisfy $\frac{d^2PE}{d\theta^2} = 0$.

where N_{hit} is the number of hit PMTs, σ is the the typical timing resolution of a PMT(2.5 nsec), t_i is the time residual of the i-th PMT, and $\langle t \rangle$ is the mean of t_i. This fitter searches for the vertex position at the maximum G_p value.

In the next step, the direction is decided to find the edge of the Cherenkov cone from the observed charge distribution. For this determination, the function is used as follows,

$$Q = \frac{\int_0^{\theta_{edge}} PE(\theta)d\theta}{\sin\theta_{edge}} \times \left(\frac{dPE(\theta)}{d\theta}\right)^2 \times \exp\left[-\frac{(\theta_{edge}-\theta_C)^2}{\sigma_\theta^2}\right] \tag{4.6}$$

where θ_C is the Cherenkov opening angle, and σ_θ is its resolution. The charge distribution gives the edge as a function of the opening angle of the Cherenkov cone, $PE(\theta)$. Figure 4.7 shows the typical $PE(\theta)$ distribution and its second derivative. The Cherenkov edge θ_{edge} has to be found outside of the cone and also the nearest to the peak, θ_{peak}, of the $PE(\theta)$ distribution at $\frac{d^2PE}{d\theta^2} = 0$. The direction and opening angle of the Cherenkov ring are determined to maximize Q.

In order to determine the vertex position more precisely, the following function of goodness is defined,

$$\begin{cases} G_I = \sum_i \frac{1}{\sigma^2} \exp\left(-\frac{(t_i-\langle t\rangle)^2}{2(1.5\sigma)^2}\right) & \text{inside Cherenkov cone} \\ G_O = \sum_i \frac{1}{\sigma^2} Max\left[\exp\left(-\frac{(t_i-\langle t\rangle)^2}{2(1.5\sigma)^2}\right), 0.8\exp\left(-\frac{t_i-\langle t\rangle}{20nsec}\right)\right] & \text{outside Cherenkov cone} \end{cases} \tag{4.7}$$

$$G = \frac{G_I + G_O}{\sum_i \frac{1}{\sigma^2}} \tag{4.8}$$

The value for goodness falls between 0 and 1, with 1 being the better fit. The TDC-fit finds the vertex which gives the maximum goodness.

4.4.3 Upmu-fit

Upmu-fit is a vertex and direction reconstruction algorithm which is based on most precise fitter for contained events(MS-fit) and which is optimized for upmu events.

For upmu events, upmu-fit are optimized by following,

- The vertex is restricted on the inner surface of the SK tank.
- The type of the particle identification is always muon.
- Single ring is assumed.
- The PMT hit ratio in the opening angle is added to weight to likelihood function.

First, the expected Cherenkov image is calculated from the reconstructed vertex, direction, momentum and opening angle. The expected number of p.e.s in the i-th PMT can be expressed as

$$Q_i^{exp} = \left(\alpha_\mu \frac{sin^2\theta_i}{l_i \left(sin\theta_i + l_i (\frac{d\theta}{dx}) \right)} + Q_i^{knock}(\theta_i) \right) exp(-\frac{l_i}{L}) f(\Theta) + S_i \tag{4.9}$$

where α_μ is the normalization factor, l_i is the distance from the vertex to the i-th PMT, θ_i is the angle of the PMT from the particle direction, L is the attenuation length of light,

$f(\Theta)$ is a function of effective PMT photo-sensitive area, and S_i is the expected amount of scattered light. $Q_i^{knock}(\theta_i)$ is a table of the knock-on electron charge made by Monte Carlo. The terms $sin^2\theta_i$ and $dx \sin\theta + l d\theta$ come from the intensity variation of Cherenkov photons and the change in the photon density due to the change in θ.

The definition of Likelihood for Cherenkov ring pattern is expressed as

$$L = \prod_{\theta_i < (1.5 \times \theta_c)} Prob(Q_i^{exp}, Q_i^{obs}) \tag{4.10}$$

where $Prob$ is the probability to detect Q_i^{obs} in the i-th PMT and Q_i^{exp} is expected. For $Q_{obs} > 20 p.e.$ ($Q_{obs} < 20 p.e.$), the function is estimated based on a single p.e. (Gaussian) distribution,

Another function R_{cone} is defined as follows,

$$R_{cone} = 1 - \frac{N_{hit}^{42}}{N_{all}^{42}} + \frac{N_{hit}^{70}}{N_{all}^{70}} \tag{4.11}$$

where N_{hit}^{42} and N_{all}^{42} are the number of hit PMTs and the number of PMTs in 42 degrees, and N_{hit}^{70} and N_{all}^{70} are the number of hit PMTs and the number of PMTs between 42 and 70 degrees. R_{cone} means the ratio hit PMT numbers. In equation 4.11, the second term $N_{hit}^{42}/N_{all}^{42}$ shows the fill in the Cherenkov ring and third term $N_{hit}^{70}/N_{all}^{70}$ shows the sharpness of the edge of the Cherenkov ring. Therefore if a muon comes in the ID, $N_{hit}^{42}/N_{all}^{42}$ shows a larger value and $N_{hit}^{70}/N_{all}^{70}$ shows a smaller value. Then the smaller R_{cone} means the better muon fitting.

Then the following equation translates the likelihood into a χ^2 parameter,

$$\chi^2 = (-2\log(L) + \text{constant})/R_{cone} \tag{4.12}$$

The upmu-fit finds the vertex where the likelihood becomes a maximum by keeping the opening angle fixed.

4.4.4 Determination of vertex and direction

In the three fitters, OD-fit, TDC-fit and upmu-fit, the most appropriate entrance point and direction is selected. Upmu-fit is basically applied to determine the entrance and direction. However, upmu-fit is very sensitive to the Cherenkov edge. If an event does not have the clear Cherenkov edge in the bremsstrahlung event, the angular resolution of upmu-fit is worse. Thus, the vertex is determined using TDC-fit or OD-fit. If there are more than two clusters in OD, OD-fit can be used.

The detail determination of vertex and direction is described in Appendix B.

4.4.5 Performance

The performance of the fitting is estimated by using the Monte Carlo through-going muons and stopping muons. The upmu Monte Carlo events which is interacted in the rock with atmospheric neutrino are used to check the fitting result.

Figure 4.8 shows the angular resolution Δ(MC,fit) distribution, where Δ(MC,fit) means the difference between the MC thru direction and the fitted direction. The angular resolutions are about 1.0 degree both of through-going muons and stopping muons. Figure 4.9 represents the distribution of the distance between the fitted and the MC true vertex. The entrance resolutions of the through-going muons and stopping muons are about 26 cm and 22 cm, respectively. Figure 4.10 shows resolutions of θ and ϕ direction between the fitted and true direction. these fitting resolutions of the shape of zenith angle are with ±2.6 % which is smaller than the statistical error as shown in Figure 4.11.

4.4.6 Upmu cut

Upward-going muons are obtained after the rejection of the 7m track length cut and $\cos\Theta$ cut.

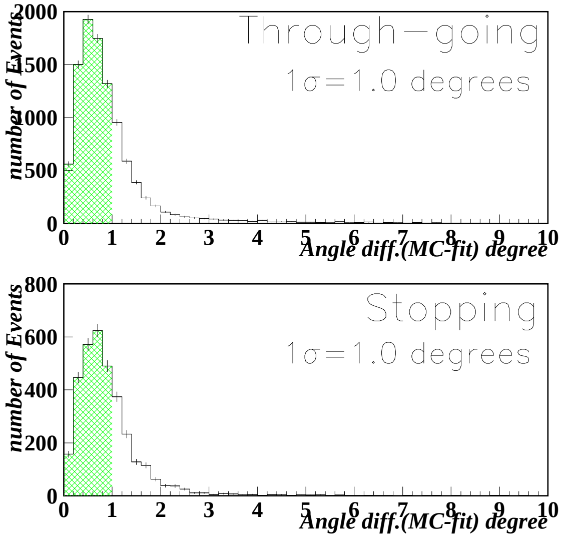

Figure 4.8: The angular resolution of the vertex reconstruction between MC true and MC fit. Upper shows the through-going muons and lower shows the stopping muons. The hatched histograms show the resolution with 1σ corresponding to 68 % of all the events.

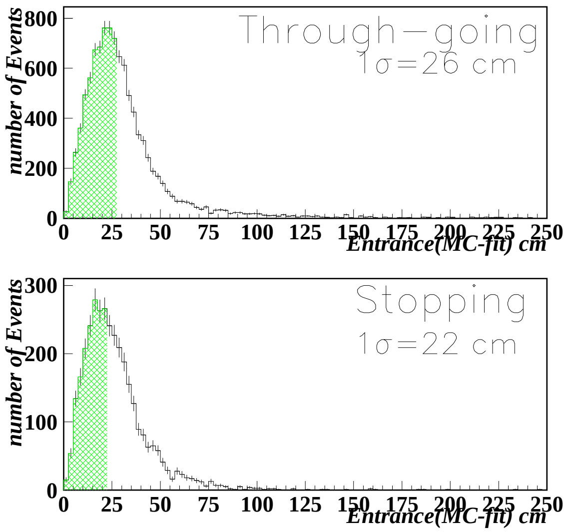

Figure 4.9: The vertex resolution of reconstruction between MC true and MC fitting. upper shows through-going muons and lower shows stopping muons.

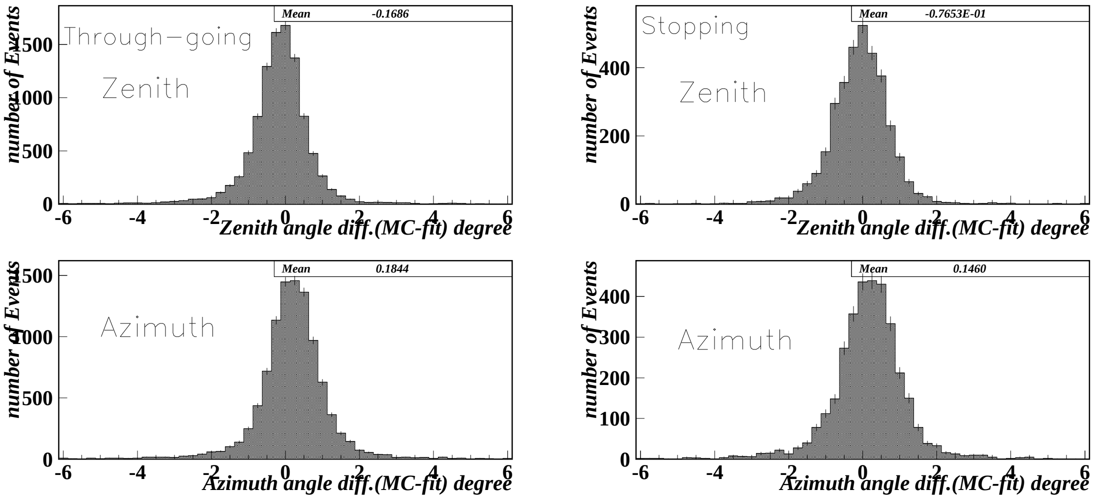

Figure 4.10: The θ and ϕ resolution of vertex reconstruction between MC true and MC fitting. left(right) shows the through-going(stopping) muons, and upper(lower) shows the zenith(azimuth) angle resolution. The hatched histograms show the resolution with 1σ corresponding to 68 % of all the events.

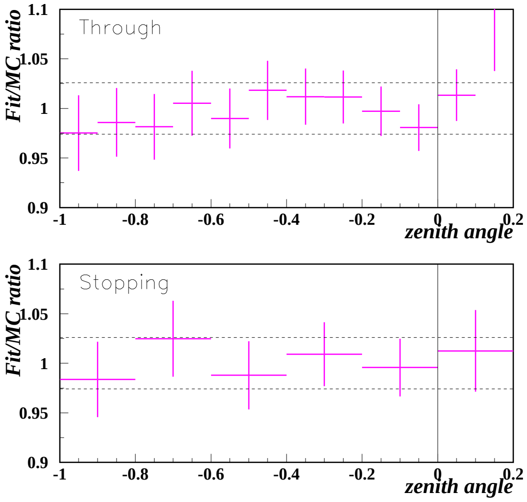

Figure 4.11: The event ratio of fitting events to MC thru events in the zenith angle distribution. Upper shows through-going muons and lower shows stopping muons. The dotted line means the ±2.6 %.

7m track length cut

Since the directional reconstruction is worse for short track and the background other than muons should be taken into account in the low energy region, events with longer than 7m track length (equivalent to 1.6GeV in muon energy) are adopted for final data. The track length means the distance from the entrance to the exit. Because the exit is not exist for the stopping muon, additionally the 7m track length cut for the stopping muon is described in Section 4.7.

$\cos\Theta$ cut

In order to select Upward-going muons, the event whose direction is downward($\cos\Theta \geq 0$) are rejected.

4.5 Scanning

The event rate of upward through-going muons and upward stopping muons after all reductions are 3.3 events per day. But some backgrounds such as miss fitted edge muons, contained and flashing PMT events are still remaining after automatic reductions. To remove them, physicists scan the data with a visual display and can only classify a event of the upward-going muon one by one. The result by auto fitter is never changed for the vertex and direction. Two independent scanners are signed for one data set so as not to miss neutrino events (double scanning). The event rate after scanning is 1.5 events per day.

After the double scanning, the final scanners, who are grouped by two experienced scanners, check the consistency of the classifications by two scanners (final scanning) and make the upward-going muon samples. The possibility that a scanners miss the upward-going events is no more than 0.01. Then the possibility of missing the event by double scanning is $(0.01)^2$. The scanning efficiency is estimated to be almost 100%.

4.6 Stopping/through-going muon separation

The OD entrance point is estimated from ID entrance to back-extrapolate to OD. If the number of PMTs are less than 10 hits in OD entrance within 8 m this events is determined as stopping muon. And if the number of PMTs are more than 10 hits is defined as through-going muon. The misidentification probability of the stopping/through-going muon separation is about 1 %.

4.7 Track length cut for stopping muons

The 7m track length of through-going muons is geometrically determined from the entrance and exit points. However, for stopping muons, track length should be calculated to estimate the stopping point from the energy at the entrance. The entrance point and direction are obtained by the vertex reconstruction. 70^o cone is opened from the entrance point in order to obtain the total charge roughly. The charge of all PMTs inside the 70^o cone is summed as the total charge. After some collections of water transparency and acceptance by PMT geometry, the momentum is estimated from the total charge. Thus the track length is calculated from the momentum by using the muon energy loss of Lohmann's calculation.

4.8 Upward muon events

After all event selection, The final data is selected. Finally, 1846 events and 463 events are obtained as upward through-going muons and upward stopping muons,respectively .

Figure 4.12 shows zenith angle distribution of upward through-going muons and upward stopping muons, and Figure 4.13 shows ϕ distributions.

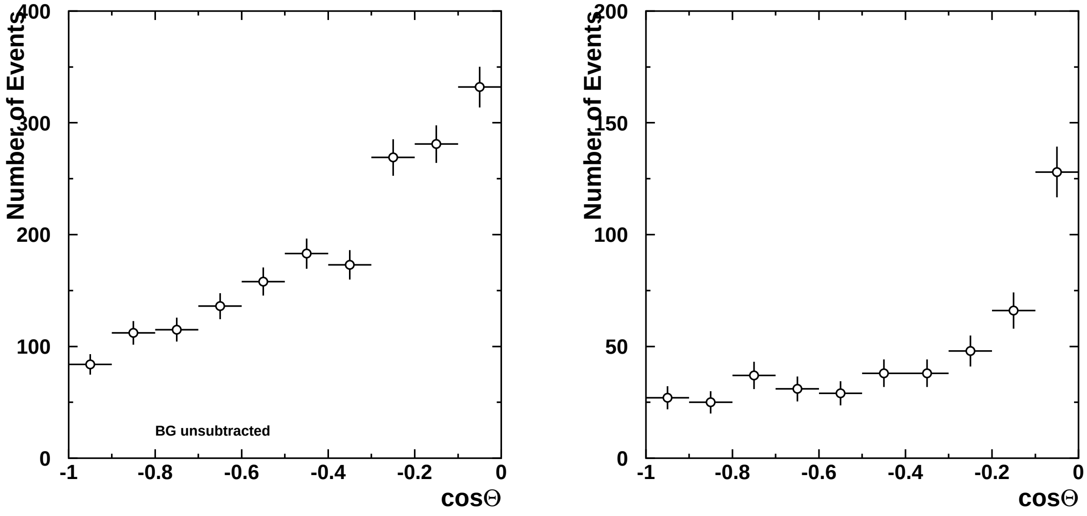

Figure 4.12: Zenith angle number distribution of upward through-going muons(left) and upward stopping muons(right).The horizontal axis is the zenith angle expressed as $\cos\Theta$. The vertical axis is the number of events.

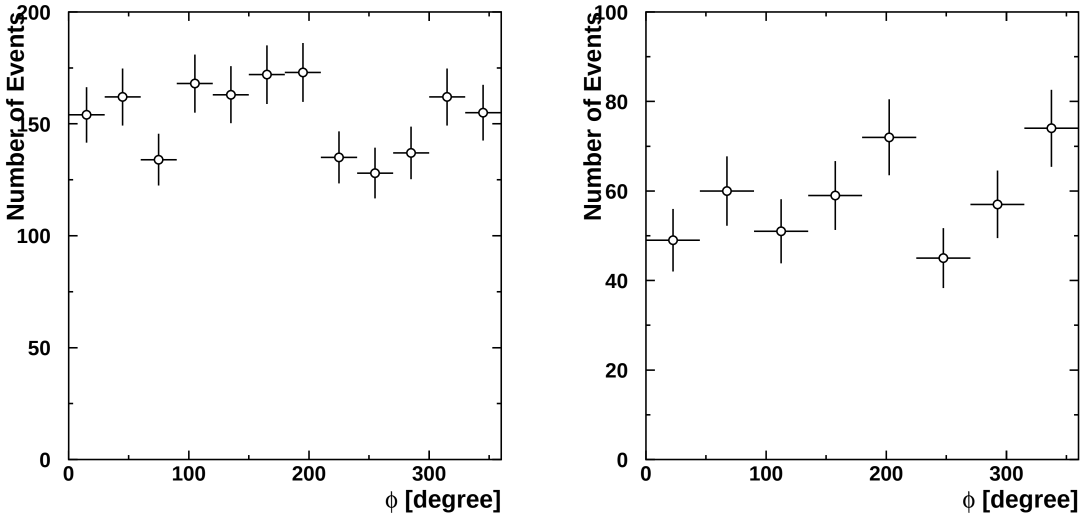

Figure 4.13: ϕ distribution of upward through-going muons(left) and upward stopping muons(right). The horizontal axis is expressed as degrees.

4.9 Backgrounds

4.9.1 Contamination of cosmic-ray muons

The contamination of cosmic-ray muons comes form almost horizontal direction is caused to the multiple scattering or the miss-fitting due to the resolution. The scatter plot of the zenith angle versus azimuth angle distribution of the final data is shown in Figure 4.14. In order to obtain the downward($\cos\Theta \geq 0$) muons, 400 days data are collected by manual reconstruction which means the determination of the entrance and the direction manually by using the event display. In this figure, regions with higher density of points, are seen in the region vertical angle $\cos\Theta < 0$(near horizontal) and azimuth angle at ϕ=120^o, ϕ=180^o for through-going muons and additonally at ϕ=270^o for stopping muons. Since contamination by multiple scattering depends on the amount of rock surrounding the detector and the shape of Ikenoyama mountain, cosmic-ray down-going muons come from relatively thin rock direction. In Figure 4.15, region(2) is thin rock direction. The thin rock region is defined as the region that the zenith angle smaller than $\cos\Theta$=-0.1, and the azimuth angle between 60^o and 240^o(310^o) for through-going(stopping) muons. Region(1) is outside of the region(2).

Figure 4.16 shows the zenith angle distribution for $\cos\Theta$ between -0.1 and 0.08(0.1) for through-going(stopping) muons. Region (1) and (2) are normalized in azimuth angle. Although both distribution is flat in upward region($\cos\Theta<0$), the direction increases exponentially with $\cos\Theta$ in the downward direction in the region(2).

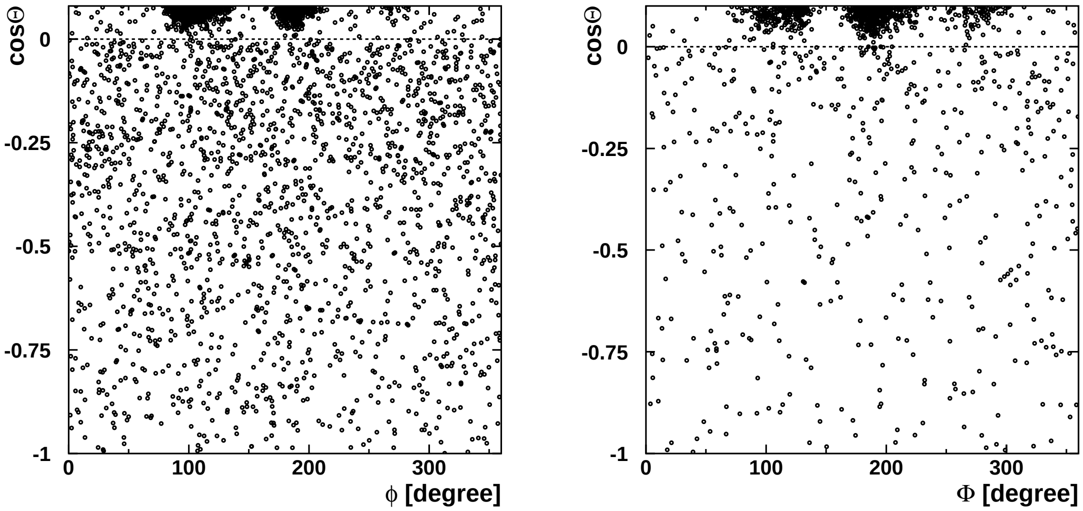

Figure 4.14: Zenith angle and azimuth angle for through-going muons(left) and stopping muons(right). ϕ in horizontal axis means azimuth angle, and $\cos\Theta$ in vertical axis means zenith angle. The downward($\cos\Theta \geq 0$) muons of 400 days data are collected by manual fitting. Cosmic-ray muons are seen in the thin direction ($\phi = 120^o$ and $\phi = 180^o$) of the mountain for downward through going muons, Additionaly cosmic-ray muons are also seen in $\phi = 270^o$ for downward stopping muons.

The number of cosmic-ray contamination into upward region is estimated to extrapolate from the distribution of region(2) as shown in Figure 4.16 to the upward direction. The fitting function integrate the exponential slope in the upward going range is expressed as follows,

$$N_{cont} = \int e^{a+b} d\cos\Theta \tag{4.13}$$

The number of cosmic-ray muons contamination is estimated to be 13.1 ± 1.22 events(-0.1$\leq \cos\Theta <0$) for upward through-going muons, and 30.5 ± 12.5 events(-0.1$\leq \cos\Theta <0$) and 0.3 ± 0.6 events(-0.2$\leq \cos\Theta <$-0.1) for upward stopping muons.

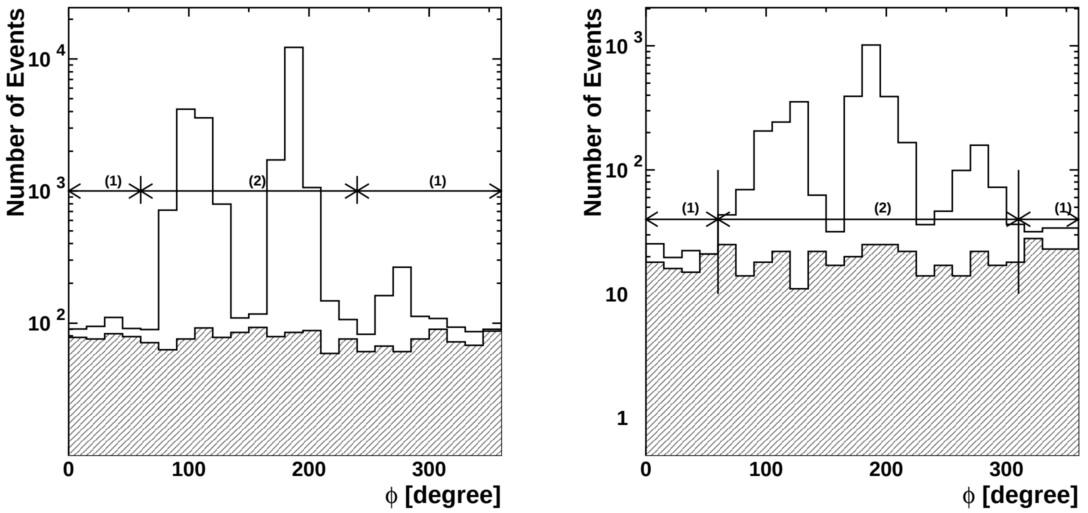

Figure 4.15: The azimuth angle distribution for through-going muons(left) and stopping muons(right). The region(1) is thick rock direction, the region(2) is thin rock direction. Hitsogram shows the distribution of downward muons($0<\cos\Theta<0.1$), and shadow histgram shows the distribution of downward muons($\cos\Theta<0$). Three peaks due to the contamination from downward-going cosmic-ray are seen in thin rock region.

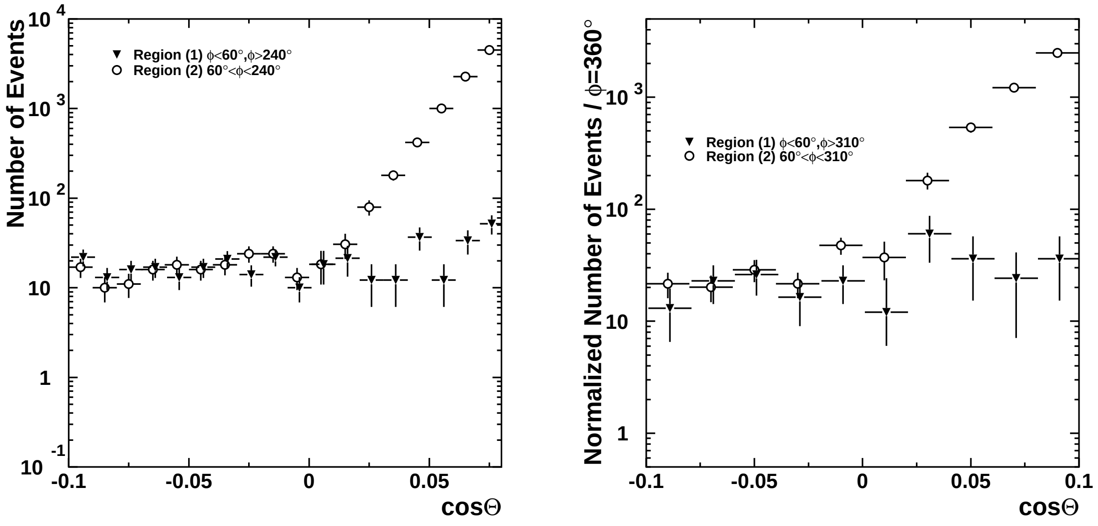

Figure 4.16: The zenith angle distribution of through-going muons and stopping muons near horizontal. The horizontal axis mean the zenith angle($0<\cos\Theta<0.1$). The region(1) is thin rock direction, the region(2) is thick rock direction in azimuth angle. Cosmic-ray contaminations are seen apparently in thin rock region(1).

Chapter 5

Observed flux

5.1 upward-going muon flux

The experimental upward-going muons flux(Φ_{obs}) is calculated by using a live time(T_{live}), an effective area of the detector(S), and a selection efficiency(ϵ). The upward-going muons flux is expressed by the formula,

$$\Phi_{obs} = \frac{1}{2\pi T_{live}} \times \sum_{j}^{N} \frac{1}{\epsilon(\theta_j)S(\theta_j)} \tag{5.1}$$

where θ_j is the zenith angle of the j-th upward going muon event, 2π is the total solid angle covered by the detector for upward-going muons, and N is the total number of observed upward-going muon events. Fluxes of the observed upward stopping muons and through-going muons are estimated from equation 5.1.

5.2 Live time

The detector live time T_{live} is calculated by following equation,

$$T_{live} = T_{run} - T_{inneroff} - T_{outeroff} - T_{pedestal} - T_{dead} \tag{5.2}$$

where $T_{pedestal}$ is the pedestal event time, $T_{inneroff}$ is the ID only dead time, $T_{outeroff}$ is the OD only dead time, T_{dead} is the detector dead and lost data time. The detector dead time means all or a part of event information is lost by electrical or network trouble. The total detector live time is estimated to be 1645 days for upward through-going muons and upward stopping muons.

5.3 Effective area

It is necessary to estimate the incident area of upward muons to a detector in order to calculate flux. The effective area is required to get enough information for upward-going muons which have a given direction, the sensitivity depends on the azimuth angle and the zenith angle of the path of the muons. In this analysis, upward-going muons with the track length longer than 7m are required. The area which have longer than 7m track length in the detector is called the effective area. Since Super-Kamiokande has a cylindrical geometry, the detectable area differs with the angle of an incident muon. Moreover, when an upward-going muon comes into the detector, the region which cannot detect the muon with track length ≥ 7 m exists if the projection depth of the detector cannot be longer than 7m.

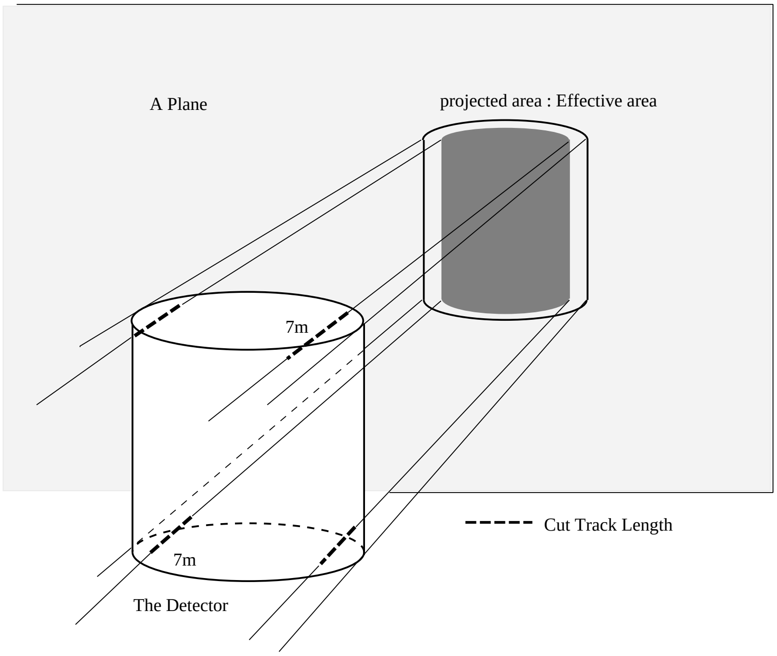

Figure 5.1: Schematic view of effective area.

The effective area is calculated as follows. The schematic view is shown in Figure 5.1. A large plane enough to be projected is taken near the detector. Two-dimensional grid points with every 10 cm step are plotted. A vertical line on the defined plane is drawn from each grid point to the detector. If the length of the line crossing the detector is longer than 7m, the corresponding grid point is counted for a part of the effective area. Finally, the effective area is calculated for every zenith angle of the area divided into 100 directions. The result of the effective area calculation is shown in Figure 5.2.

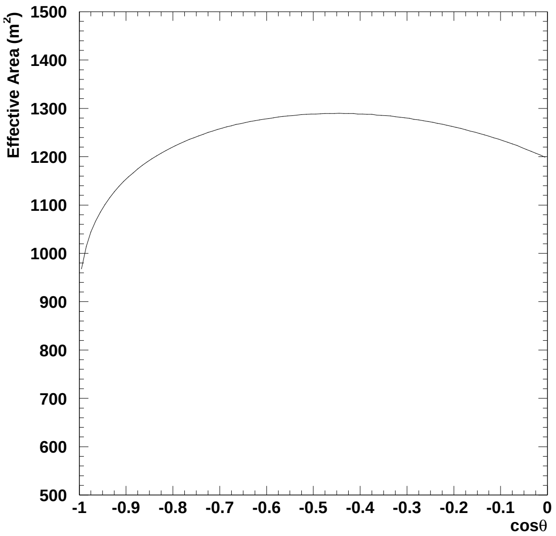

Figure 5.2: The zenith angle dependence of the effective area for upward through-going muons with track length longer than 7m.

5.4 Selection efficiency

The selection efficiency is the detection probability for the upward-going muons estimated for each zenith angle bin, with the range -1$\leq \cos\Theta \leq$0 being divided into 10 bins. The selection efficiency depends on all reduction efficiency because the selection efficiency for bouble scanning is almost 100 % as described in Section 4.5. The result for selection efficiency is shown in Figure 4.6.

5.5 Systematic errors

The systematic errors are categorized into two cases: one is the live time and the effective area which correspond on the event category, and the other is the track length which correspond to independent errors. The uncertainty for the cosmic-ray contamination, which was estimated from down-going muons described in Section 4.9.1, is included in the statistical error.

5.5.1 Track length

For the stopping muons, the difference between the track length reconstructed from total charge of cosmic-ray stopping muons and that calculated from entering point to stopping point with MC is 5%. When the track length cut with 7m is changed ±5%, the upward stopping muon flux is changed +4.9% -4.1%. The systematic error of track length for upward through-going muons is determined to be 0.5% by geometrical uncertainty for the Super-Kamiokande detector.

5.5.2 Systematic errors for observed flux

Table 5.1 and 5.2 shows the summary of systematic errors for the observed upward through-going muon flux and the upward stopping muon flux. Total systematic errors for the observed upward-going muon flux and the through-going muon flux are estimated to be +5.0% -4.2%, and ±1.2%, respectively.

Table 5.3 shows the summary of systematic errors for the ratio of observed upward stopping and through-going muon flux.

source	syst. error of flux
7m track length cut	±0.5%
effective area	±0.3%
Live time	±0.1%
total	± 0.6%

Table 5.1: The summary of systematic error for the upward through-going muons

source	syst. error of flux
7m track length cut	+4.9% -4.1%
live time	±0.1%
total	+5.0% -4.2%

Table 5.2: The summary of systematic error for the upward stopping muons

5.6 Summary of observed upward-going muon flux

In the 1645 live days for upward through-going muons and upward stopping muons, observed fluxes are calculated to be

$$\begin{aligned}\phi_{thru} &= 1.71 \pm 0.04(stat.) \pm 0.02(syst.) \times 10^{-13}(cm^{-2}s^{-1}sr^{-1}) \\ \phi_{stop} &= 0.42 \pm 0.02(stat.) \pm 0.02(syst.) \times 10^{-13}(cm^{-2}s^{-1}sr^{-1}).\end{aligned}$$

source	syst. error of flux
7m track length cut	±4.9%
live time	±0.1%
stop/thru miss ID	±1.0%
total	±5.1%

Table 5.3: The summary of systematic error of the ratio for upward stopping/through-going muons

Zenith angle distributions of upward through-going muon flux and upward stopping muon flux are shown in Figure 5.3.

The total upward going muon flux which is the sum of the stopping muon flux and through-going muons flux is

$$\phi_{thru+stop} = 2.13 \pm 0.05(stat.) \pm 0.03(syst.) \times 10^{-13}(cm^{-2}s^{-1}sr^{-1}),$$

which is independent of the detector shape. The zenith angle distribution of the total upward going muon flux is shown in Figure 5.4.

The ratio for the stopping muon flux and the through-going muon flux is

$$\phi_{stop}/\phi_{thru} = 0.245 \pm 0.014(stat.) \pm 0.013(syst.).$$

The zenith angle distribution of ratio for stopping muon flux and through-going are shown in Figure 5.5.

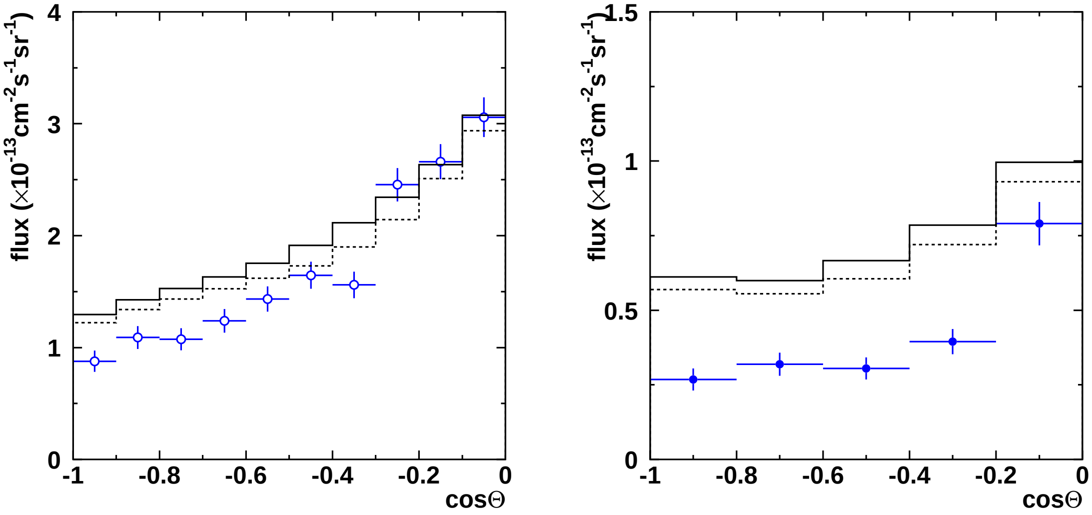

Figure 5.3: The zenith angle distribution of upward through-going muon flux(left) and upward stopping muon flux(right)($E_\mu \geq$1.6GeV). The circles show the observed flux. solided line and dashed line shows the expected flux by Bartol and by Honda, respectively.

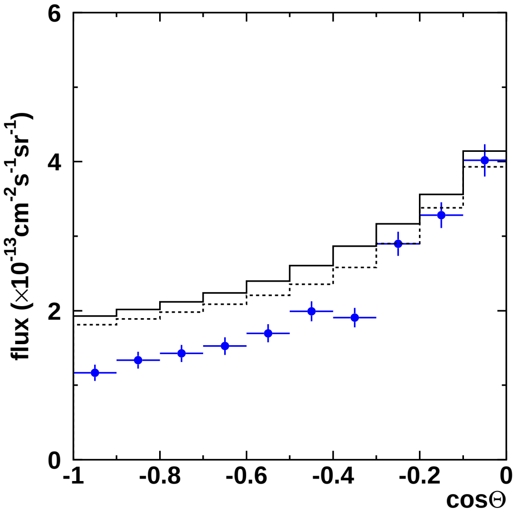

Figure 5.4: The zenith angle distribution of the total upward going muon flux ($E_\mu \geq$1.6GeV). The circles show the observed flux. The solid line and the dashed line shows the expected flux by Bartol and by Honda, respectively.

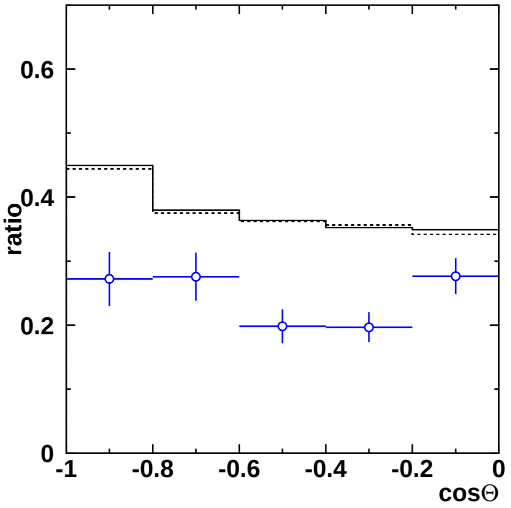

Figure 5.5: The zenith angle distribution of ratio for stopping muon flux and through-going muon flux ($E_\mu \geq$1.6GeV). The circles show the observed flux. The solid line and the dashed line show expected fluxes by Bartol and by Honda, respectively.

Chapter 6

Expected flux

6.1 Analytical Method

Primary cosmic-rays interact with the nucleus of the earth's atmosphere and some kinds of mesons are generated. Neutrinos are produced from the decay of pions an kaons which are produced from those interactions. The atmospheric neutrino penetrates the earth and interact with the nucleus of the rock surrounding the detector. Such neutrino-induced muons generated from the interaction travel through the rock and comes into the detector. The atmospheric neutrino-induced upward-going muon flux is calculated by using the atmospheric neutrino flux(ϕ_ν), the charged current cross section for the neutrino-nucleon interaction in the rock(σ_ν) and the muon range in the rock(R). The production cross section of the neutrino-induced muon produced by the parent atmospheric neutrino in the energy of E_ν is given by

$$\frac{d^2\sigma_\nu}{dxdy} \cdot \frac{d^2\phi_\nu(E_\nu, \cos\Theta_\nu)}{dE_\nu d\Omega}$$

where $d^2\sigma_\nu/dxdy$ is the differential charged current cross section as a function of the Bjorken scaling parameters, x and y (to be described in Section 6.3.1). $d^2\phi_\nu/dE_\nu d\Omega$ is the differential spectrum of the parent neutrino as a function of the neutrino energy (E_ν) and the zenith angle ($\cos\Theta_\nu$).

The probability that a muon with the energy of E_μ survives with the energy larger than E_{th} comes into the detector after the traveling the thickness $X(g/cm^3)$ in the rock is defined as $g(X, E_\mu, E_{th})$. The upward-going muon flux is calculated as follows,

$$\frac{d\phi_\mu(E_{th}, \cos\Theta_\mu)}{d\Omega} = \int_0^\infty N_A dX \int_{E_\mu}^\infty dE_\nu \int_0^1 dy \int_0^1 dx \cdot \frac{d^2\sigma_\nu}{dxdy} \cdot \frac{d^2\phi_\nu(E_\nu, \cos\Theta_\nu)}{dE_\nu d\Omega} \cdot g(X, E_\mu, E_{th}) \tag{6.1}$$

where Θ_μ and Θ_ν are the zenith angle of a muon and its parent neutrino and N_A is Avogadro's number. Θ_ν and Θ_μ can be taken to be Θ so that the direction of the muon is nearly equal to that of its parent neutrino.

The function $g(X, E_\mu, E_{th})$ can be written as

$$g\left(X, E_\mu, E_{th}\right) = \vartheta(R(E_\mu, E_{th}) - X) \tag{6.2}$$

where $R(E_\mu, E_{th})$ is a range that the muon travels while its energy decreases from E_μ to E_{th}, and ϑ is the step function as follows,

$$\vartheta(x) = \begin{cases} 1 & \text{if} \quad x \geq 0 \\ 0 & \text{if} \quad x < 0 \end{cases} \tag{6.3}$$

Equation 6.2 is replaced as follows,

$$\int_0^\infty g(X, E_\mu, E_{th}) dX = R(E_\mu, E_{th}) \tag{6.4}$$

Thus $d\phi_\mu(E_{th}, \cos\theta)/d\Omega$ is expressed as follows,

$$\begin{aligned} \frac{d\phi_\mu(E_{th}, \cos\theta)}{d\Omega} &= N_A \int_{E_\mu}^\infty dE_\nu \int_0^1 dy \int_0^1 dx \cdot \frac{d^2\sigma_\nu}{dxdy} \cdot \frac{d^2\phi_\nu(E_\nu, \cos\theta)}{dE_\nu d\Omega} \cdot R(E_\mu, E_{th}) \qquad (6.5) \\ &= \int_{E_\mu}^\infty \left[\int_0^1 \left[\int_0^1 \frac{d^2\sigma_\nu}{dxdy} dx \right] N_A R(E_\mu, E_{th}) dy \right] \frac{d^2\phi_\nu(E_\nu, \cos\theta)}{dE_\nu d\Omega} dE_\nu \\ &= \int_{E_\mu}^\infty P(E_\nu, E_{th}) \frac{d^2\phi_\nu(E_\nu, \cos\theta)}{dE_\nu d\Omega} dE_\nu \end{aligned}$$

where the function P is defined as

$$P(E_\nu, E_{th}) \equiv \int_0^1 \left[\int_0^1 \frac{d^2\sigma_\nu}{dxdy} dx \right] N_A R(E_\mu, E_{th}) dy \tag{6.6}$$

This function $P(E_\nu, E_{th})$ means the probability that an neutrino with energy E_ν produces a muon by neutrino interaction and the muon reaches the detector with energy larger than E_{th}. Since the Super-Kamiokande detector can not distinguish between the muon from muon a neutrino and from an anti-muon neutrino, the total upward-going muon flux is estimated as follows,

$$\frac{d\phi_\mu(E_{th}, \cos\theta)}{d\Omega} = \int_{E_\mu}^\infty dE_\nu \left[P(E_\nu, E_{th}) \frac{d^2\phi_\nu(E_\nu, \cos\theta)}{dE_\nu d\Omega} + P(E_{\bar\nu}, E_{th}) \frac{d^2\phi_{\bar\nu}(E_\nu, \cos\theta)}{dE_\nu d\Omega} \right] \tag{6.7}$$

6.2 Atmospheric neutrino flux

The energy spectrum of atmospheric neutrino is derived from that of primary cosmic-ray. It has the energy dependency as follows,

$$\frac{d\phi_\nu}{dE_\nu} \propto E_\nu^{-2.7}$$

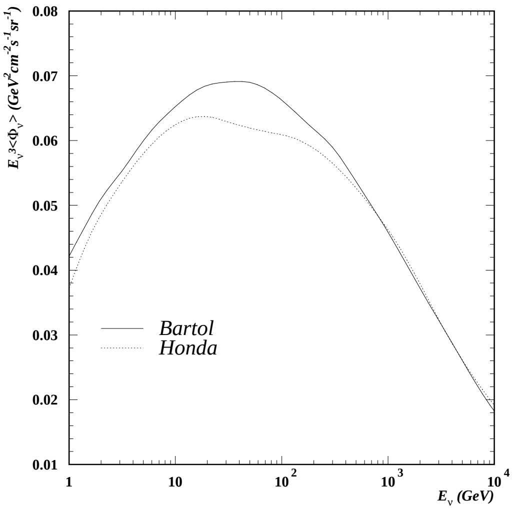

Figure 6.1: The energy spectrum of atmospheric neutrinos($\nu_\mu + \bar{\nu}_\mu$). The average is taken about the zenith angle. The solid line shows the flux of Bartol model, and the dashed line shows the flux of the Honda model. The ordinate is the differential flux multiplied by E_ν^3 in order to clarify the differences.

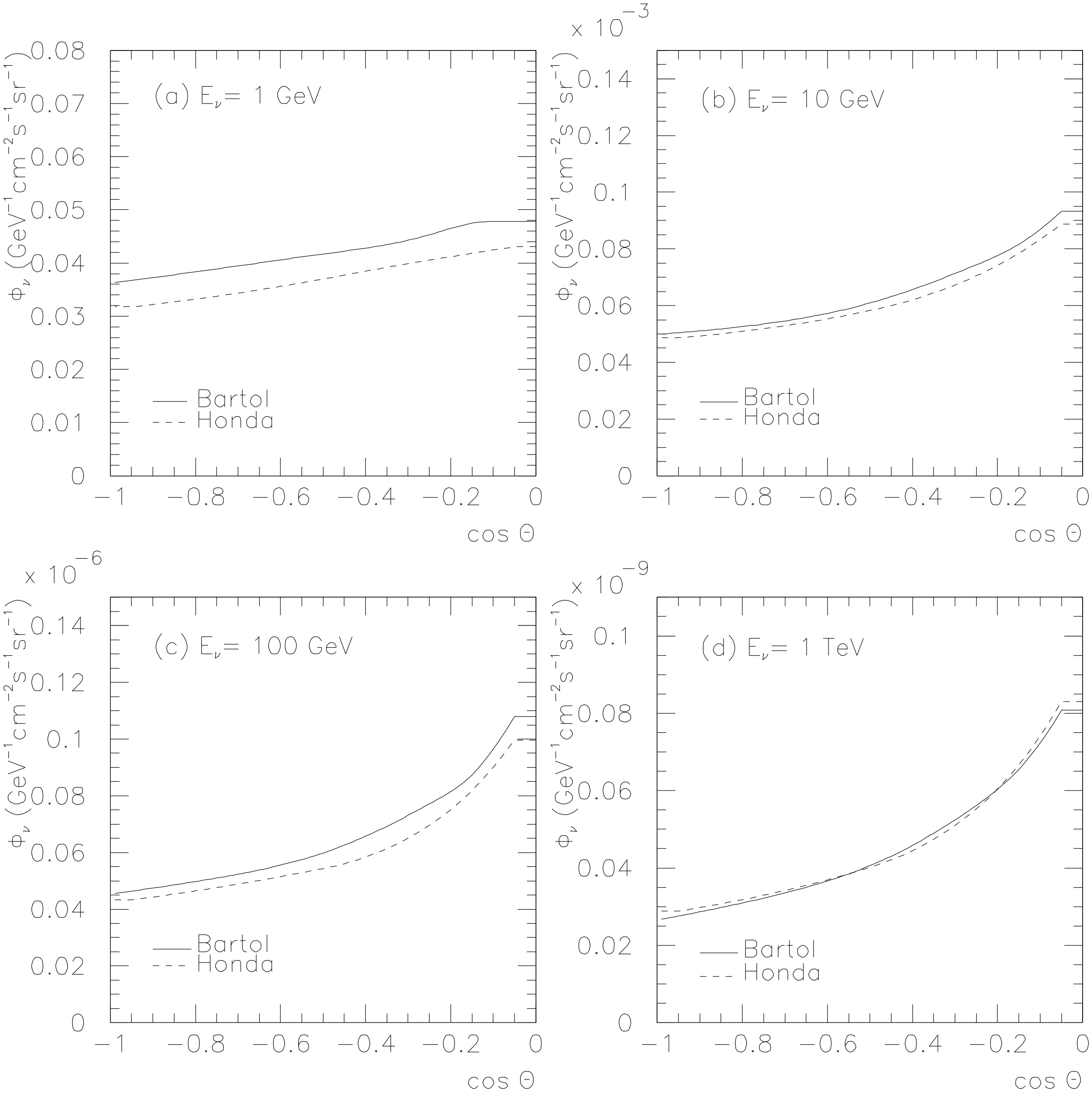

Figure 6.2: The zenith angle distribution of the atmospheric muon neutrinos $(\nu_\mu + \bar{\nu}_\mu)$ at energy (a)1GeV, (b)10GeV, (c)100GeV and (d)1TeV. The solid line shows the flux of Bartol model, and the dashed line shows the flux of the Honda model.

The calculation of atmospheric neutrino flux needs the information about the composition of primary cosmic-ray and hadron interaction. Several models for the atmospheric neutrino flux are available. Energy spectra for atmospheric neutrino fluxes by Bartol[60]、Honda[61] are shown in Figure 6.1.

The upward-going muon flux at vertical upward ($\cos\Theta$=-1) is larger than the flux at horizontal($\cos\Theta$=0). The shape of the zenith angle distribution depends on the neutrino energy. The shape in low energy is flat while it is steep in high energy. Figure 6.2 shows the zenith angle distribution of the atmospheric muon neutrinos($\nu_\mu + \bar{\nu}_\mu$) at energy 1GeV∼1TeV which correspond to the effective region of upward-going muon flux. The angular distributions vary between nadir and the horizon due to the increase in decay length in the horizontal geometry.

6.3 Neutrino-nucleon interaction

The atmospheric neutrino produces a muon when it interacts with nucleon in the rock. Assuming that the neutral current interaction does not influence to the upward-going muon event, the cross section for the charged current interaction is only taken account.

The total cross section for the charged current interaction of neutrinos is consist of deep inelastic scattering(DIS), quasi-elastic scattering(QEL) and single-pion production(1π) .

$$\sigma^{CC} = \sigma^{DIS} + \sigma^{QEL} + \sigma^{1\pi} \tag{6.8}$$

The cross section for DIS is calculated from the parton distribution function(PDF) which expresses the quark distribution in nucleus. The QEL and single pion production are also taken into account.

6.3.1 Deep inelastic scattering

In condition that a neutrino with the energy of E_ν produces the muon with E_μ by the charged current interaction,

$$\frac{d^2\sigma_\nu}{dxdy} = \frac{G_F^2 m_N E_\nu}{\pi} \frac{m_W^4}{(m_W^2+Q^2)^2}\left[y^2 xF_1 + \left(1 - y - \frac{m_N xy}{2E_\nu}\right)F_2 \pm \left(y - \frac{y^2}{2}\right)xF_3\right] \tag{6.9}$$

where x and y are Bjorken scaling parameter, the positive and negative signs in the last term correspond to ν_μ and $\bar{\nu}_\mu$, respectively. G_F is the Fermi constant, m_N and m_W is the mass of the nucleon and the intermediate $W^\pm$ boson, Q^2 is the four momentum transfer squared from neutrino to muon. $F_1(x,Q^2)$,$F_2(x,Q^2)$,$F_3(x,Q^2)$ are the structure functions given by quark momentum distribution functions normalized to one. f_i(i=the flavor of quark) is described as follows, for $\nu_\mu p(n) \to \mu^- X$,

$$\begin{aligned} F_2 &= 2xF_1 = 2x[f_d(f_u) + f_s + f_b + f_{\bar{u}}(f_{\bar{d}}) + f_{\bar{c}} + f_{\bar{t}}] && (6.10) \\ F_3 &= 2[f_d(f_u) + f_s + f_b - f_{\bar{u}}(f_{\bar{d}}) - f_{\bar{c}} - f_{\bar{t}}] && (6.11) \end{aligned}$$

and for $\bar{\nu}_\mu p(n) \to \mu^+ X$,

$$\begin{aligned} F_2 &= 2xF_1 = 2x[f_u(f_d) + f_c + f_t + f_{\bar{d}}(f_{\bar{u}}) + f_{\bar{s}} + f_{\bar{b}}] && (6.12) \\ F_3 &= 2[f_u(f_d) + f_c + f_t - f_{\bar{d}}(f_{\bar{u}}) - f_{\bar{s}} - f_{\bar{b}}] && (6.13) \end{aligned}$$

There are various models with the parton distribution functions which come from the difference of fitting method into the experimental results. In order that the relation between Bjorken scaling parameter x,y and Q^2 is expressed by

$$xy = \frac{Q^2}{2M_N E_\nu}, \tag{6.14}$$

the range of Q^2 is important to integrate over x and y. Especially for low energy neutrinos($E_\nu <$ few GeV), the minimum momentum transfer Q_0^2 is sensitive to the calculation. In this calculation, Q^2 below Q_0^2 is treated as constant value Q_0^2. For the model of PDF, GRV94[62] is taken into account because of using relatively smaller $Q_0^2 (= 0.4 GeV^2)$.

Equation 6.9 can be consistent in both large momentum transfer squared Q^2 and large invariant mass $W^\pm$ of final state hadron system. In the condition that the energy of W is grater than 1.4 GeV, Equation 6.9 is integrated. Figure 6.3 shows the neutrino-nucleon cross section versus neutrino energy.

6.3.2 Quasi-elastic scattering and single pion production

In addition to DIS, Quasi-elastic scattering(QEL) is taken into account. QEL modes consider the charged-current interaction (νN→ νN'). The charged current quasi-elastic scattering cross-section is calculated according to the standard weak interaction formulations as a function of Q^2.

Moreover single pion production is also adopted. A neucleon is excited by the neutrino whose energy is around 1∼2 GeV in resonant states, then de-excited by emitting a meson which are mostly a single pion. The cross sections for single pion production modes are taken from the model of Rein and Seghal [63]. , and are also adopted for the calculations of single η and K production modes.

6.3.3 Total neutrino cross section

The total cross section used in this analysis is shown in Figure 6.4.

6.4 Energy loss for muons

The neutrino-induced muon goes through in the rock with losing their energy. Its travel length in the rock is calculated to judge whether the muon reaches the detector or not.

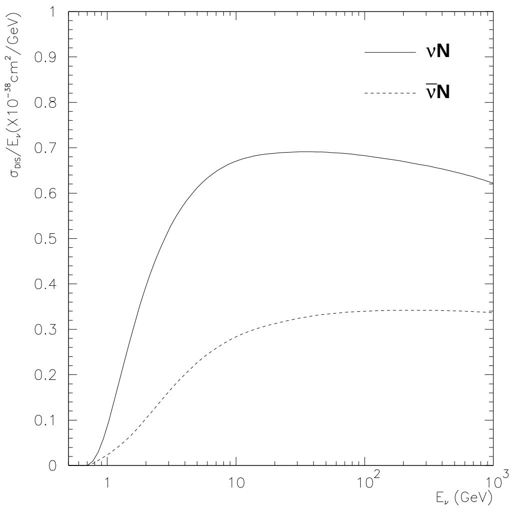

Figure 6.3: The total cross section of DIS in the charged-current interaction in the conditon of $W>$ 1.4 GeV. The solid line shows νN cross section and the dotted line shows $\bar{\nu}$N cross section. GRV94 is used for Q^2 in PDF。

Moreover the muon track length in water is calculated for judgment on muons stopping or going through and on muons traveling over 7 m.

6.4.1 Muon energy loss in rock

The muon energy loss in rock(2.7 g/cm^3 in density) is calculated by Lohmann[64] including contributions from bremsstrahlung, direct pair production and photo-nuclear interactions. Figure 6.5 shows the energy loss(dE/dx) of a muon in standard rock.

The traveling distance for which muons produced in the enerygy E_μ lose energy down to a threshold E_{th} is calculated from following equation,

$$R(E_\mu, E_{th}) = \int_{E_\mu}^{E_{th}} \frac{-dE}{dE/dX} \tag{6.15}$$

The range with E_{th}=1.6GeV is shown in Figure 6.6.

6.4.2 Muon energy loss in water

The muon energy loss in water is calculated by Lohmann for the muon energy larger than 1 GeV. So Lohmann‘s result is applied for energy loss larger than 1 GeV, and

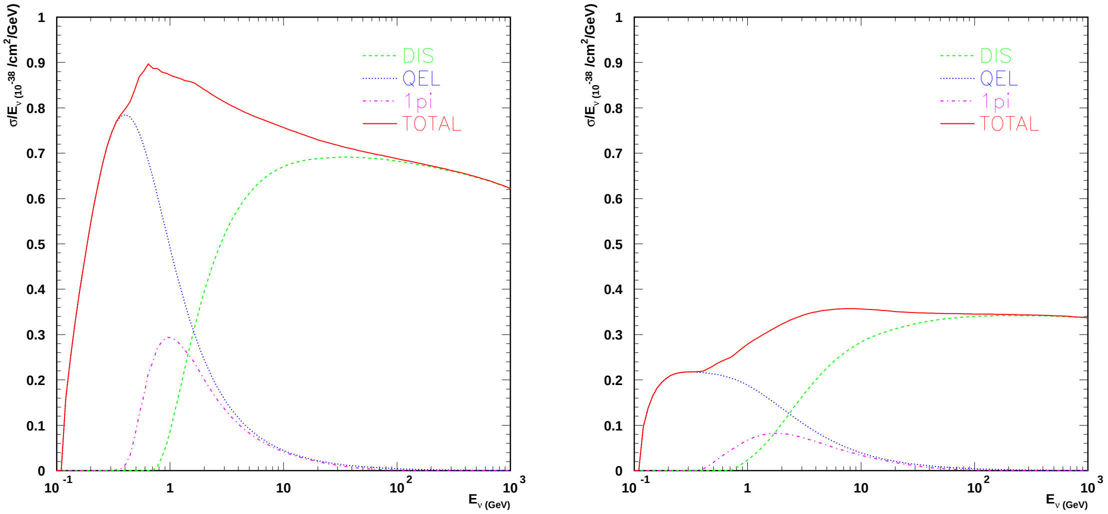

Figure 6.4: The left figure shows the neutrino-nucleon charged-current cross section. and the right figure shows the antineutrino-nucleon charged-current cross section. The dashed line shows the cross section of deep inelastic scattering, dotted line shows one of quasi-elastic scattering, dot-dashed line shows one of single pion production and solid line shows the total cross section.

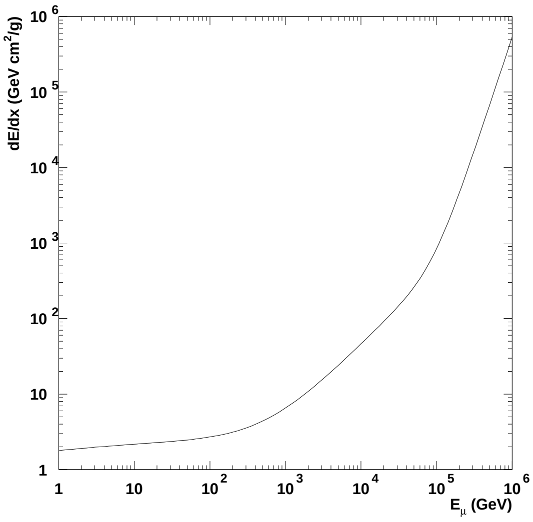

Figure 6.5: The energy loss calculated by Lohmann

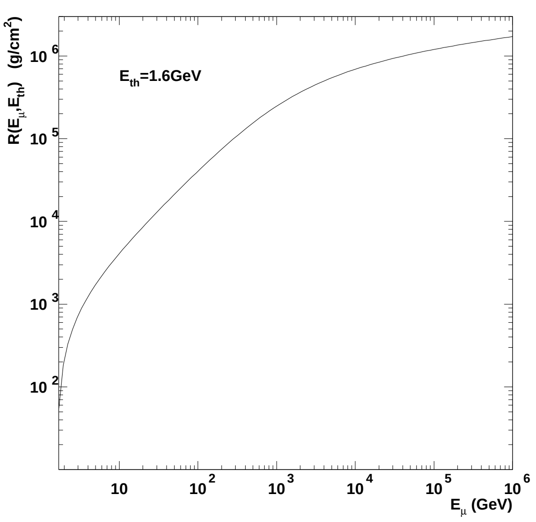

Figure 6.6: the range from E_μ to E_{th} in the standard rock.

the ionization energy loss with dencity effect[65] is applied for smaller than 1 GeV. The muon range in water is shown in Figure 6.7. The 7 m track length corresponds to a muon energy of 1.6 GeV.

6.5 Theoritical uncertainties

The theoretical uncertainties for the expected upward-going muon flux are mainly caused by the uncertainties of atmospheric neutrino flux and neutrino-nucleon interaction.

6.5.1 Atmospheric neutrino flux

Absolute atmospheric neutrino flux

The main source of uncertainty in the calculation of the atmospheric neutrino flux comes from the primary-cosmic ray.

While the primary cosmic-ray flux is well studied at low energy, there is large ambiguity in the determination of absolute value. The result from various measurements covers a range of ±10 % below 100 GeV and ±20 % above. The unceartainty in the calculation of the upward-going muon flux is estimated to be 20 %.

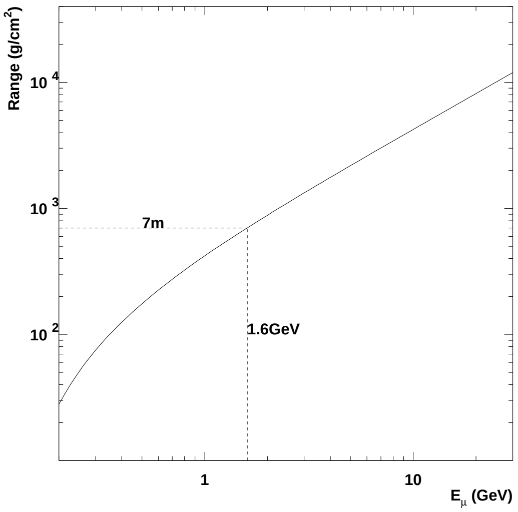

Figure 6.7: the range in the water.

Model dependence of atmospheric neutrino flux

The dependence on neutrino flux models is estimated by comparison between Bartol model[60] and Honda model[61] as shown in Figure 6.8. The uncertainty of absolute flux from the model dependence is estimated to be ~10 %. Moreover the zenith angle bin-by-bin uncertainty, σ^i_{theo}, is also calculated as follows,

$$\sigma^i_{theo} = \frac{\left(\frac{d\Phi}{d\Omega}\right)^i_{Honda} - \left(\frac{d\Phi}{d\Omega}\right)^i_{Bartol}}{\left(\frac{d\Phi}{d\Omega}\right)^i_{Bartol}} \tag{6.16}$$

where $\left(\frac{d\Phi}{d\Omega}\right)^i_{Honda}$ means the flux of Honda model and $\left(\frac{d\Phi}{d\Omega}\right)^i_{Bartol}$ means the flux of Bartol model. These ratios are normalized by the combination of the GRV94 parton distribution function and Bartol neutrino flux model. Figure 6.9 shows the zenith angle distribution as the function of the ratio.

The ratio of the upward stopping muon flux to the upward through-going muon flux

The ratio of upward stopping muon flux to upward through-going muon flux is useful for the analysis. The large uncertainty in the neutrino flux normalization and the neutrino interaction cross section were canceled. because the neutrino flux is approximately

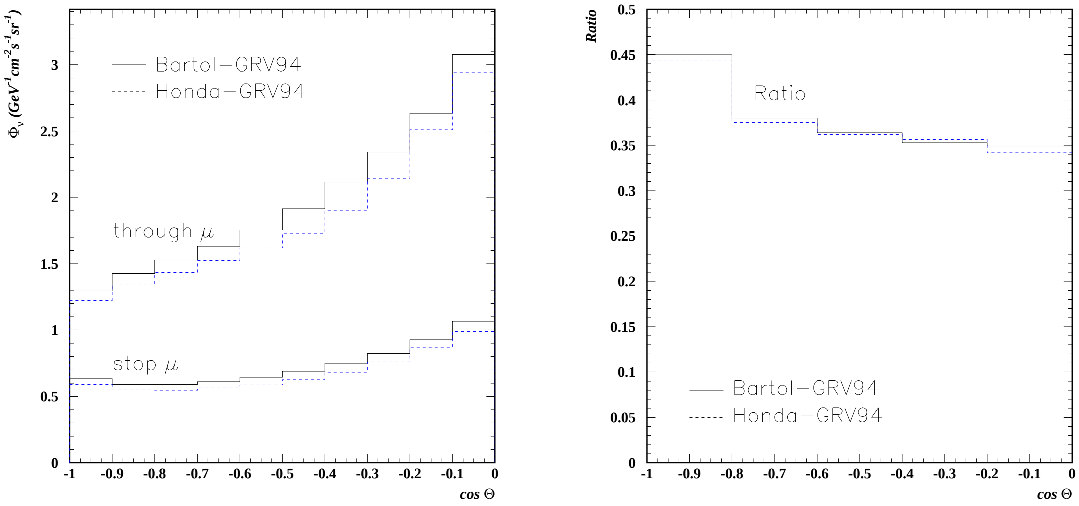

Figure 6.8: The zenith angle distribution of expected flux. Left figure shows the upward through-going muon flux and the upward stopping muon flux. Right figure shows the ratio of the upward stopping muon flux to the upward through-going muon flux. Solid(dashed) line shows Bartol(Honda) model.

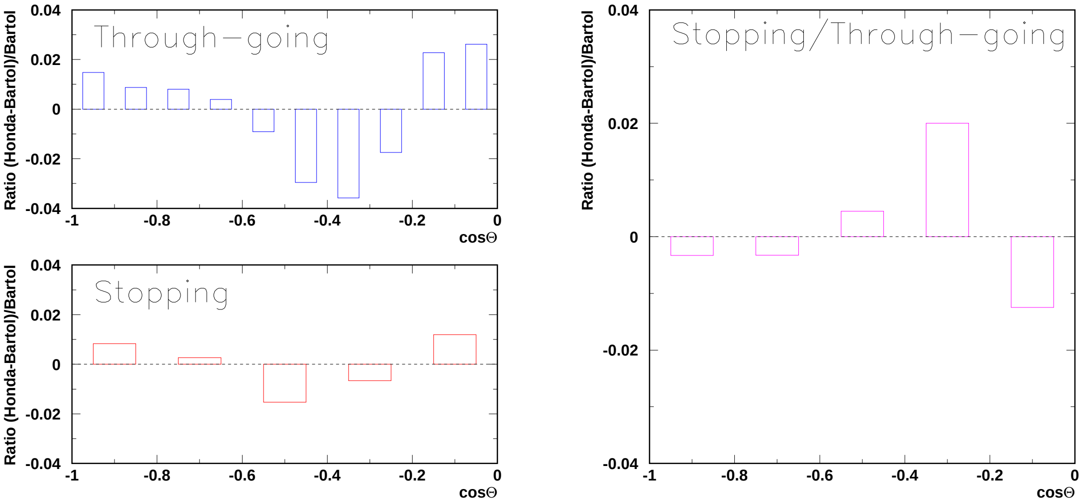

Figure 6.9: The zenith angle distribution as the function of the error estimated from the model difference. Left figure shows the error of the upward through-going muon flux and the upward stopping muon flux. Right figure shows the error of the ratio of the upward stopping muon flux to the upward through-going muon flux. These ratios are normalized by the combination of the GRV94 and Bartol model.

upward stopping muon flux	0.73 ± 0.16(theo.)	($\times\ 10^{-13}\ cm^{-2}s^{-1}sr^{-1}$)
upward through-going muon flux	1.97 ± 0.44(theo.)	($\times\ 10^{-13}\ cm^{-2}s^{-1}sr^{-1}$)
upstop/upthru ratio	$0.372\ ^{+0.049}_{-0.044}$ (theo.)	
total upward-going muon flux	2.70 ± 0.47(theo.)	($\times\ 10^{-13}\ cm^{-2}s^{-1}sr^{-1}$)

Table 6.1: The expected upward-going muon flux and the flux ratio.

defined as (absolute flux)$\times E_\nu^\gamma$ and the cross section of the deep inelastic scattering is canceled.

The uncertainty of atmospheric neutrino flux comes from the primary-cosmic ray energy dependence and affects to upward-going muon flux. To estimate the uncertainty of the upward-going muon flux, the 5 % change of the energy spectral index γ for atmospheric neutrino is applied as follows,

$$\frac{d\phi_\nu}{dE_\nu} \longrightarrow \frac{d\phi_\nu}{dE_\nu} \times E_\nu^{\pm 0.05}$$

The uncertainty of the ratio of the upward stopping muon flux to the upward through-going muon flux come from the uncertainty of the spectrum index is estimated to be +12.5 % -11.4 %.

6.5.2 Neutrino-nucleon cross section

As described in Section 6.2, we consider the uncertainty of the total charged-current cross section. When the cross section is changed with ± 15%, the change of upward-going muon flux is estimated to be +4.2 % -3.5 %.

6.6 Expected flux of upward muons

The upward-going muon flux is calculated by using Bartol's atmospheric neutrino flux and GRV94 neutrino-nucleon neutrino interaction. The energy loss for muons are applied with Lohmann's calculation. The expected upward-going muon fluxes(E_μ>1.6GeV) and the flux ratio are shown as Table 6.1.

Chapter 7

Neutrino oscillation analysis

The theory of neutrino oscillation is described in Section 1.1. The expected flux and observed flux obtained are described in Chapter 6 and Chapter 5, respectively. The upward through-going muons, the upward stopping muons, the ratio of upward stopping muons to upward through-going muons, the upward stopping muons and through-going muons combined are used for neutrino oscillation analysis.

7.1 Absolute flux

The absolute values of the expected and observed upward muon flux are shown in Table 7.1. Comparing to absolute values of the observed flux with of the expected flux in the through-going muons and the stopping muons, there are not significant difference because of the theoretical error of about 22% in the expected flux.

However errors of the neutrino flux and neutrino cross-section uncertainty are canceled by taking a ratio of the stopping muon flux to the through-going muon flux, $\mathcal{R}=\Phi^{stop}/\Phi^{thru}$ where Φ^{stop} and Φ^{thru} are the stopping muon flux and the through-going muon flux, respectively. Consequently the difference of the ratio between the observed value $\mathcal{R}_{obs}$ and the theoretical expected value $\mathcal{R}_{exp}$ comes to 2.6σ. The double ratio of

	Observed flux	Expected flux
Through -going	1.71 ± 0.04(stat.) ± 0.02(syst.) $(\times 10^{-13} cm^{-2} s^{-1} sr^{-1})$	1.97 ± 0.44 (Bartol-GRV94) $(\times 10^{-13} cm^{-2} s^{-1} sr^{-1})$
Stopping	0.42 ± 0.02(stat.) ± 0.02(syst.) $(\times 10^{-13} cm^{-2} s^{-1} sr^{-1})$	0.73 ± 0.16 (Bartol-GRV94) $(\times 10^{-13} cm^{-2} s^{-1} sr^{-1})$
Ratio	0.245 ± 0.014(stat.) ± 0.013(syst.)	$0.372\ ^{+0.049}_{-0.044}$(Bartol-GRV94)

Table 7.1: The summary of the observed flux and the expected flux of upward through-going muons and upward stopping muons.

the observed ratio to the expected ratio is 0.659.

7.2 Neutrino oscillation analysis

7.2.1 Analysis method

The survival probability of muon neutrinos by neutrino oscillation is expressed as equation 1.11. The expected flux is distorted due to the neutrino oscillation.

To compare the observed result with the expected, the χ^2 examination is used to this oscillation analysis. It searches for Δm^2 and $\sin^2 2\theta$ of the best fit point of minimum χ^2 in the various points at oscillation parameters. In this analysis, the upward through-going muon flux, the upward stopping muon flux, the ratio of the stopping muon to through-going muon flux and the combined flux of the upward stopping and through-going muon flux are divided into 10, 5, 5 and 15 zenith angle bin, respectively. The oscillated expected flux is calculated from Equation 1.11. The range of the oscillation parameter to be explored is $0 \leq \sin^2 2\theta \leq 1.4$ and $10^{-4} \leq \Delta m^2 \leq 1$. This region is divided into 1763 points. If the best fit point is the unphysical region($\sin^2 2\theta > 1$), this point is fixed to be $\sin^2 2\theta = 1$.

χ^2 is calculated at each point and the minimum χ^2 is searched. The allowed region is defined by

$$\Delta\chi^2 \equiv \chi^2(\sin^2 2\theta, \Delta m^2) - \chi^2_{min} < \Delta\chi^2_{th} \tag{7.1}$$

where $\Delta\chi^2_{th}$ is set to 2.3, 4.6 and 9.2, correspond to 68%, 90% and 99% of the confidence level, for the degree of freedom=2.

The summary of systematic uncertainties is shown in Table 7.2. The systematic error of normalization factor is estimated as follows,

Absolute normalization factor: α The absolute normalization uncertainty σ_α is estimated to be ±22.4% including theoretical uncertainties and experimental uncertainties. Theoretical uncertainties consist of the absolute neutrino flux and model dependence. Experimental uncertainties consist of the track length cut and livetime.

Stop/thru relative normalization factor: β The stop/thru relative normalization uncertainty σ_β is estimated to be ±14.2% including theoretical uncertainties and experimental uncertainties Theoretical stop/thru uncertainties consists of the primary spectrum index and cross section. Experimental stop/thru uncertainties consists of the track length cut, livetime and stop/thru miss ID.

(a)Theoretical typical uncertainties in flux calculation

absolute neutrino flux	±20.0%
absolute model dependence	±10.0%

(b)Theoretical stopping/through-going uncertainties

primary spectrum index	+12.5% -11.4%
cross section	+4.2% -3.5%
choice of ν flux	±0.9%

(c)Experimental sys. errors in through-going flux

track length cut	±0.5%
live time	±1.0%

(d)Experimental sys. errors in stopping flux

track length cut	+4.9% -4.1%
live time	±1.0%

(e)Experimental stopping/through-going sys. errors

track length cut	±4.9%
live time	±1.0%
stop/thru miss ID	±1.0%

Table 7.2: Uncertainties for oscillation analysis.

Horizontal and vertical ratio: ε The factor of horizontal and vertical ratio σ_ε is taken to be ±3 %. This uncertainty is expressed by multiplying factors $1+2\varepsilon(\cos\Theta_i+\frac{1}{2})$, where Θ_i is a central value of zenith angle for the i-th bin.

The normalization summary for oscillation analysis is shown in Table 7.3.

7.2.2 Analysis for upward through-going muons

The χ^2 definition of the upward through-going muon flux is expressed as follows,

$$\chi^2_{thru} = \sum_{i=1}^{10} \left(\frac{\left(\frac{d\Phi}{d\Omega}\right)^{thru,i}_{obs} - (1+\alpha)\left(1+2\varepsilon(\cos\Theta_i+\frac{1}{2})\right)\left(\frac{d\Phi}{d\Omega}\right)^{thru,i}_{theo}}{\sqrt{(\sigma^{thru,i}_{stat})^2+(\sigma^{thru,i}_{sys})^2}} \right)^2 + \left(\frac{\alpha}{\sigma_\alpha}\right)^2 + \left(\frac{\varepsilon}{\sigma_\varepsilon}\right)^2 \tag{7.2}$$

where $\left(\frac{d\Phi}{d\Omega}\right)^{thru,i}_{obs}$ means the observed muon flux in the i-th $\cos\Theta$, $\left(\frac{d\Phi}{d\Omega}\right)^{thru,i}_{theo}$ means the theoretical muon flux, $\sigma^{thru,i}_{stat}$ means the experimental statistical error, $\sigma^{thru,i}_{sys}$ means the

	Normalization factor		error
α	Absolute normalization	σ_α	$\pm 22.4\%$
β	Stop/thru relative normalization	σ_β	$\pm 14.2\%$
ε	Horizontal and vertical ratio	σ_ε	$\pm 3\%$

Table 7.3: The systematic error of normalization factor for oscillation analysis.

combination of bin-by-bin uncorrelated theoretical as shown in Figure 6.9 and experimental systematic errors as shown in Table 7.2(c), α means the absolute flux normalization factor with error σ_α, ε means the vertical/horizontal correlated normalization factor with error σ_ε.

Figure 7.1 shows the Δm^2-$\sin^2 2\theta$ contour plot of the upward through-going muon flux for ν_μ-ν_τ oscillation. The zenith angle distribution at the best fit is shown in Figure 7.2. The best fit is obtained at Δm^2=3.2×10^{-3}eV^2 and $\sin^2 2\theta$=1.0 at a minimum χ^2 of 9.49/8 when the parameter of α is 0.04 and ε is 0.01. At the best fit including the unphysical region($\sin^2 2\theta>1$), the χ^2 becomes 29.13/8 at $\sin^2 2\theta$=1.24 and Δm^2=2.3×10^{-3}eV^2 with α=0.04 and ε=0.00. Assuming to the null oscillation, the χ^2 is 28.9/10.

7.2.3 Analysis for upward stopping muons

The χ^2 definition of stopping muon flux is almost same as that of through-going muon flux as follows,

$$\chi^2_{stop} = \sum_{i=1}^{5} \left(\frac{\left(\frac{d\Phi}{d\Omega}\right)^{stop,i}_{obs} - (1+\alpha)\left(1+2\varepsilon(\cos\Theta_i + \frac{1}{2})\right)\left(\frac{d\Phi}{d\Omega}\right)^{stop,i}_{theo}}{\sqrt{(\sigma^{stop,i}_{stat})^2 + (\sigma^{stop,i}_{sys})^2}} \right)^2 + \left(\frac{\alpha}{\sigma_\alpha}\right)^2 + \left(\frac{\varepsilon}{\sigma_\varepsilon}\right)^2 \tag{7.3}$$

Figure 7.3 shows the Δm^2-$\sin^2 2\theta$ contour plot of upward stopping muon flux for ν_μ-ν_τ oscillation. The zenith angle distribution at the best fit is shown in Figure 7.4. The best fit is obtained at Δm^2=1.9×10^{-3}eV^2 and $\sin^2 2\theta$=1.0 at a minimum χ^2 of 1.59/8 when the parameter of α is -0.001 and ε is -0.03. At the best fit including the unphysical region, the χ^2 becomes 1.31/3 at $\sin^2 2\theta$=1.15 and Δm^2=2.5×10^{-3}eV^2 with α=0.001 and ε=0.14. Assuming to the null oscillation, the χ^2 is 15.7/5.

7.2.4 Analysis for upward stopping/through-going muons ratio

The χ^2 definition of the ratio of the upward stopping/through-going muon flux is written as follows,

$$\chi^2_{ratio} = \sum_{i=1}^{5} \left(\frac{\mathcal{R}^i_{obs} - (1+\beta)\mathcal{R}^i_{theo}}{\sqrt{(\sigma^i_{\mathcal{R},stat})^2 + (\sigma^i_{\mathcal{R},sys})^2}} \right)^2 + \left(\frac{\beta}{\sigma_\beta}\right)^2 \tag{7.4}$$

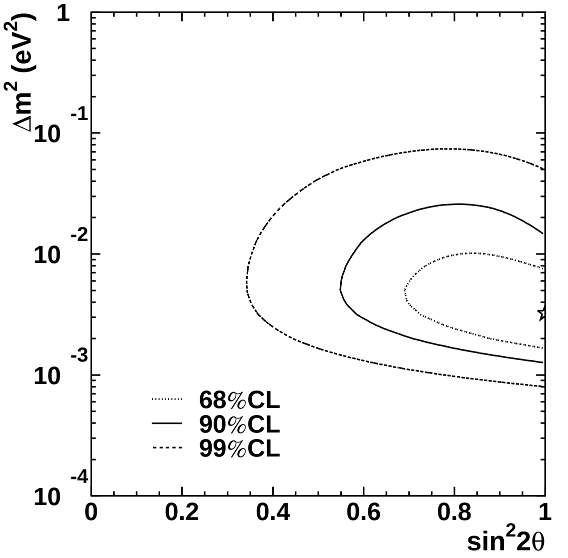

Figure 7.1: The allowed region for ν_μ-ν_τ oscillation of the upward through-going muon flux on Δm^2-$\sin^2 2\theta$. the regions means 68%、90% and 99% confidence level. ‘star‘ means the best fit point as (Δm^2,$\sin^2 2\theta$)=(3.2×10^{-3},1.0).

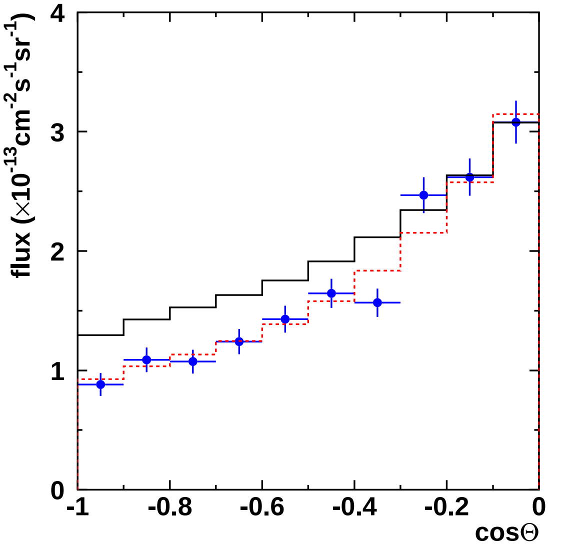

Figure 7.2: The zenith angle distribution of the upward through-going muon flux. The dashed line means the expected flux at the best fit parameter (α=0.04,ε=0.01).

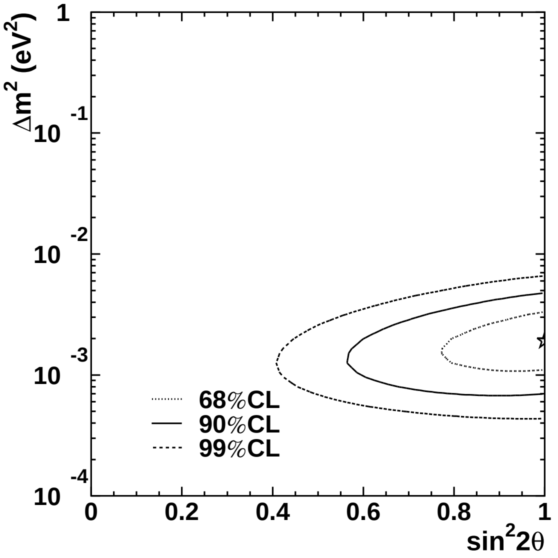

Figure 7.3: The allowed region for ν_μ-ν_τ oscillation of the upward stopping muon flux on Δm^2-$\sin^2 2\theta$. the regions means 68%、90% and 99% confidence level. ‘star‘ means the best fit point as $(\Delta m^2, \sin^2 2\theta) = (1.9\times10^{-3}, 1.0)$.

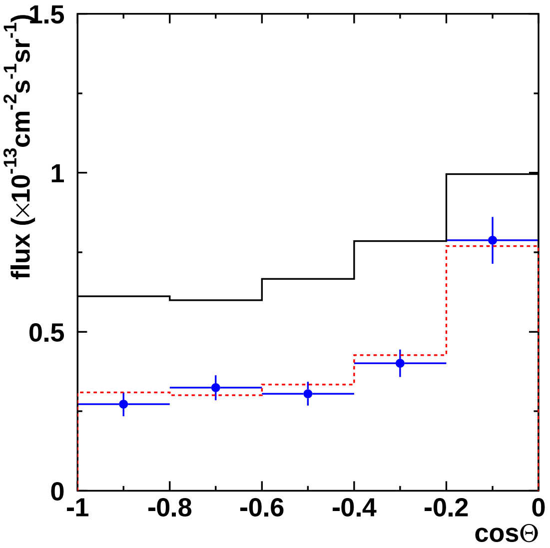

Figure 7.4: The zenith angle distribution of the upward stopping muon flux. The dashed line means the expected flux at the best fit parameter (α=0.001,ε=0.03).

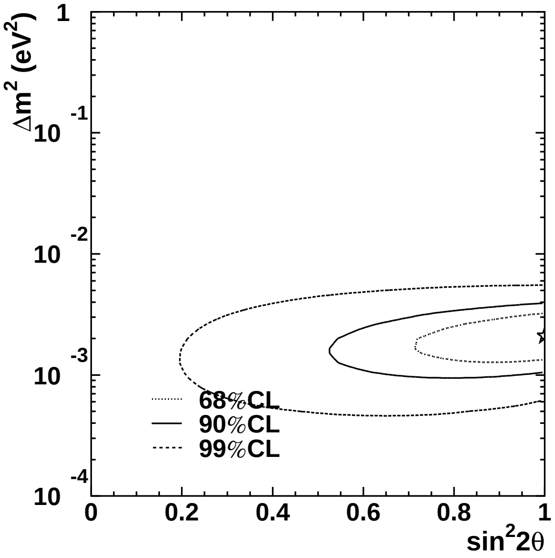

Figure 7.5: The allowed region for ν_μ-ν_τ oscillation of the ratio of upward stopping muon flux to upward through-going muon flux on Δm^2-$\sin^2 2\theta$. the regions means 68%、 90% and 99% confidence level. ‘star‘ means the best fit point as (Δm^2,$\sin^2 2\theta$)=(2.1×10^{-3},1.0).

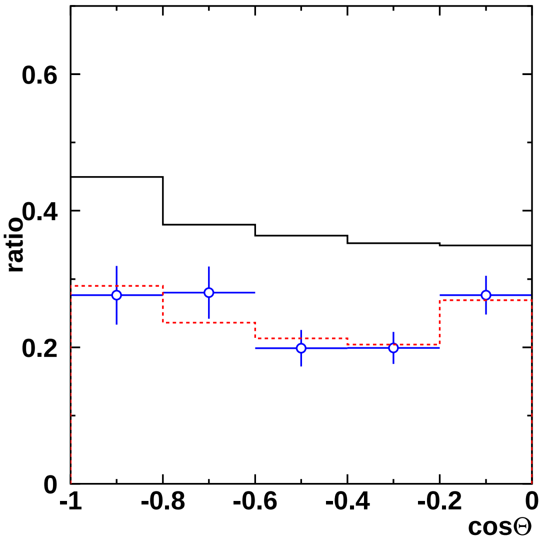

Figure 7.6: The zenith angle distribution of the ratio of upward stopping muon flux to upward through-going muon flux. The dashed line means the expected flux at the best fit parameter (β=-0.02).

where $\mathcal{R}^i_{obs}$ and $\mathcal{R}^i_{exp}$ mean the observed flux ratio and the theoretical muon flux ratio in the i-th $\cos\Theta$, and β mean the relative normalization factor for the ratio of stopping muon flux to through-going flux with error σ_β. $\sigma^i_{\mathcal{R},sys}$ means the experimental statistical error, and $\sigma^i_{\mathcal{R},sys}$ means the combination of bin-by-bin uncorrelated theoretical as shown in Figure 6.9 and experimental systematic errors as shown in Table 7.2(e). The absolute flux normalization factor and vertical and horizontal normalization factor are almost canceled. Thus β is only used.

The Δm^2-$\sin^2 2\theta$ contour plot and the zenith angle distribution of the ratio are shown in Figure 7.5 and Figure 7.6. The best fit is obtained at Δm^2=2.1×10^{-3}eV^2 and $\sin^2 2\theta$=1.0 at a minimum χ^2 of 1.75/3 when the parameter of β is -0.02. At the best fit including the unphysical region, the χ^2 becomes 1.63/3 at $\sin^2 2\theta$=1.04 and Δm^2=2.5×10^{-3}eV^2 with β=0.00. Assuming to null oscillation, the χ^2 is 1.63/5.

7.2.5 Analysis for combined upward stopping and through-going muons

The χ^2 definition of the combined upward stopping muon flux and through-going muon flux is expressed as follows,

$$\begin{aligned}
\chi^2_{upmu} &= \sum_{i=1}^{10(thru)} \left(\frac{\left(\frac{d\Phi}{d\Omega}\right)^{thru,i}_{obs} - (1+\alpha)\left(1+2\varepsilon(\cos\theta_i+\frac{1}{2})\right)\left(\frac{d\Phi}{d\Omega}\right)^{thru,i}_{theo}}{\sqrt{(\sigma^{thru,i}_{stat})^2+(\sigma^{thru,i}_{sys})^2}} \right)^2 \\
&\quad + \sum_{i=1}^{5(stop)} \left(\frac{\left(\frac{d\Phi}{d\Omega}\right)^{stop,i}_{obs} - (1+\alpha)(1+\beta)\left(1+2\varepsilon(\cos\theta_i+\frac{1}{2})\right)\left(\frac{d\Phi}{d\Omega}\right)^{stop,i}_{theo}}{\sqrt{(\sigma^{stop,i}_{stat})^2+(\sigma^{stop,i}_{sys})^2}} \right)^2 \\
&\quad + \left(\frac{\alpha}{\sigma_\alpha}\right)^2 + \left(\frac{\beta}{\sigma_\beta}\right)^2 + \left(\frac{\varepsilon}{\sigma_\varepsilon}\right)^2
\end{aligned} \tag{7.5}$$

where $\left(\frac{d\Phi}{d\Omega}\right)^{thru,i}_{obs}$ and $\left(\frac{d\Phi}{d\Omega}\right)^{thru,i}_{theo}$ means the observed muon flux and theoretical muon flux for through-going muon flux in the i-th $\cos\Theta$, and $\left(\frac{d\Phi}{d\Omega}\right)^{stop,i}_{obs}$ and $\left(\frac{d\Phi}{d\Omega}\right)^{stop,i}_{theo}$ means the observed muon flux and theoretical muon flux for stopping muon flux. $\sigma^{thru,i}_{stat}$ and $\sigma^{thru,i}_{sys}$ mean the experimental statistical error and the combination of bin-by-bin uncorrelated theoretical and experimental systematic errors for through-going muon flux as described in Section 7.2.2 $\sigma^{stop,i}_{stat}$ means the experimental statistical error, and $\sigma^{stop,i}_{sys}$ the combination of bin-by-bin uncorrelated theoretical errors as shown in Figure 6.9 and experimental systematic errors as shown in Table 7.2(d) for the stopping muon flux, respectively. α means the absolute flux normalization factor with error σ_α, ε means the vertical/horizontal correlated normalization factor with error σ_ε.

The zenith angle distribution for stopping and through-going muon flux is shown in Figure 7.7 and the confidence interval is shown in Figure 7.8. The best fit is obtained at Δm^2=2.4$\times10^{-3}$eV^2 and $\sin^2 2\theta$=1.00 at a minimum χ^2 of 11.9/13 when the parameter of α is 0.01, β is -0.01, ε is 0.02. At the best fit including the unphysical region, the χ^2 becomes 10.8/13 at $\sin^2 2\theta$=1.13 and Δm^2=2.5$\times10^{-3}$eV^2 with α=0.04,β=0.08 and ε=0.00. Assuming to null oscillation, the χ^2 is 48.4/15.

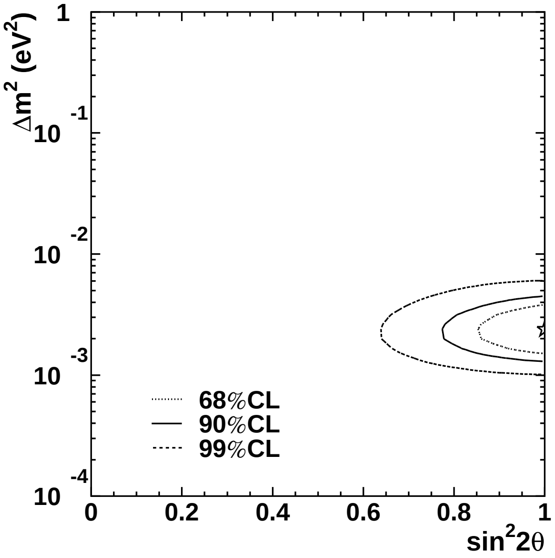

Figure 7.7: The allowed region for ν_μ-ν_τ oscillation of the upward through-going and stopping muons combined on Δm^2-$\sin^2 2\theta$. the regions means 68%, 90% and 99% confidence level. 'star' means the best fit point as $(\Delta m^2, \sin^2 2\theta) = (2.4\times10^{-3}, 1.0)$.

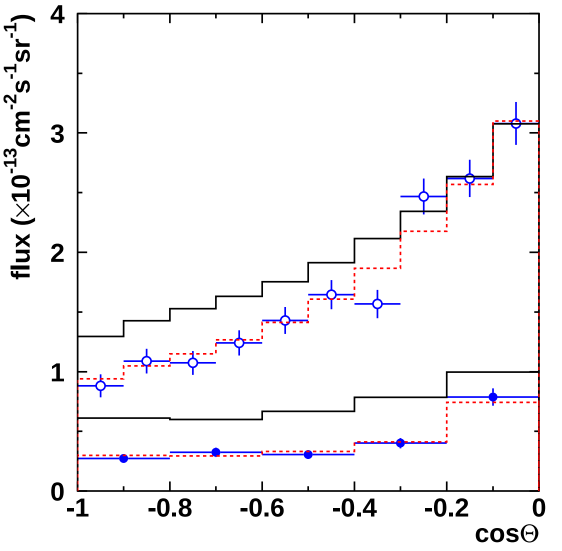

Figure 7.8: The zenith angle distribution of the upward through-going muon flux and the upward stopping muon flux. The dashed line means the expected flux at the best fit parameter (α=0.01,β=-0.01,ε=0.02)

Chapter 8

Conclusion

8.1 Upward-going muon flux

In 1746 live days observation of the Super-Kamiokande experiment, 1846 upward through-going muon events and 463 upward stopping muon events are obtained.

Observed upward through-going muon flux and upward stopping muon flux (E_μ>1.6GeV) are

$$\begin{aligned} \phi^{obs}_{through\mu} &= 1.71 \pm 0.04(stat.) \pm 0.02(syst.) \times 10^{-13} cm^{-2} s^{-1} sr^{-1} \\ \phi^{obs}_{stop\mu} &= 0.42 \pm 0.02(stat.) \pm 0.02(syst.) \times 10^{-13} cm^{-2} s^{-1} sr^{-1}. \end{aligned}$$

The combined flux and the ratio of the upward stopping/through-going muons are

$$\begin{aligned} \phi^{obs}_{\mu} &\equiv \phi^{obs}_{stop\mu} + \phi^{obs}_{through\mu} \\ &= 2.13 \pm 0.046(stat.) \pm 0.03(sys.) \times 10^{-13} cm^{-2} s^{-1} sr^{-1} \\ R^{obs} &\equiv \phi^{obs}_{stop\mu} / \phi^{obs}_{through\mu} \\ &= 0.245 \pm 0.014(stat.) \pm 0.013(syst.). \end{aligned}$$

The expected upward-going muon flux is estimated by analytical calculation based on the Bartol atmospheric flux model, GRV94 parton distribution function for deep inelastic scattering and muon energy loss by Lohmann. Expected fluxes are

$$\begin{aligned} \phi^{theo}_{through\mu} &= 1.97 \pm 0.44(theo.) \times 10^{-13} cm^{-2} s^{-1} sr^{-1} \\ \phi^{theo}_{stop\mu} &= 0.73 \pm 0.16(theo.) \times 10^{-13} cm^{-2} s^{-1} sr^{-1} \\ \phi^{theo}_{through\mu+stop\mu} &= 2.70 \pm 0.47(theo.) \times 10^{-13} cm^{-2} s^{-1} sr^{-1} \\ R^{theo} &= 0.372^{+0.049}_{-0.044}(theo.). \end{aligned}$$

There are not significant difference between the observed and expeceted flux both of the upward through-going and stopping muons. The double ratio of the observed ratio to the expected ratio is 0.659 and the difference comes to 2.6σ.

	$\sin^2 2\theta$	Δm^2	α	β	ε	χ^2/dof	Probability
Through	0.00	-	-0.15	-	0.07	28.9/ 10	1.3×10^{-3}
-going	1.24	2.3×10^{-3}	0.04	-	0.00	9.13/ 8	0.33
(10 bins)	1.00	3.2×10^{-3}	0.04	-	0.01	9.49/ 8	0.30
Stopping	0.00	-	0.00	-	-0.47	15.7/ 5	7.7×10^{-3}
(5 bins)	1.15	2.5×10^{-3}	0.00	-	0.14	1.31/ 3	0.73
	1.00	1.9×10^{-3}	-0.00	-	-0.03	1.59/ 3	0.66
Ratio	0.00	-	-	-0.35	-	13.9/ 5	1.7×10^{-2}
(5 bins)	1.04	2.5×10^{-3}	-	0.00	-	1.63/ 3	0.65
	1.00	2.1×10^{-3}	-	-0.02	-	1.75/ 3	0.63
Through	0.00	-	-0.16	-0.35	0.08	48.4/ 15	2.1×10^{-5}
+stopping	1.13	2.5×10^{-3}	0.04	0.08	0.00	10.8/ 13	0.63
(15 bins)	1.00	2.4×10^{-3}	0.01	-0.01	0.02	11.9/ 13	0.54

Table 8.1: The summary of $\sin^2 2\theta$, Δm^2, normalization parameters and probabilities at the best fit point and null oscillation. $\sin^2 2\theta=0$ means null oscillation.

8.2 Neutrino oscillation

In the analysis of the combined upward through-going muon flux and stopping muon flux, the result of the χ^2 analysis in the zenith angle distribution is consistent with the hypothesis of ν_μ-ν_τ oscillation with the parameters of $\sin^2 2\theta>0.7$ and $1.3\times10^{-3}<\Delta m^2<4.5\times10^{-3}$ eV^2 at 90 % confidence level. The probability of the hypothesis of null oscillation is 2.1×10^{-5}. Thus, null oscillation is strongly disfavored. At the best fit, the χ^2 becomes 11.9/13 at $\sin^2 2\theta=1.00$ and $\Delta m^2=2.5\times10^{-3}$eV^2 with $\alpha=0.01$,$\beta=-0.01$ and $\varepsilon=0.02$. The result of the χ^2 analysis is consistent with the hypothesis of ν_μ-ν_τ oscillation.

In the analysis of upward through-going muon flux, The result of the χ^2 analysis is consistent with the hypothesis of ν_μ-ν_τ oscillation in the energy region of ~100 GeV typically. At the best fit, the χ^2 becomes 9.49/8 at $\sin^2 2\theta=1.00$ and $\Delta m^2=3.2\times10^{-3}$eV^2 with $\alpha=0.04$ and $\varepsilon=0.01$. Moreover, in the analysis of upward stopping muon flux, the result is consistent with the hypothesis of ν_μ-ν_τ oscillation in the typical energy region of ~10 GeV same as multi-GeV contained events. At the best fit, the χ^2 becomes 1.59/3 at $\sin^2 2\theta=1.00$ and $\Delta m^2=1.9\times10^{-3}$eV^2 with $\alpha=-0.001$ and $\varepsilon=-0.03$.

In the analysis of the upward stopping and through-going muon ratio, the result is also consistent with the hypothesis of ν_μ-ν_τ oscillation. At the best fit, the χ^2 becomes 1.75/3 at $\sin^2 2\theta=1.00$ and $\Delta m^2=2.1\times10^{-3}$eV^2 with $\beta=-0.01$ and $\varepsilon=0.02$.

Table 8.1 shows the $\sin^2 2\theta$, Δm^2 and χ^2 calculation parameters at the null oscillation and at the oscillation in the best fit.

Figure 8.1 shows the Allowed regions for ν_μ-ν_τ oscillation of Kamiokande[27, 28], Super-Kamiokande[32] and MACRO[66] using upward-going muon events, and Super-

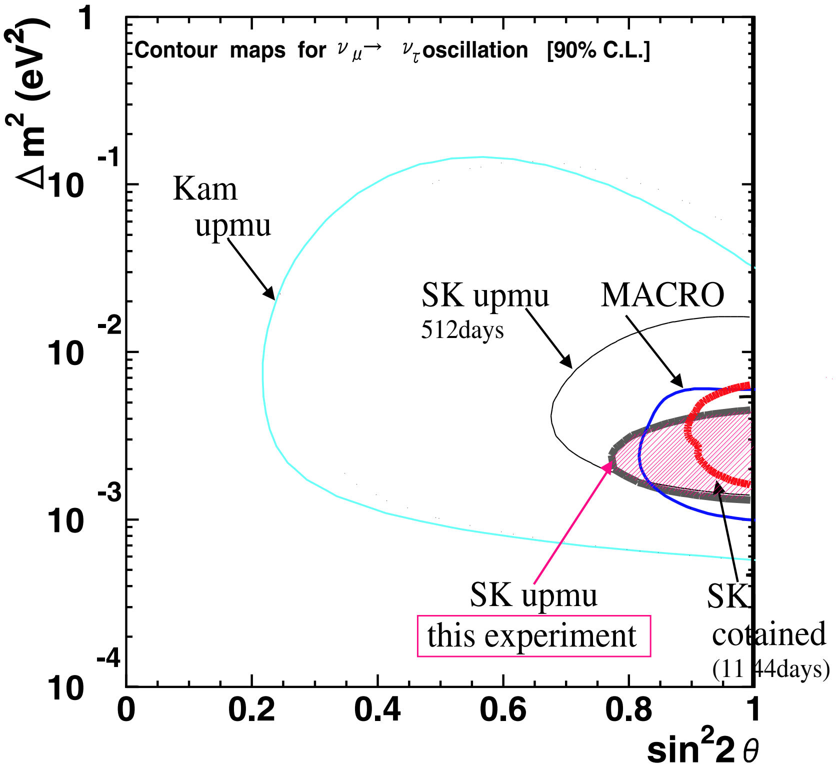

Figure 8.1: Allowed regions for ν_μ-ν_τ oscillation for ν_μ-ν_τ oscillation of Kamiokande, Super-Kamiokande and MACRO at the 90 % confidence level.

Kamiokande[67] using contained events at the 90 % confidence level.

The results in this analysis agree with the muon neutrino to tau neutrino oscillation hypothesis, and provide a confirmation of the observation of neutrino oscillations by Super-Kamiokande using the contained atmospheric neutrino events. However, it does not rule out the possibility of muon neutrinos to a mixture of tau neutrinos and a small fraction of sterile neutrinos. In other analysis[68] using the upward-going muon events and contained events of the Super-Kamiokande, no evidence favoring sterile neutrinos are found and reject the hypothesis at the 99% confidence level.

Appendix A

Monte carlo simulation

The upward-going muon flux was calculated by analytical calculation method described in Chapter 6. But the expected flux is usually estimated by Monte Carlo approach because There is no consideration for the angle of neutrino-nucleon interaction, the multiple scatter of muons, neutral current effect and the precise detector response. are described.

A.1 Atmospheric neutrino flux

In several atmospheric neutrino flux models, the Bartol model[60] is applied for the atmospheric neutrino flux as same as analytical calculation described in Section 6.2.

The neutrino energy range for this analysis of the neutrino-induced muon is applied from 1.6GeV to 90TeV. The energy spectrum and zenith angle distribution of the atmospheric neutrino flux show Figure 6.1 and Figure 6.2.

A.2 Neutrino interaction

The neutrino-nucleon interaction is applied as same as analytical calculation described in Section 6.3.1. The cross section is calculated by using GRV94 parton distribution function[62]. The charged current interaction is only generated out of the detector, and charged current interaction and neutral current are generated in the detector.

The area of the neutrino-nucleon interaction is in the spherical shape with 4km radius, where the detector is located at center of the sphere. Figure A.1 shows the distribution of neutrino interaction point. 4km radius have a margin sufficiently.

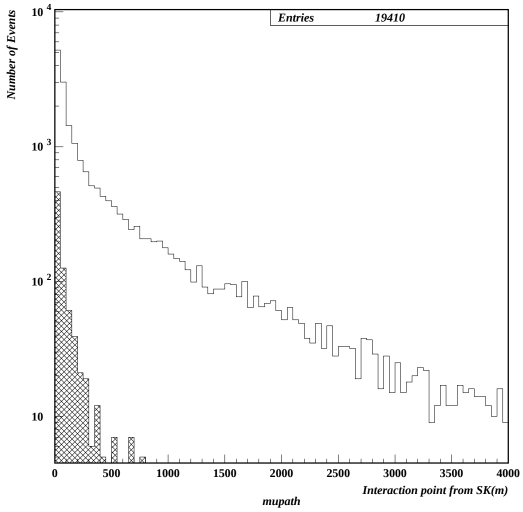

Figure A.1: The distribution of interaction point from the tank. The histogram shows all muons by the the neutrino interaction and the hatched histogram shows muons only coming into the tank.

A.3 Detector simulation

The GEANT program in CERN program library is used for detector simulation commonly used in high-energy experiments.

A.3.1 Muon energy loss

The muon energy loss is applied the Lohmann's model[18], same as analytical calculation.

A.3.2 Data selection

The data selection is done by true information, judgment between stopping muon and through-going muon, and 7m track length cut and zenith angle cut are applied.

A.4 Comparison between MC and analytical calculation

The live time 49.5 years Monte Carlo data was generated. The Monte Carlo result and the analytic calculation result are compared in the absolute flux and the zenith angle distribution of the flux.

The comparison result for upward through-going muon flux is shown in Figure A.2. The absolute flux is 1.91 ± 0.01(stat) ($\times 10^{-13} cm^{-2} s^{-1} sr^{-1}$) for Monte Carlo and 1.97 ($\times 10^{-13} cm^{-2} s^{-1} sr^{-1}$) for analytic calculation. The Monte Carlo absolute flux is smaller than analytic calculation with 3 %.

The comparison result for upward stopping muon flux is shown in Figure A.3. The absolute flux for upward stopping muon is 0.73 ± 0.01(stat.) ($\times 10^{-13} cm^{-2} s^{-1} sr^{-1}$) for Monte Carlo and 0.73 ($\times 10^{-13} cm^{-2} s^{-1} sr^{-1}$) for analytic calculation obtained. The MC flux is consistent with the analytical flux.

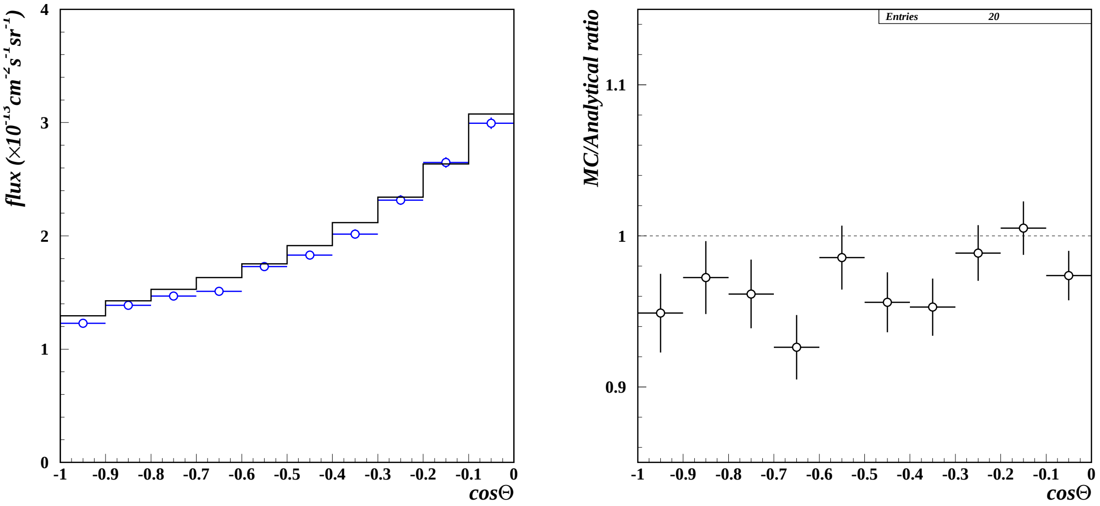

Figure A.2: Zenith angle distribution of the upward through-going muon flux. The left figure shows the Monte Carlo flux(cross) and the analytic calculation flux(solid). The right figure shows the zenith angle shape difference.

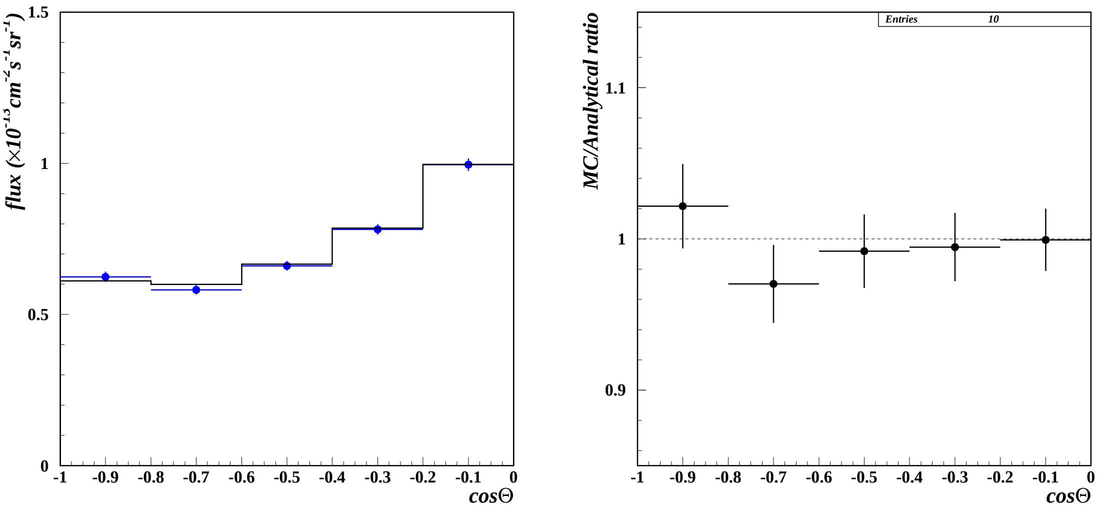

Figure A.3: Zenith angle distribution of the upward stopping muon flux. The left figure shows the Monte Carlo flux(cross) and the analytic calculation flux(solid). The right figure shows the zenith angle shape difference.

Appendix B

Fitting method selection

In the three fitters, that is OD-fit, TDC-fit and upmu-fit, the most appropriate fitting method is selected to decide the entrance point and direction.

At first, the three angular difference between two directions which is determined by each fitting is calculated. Δ(OD,TDC), Δ(OD,upmu) and Δ(TDC,upmu) are defined as the angular difference between the direction of OD-fit and TDC-fit, of OD-fit and upmu-fit and of TDC-fit and upmu-fit, respectively.

If OD-fit can be used, The entrance point and direction are determined by following,

- Total p.e./track length ≤ 40
  Upmu-fit is used.
- $40 <$ Total p.e./track length ≤ 50
  TDC-fit is used if Δ(OD,TDC) $<$ Δ(OD,upmu)
  OD-fit is used if Δ(OD,TDC) $\geq$ Δ(OD,upmu)
- $50 <$ Total p.e./track length ≤ 500
  OD-fit is used if Δ(OD,TDC) $<$ Δ(OD,upmu)
  TDC-fit is used if Δ(OD,TDC) $\geq$ Δ(OD,upmu)
- Total p.e./track length ≥ 500
  OD-fit is used.

When the Number of OD cluster is only one, two new directions are defined. The exit point is OD hit point and entrance is the point from upmu-fit(new OD). If Δ(new OD,upmu) is within the angular resolution, the entrance and exit point is defined as new OD, and upmu-fit is used by changing the other condition.

So the entrance point and direction determined by following,

- Total p.e./track length ≤ 40
  Upmu-fit is used.

- 40 < Total p.e./track length ≤ 50
  The exit point is OD hit point and entrance is the point from upmu-fit(upmu+OD-fit)
  upmu+OD-fit is used if Δ(upmu+OD,upmu) is in the angular resolution.
  Upmu-fit is used if Δ(upmu+OD,upmu) is beyond the angular resolution.

- 50 < Total p.e./track length ≤ 500
  The exit point is OD hit point and entrance is the point from upmu-fit(TDC+OD-fit)
  TDC+OD-fit is used if Δ(TDC+OD,TDC) is in the angular resolution
  TDC-fit is used if Δ(TDC+OD,TDC) is beyond the angular resolution.

- Total p.e./track length ≥ 500
  TDC-fit is used.

When there is no OD cluster,

- Total p.e./track length ≤ 40
  Upmu-fit is used.

- 40 < Total p.e./track length ≤ 500
  upmu-fit is used if Δ(TDC,upmu) is in the angular resolution.
  TDC-fit is used if Δ(TDC,upmu) is beyond the angular resolution.

- Total p.e./track length ≥ 500
  TDC-fit is used.

Bibliography

[1] W.Pauli, **Open letter to Radioactive Ladies and Gentlemen**, (1930) (translation into English) Physics today **31**, 27 (1978)

[2] F.Reines and C.L.Cowan, Nature **178**, 446 (1956)

[3] G.Danby *et al.*, Phys. Rev. Lett. **9** 36 (1962)

[4] K.Kodama *et al.*, Phys. Lett. **B504**, 218 (2001)

[5] S.L.Glashow, Nucl. Phys. **22**, 579 (1961)

[6] S.Weinberg, Phys. Pev. lett. **19**, 1264 (1967)

[7] A.Salam, *in Elementary Particle Theory, proc. of the 8th Nobel symposium*, p.367 (1986)

[8] Particle Data Group, *Review of Particle Physics* Euro. Phys. Journal **C15** (2000)

[9] K.A.Assamagan et al., Phys. Lett. **B335** 231 (1994)

[10] R.Barate et al., Euro. Phys. Journal **C2** 395 (1998)

[11] D.N.Spergel and J.N.Bahcall, Phys. Lett. **B200**, 366 (1988)

[12] T.Yanagida, *Proceedings of the Workshop on the Unified Theory and Baryon Number in the Universe*, edited by O.Sawada and A.Sugamoto (KEK report 79-18,1979) 95

[13] M.Gell-Mann et al., *Supergravity*, (North Holland, Amsterdam,1979)

[14] Z.Maki, M.Nakagawa and S.Sakata, Prog. Theor. Phys. **28**, 870 (1962)

[15] B.Pontecoro, Sov. Phys. **JETP6**, 429 (1958); ibid., **7**, 172 (1958)

[16] M.Kobayashi and T.Maskawa, Prog. Theor. Phys. **49**, 652 (1979)

[17] R. Becker-Szendy *et al.*, Phys. Rev. D **46**, 3720 (1992)

[18] D.Casper *et al*, Phys. Rev. Lett. **66**, 2561 (1991)

[19] K.S. Hirata *et al.*, Phys. Lett. **B205**, 416 (1988)

[20] K.S. Hirata *et al.*, Phys. Lett. **B280**, 146 (1992)

[21] Y.Fukuda *et al.*, Phys. Lett. **B433**, 9 (1998)

[22] Y.Fukuda *et al.*, Phys. Lett. **B436**, 33 (1998)

[23] W.W.M. Allison, Phys. Lett. **B391**, 491 (1997)

[24] K. Daum *et al.*, Z. Phys. **C66**, 417 (1995)

[25] M. Aglietta *et al.*, *Europhysics Letters*, **8**, 611 (1989)

[26] M.Boliev *et al.*, Nucl. Phys. Proc. Suppl. **70**, 371 (1999)

[27] S.Hatakeyama *et al.*, Phys. Rev. Lett. **81**, 2016 (1998)

[28] T.Hara, Ph.D.thesis, Fac. of Science, Osaka Univ.(1996).

[29] T.Becker-Szendy *et al.*, Phys. Rev. Lett. **69**, 1010 (1992)

[30] F.Ronga *et al.*, Nucl. Phys. Proc. Suppl. **77**, 117 (1999); M.Ambrosio *et al.*, Phys. Lett. **B434**, 451 (1998)

[31] Y.Fukuda *et al.*, Phys. Rev. Lett. **82**, 2644 (1999)

[32] Y.Fukuda *et al.*, Phys. Lett. **B467**, 185 (1999)

[33] B.T.Cleveland, *et al.*, Astrophys. J. **496**, 505 (1998)

[34] K.S.Hirata *et al.*, Phys. Rev. Lett. **65**, 1297 (1990); Phys. Rev. **D44**, 2441 (1991)

[35] SAGE collaboration, Phys. Rev. Lett. **83**, 4686 (1999)

[36] W.Hampel *et al.*, Phys. Lett. **B388**, 384 (1996)

[37] Y.Fukuda *et al.*, Phys. Rev. Lett. **86**, 5651 (2001); Y.Fukuda *et al.*, Phys. Rev. Lett. **86**, 5656 (2001); Y.Fukuda *et al.*, Phys. Rev. Lett. **82**, 2430 (1999)

[38] Q.R.Ahmad *et al.*, Phys. Rev. Lett. **87**, 071301 (2001)

[39] G. Zacek *et al.*, Phys. Rev. **D34**, 2621 (1986)

[40] B. Achkar *et al.*, Nucl. Phys. **B434**, 503 (1995)

[41] M. Apollonio *et al.*, Phys. Lett. **B466**, 415 (1999)

[42] F.Boehm *et al.*, Phys. Rev. **D62**, 072002 (2000); F.Boehm *et al.*, Phys. Rev. **D64**, 112001 (2001).

[43] L.Borodovsky *et al.*, Phys. Rev. Lett. **68** 274 (1992)

[44] C.Athanassopoulos *et al.*, Phys. Rev. **C54** 2685 (1996); Phys. Rev. Lett. **77** 3082 (1996); Phys. Rev. Lett. **81** 1774 (1998)

[45] F.Bergsma *et al.*, Phys. Lett. **142**, 103 (1984)

[46] B. Armbruster *et al.*, Phys. Rev. **D65**, 112001 (2002)

[47] N.Ushida *et al.*, Phys. Rev. Lett. **57**, 2897 (1986)

[48] E.Eskut *et al.*, Phys. Lett. **B497**, 8 (2001)

[49] P.Astier *et al.*, Nucl. Phys. **B611**, 3 (2001)

[50] F.Dydak *et al.*, Phys. Lett. **B134**, 281 (1984)

[51] H.Kume *et al.*, Nucl. Inst. Meth., **A205**, 443 (1983).

[52] A.Suzuki *et al.*, Nucl. Inst. Meth., **A329**, 299 (1993).

[53] Becker-Szendy *et al.*, Nucl. Inst. Meth., **A324**, 363 (1993).

[54] T.Tanimori, H.Ikeda, M.Mori, K.Kihara, H.Kitagawa, and Y.Haren, IEEE Trans. Nucl. Sci., NS-36, 497 (1989)

[55] KEK Data Acquisition Development Working Group, *"TKO Specication"* , KEK Report 85-10, (1985)

[56] Jamie Shiers, Helge Meinhard, Otto Schaile and Michel Goossens, *The ZEBRA System*, CERN,CN Division,Program Library Office, Geneva, Swizerland, February 1995.

[57] J.W.Flanagan, Ph.D.Thesis, University of Hawaii at Manoa(1974).

[58] P.Hanggi *et al.*, Phys. Lett. **B51** (1974), 119.

[59] M.Nakahata *et al.*, Nucl. Instr. Meth. **A421** (1999), 113.

[60] Vievek Agrawal, T.K.Gaisser, Paolo Lipari, Todor Stanev, Phys.Rev. **D53** (1996), 1314.

[61] M.Honda and T.Kajita, K.Kasahara, S.Midorikawa, Phys.Rev. **D52** (1995), 4985.

[62] M.Glück, E.Reya, A.Vogt, Z.Phys. **C67** (1995), 433.

[63] D. Rein and L.M. Seghal, Ann. Phys. **133** (1981), 79.).

[64] W.Lohmann, R.Kopp and R.Voss, CERN Report No.85-03(1985) (unpublished).

[65] R.M.Sternheimer, Atomic data and Nuclear data tables 30(1984)261.

[66] M. Siolia ,for the MACRO Collaboration, *Proceeding of the XII International Symposium On Very High Energy Cosmic Ray Interactions* ,to be published.

[67] R. Svoboda *et al.*, Nucl. Phys. Proc. Suppl. **98**, 165 (2001)

[68] S. Fukuda *et al.*, Phys. Rev. Lett. **85**, 3999(2000)